MULTI-SCALE SELF-ASSEMBLY OF SILICON QUANTUM DOTS INTO AN ANISOTROPIC THREE-DIMENSIONAL RANDOM NETWORK

A THESIS SUBMITTED TO
THE GRADUATE SCHOOL OF NATURAL AND APPLIED SCIENCES
OF
MIDDLE EAST TECHNICAL UNIVERSITY

BY

SERİM KAYACAN İLDAY

IN PARTIAL FULFILLMENT OF THE REQUIREMENTS
FOR
THE DEGREE OF DOCTOR OF PHILOSOPHY
IN
MICRO AND NANOTECHNOLOGY

SEPTEMBER 2014

Approval of the Thesis:

MULTI-SCALE SELF-ASSEMBLY OF SILICON QUANTUM DOTS INTO AN ANISOTROPIC THREE-DIMENSIONAL RANDOM NETWORK

submitted by **SERİM KAYACAN İLDAY** in partial fulfillment of the requirements for the degree of **Doctor of Philosophy in Micro and Nanotechnology Department, Middle East Technical University** by,

Prof. Dr. Canan Özgen _____
Dean, Graduate School of **Natural and Applied Sciences**

Prof. Dr. Tayfun Akın _____
Head of Department, **Micro and Nanotechnology**

Prof. Dr. Raşit Turan _____
Supervisor, **Physics Dept., METU**

Assoc. Prof. Dr. Hüsnü Emrah Ünalan _____
Co-Supervisor, **Metallurgical and Materials Engineering Dept., METU**

Examining Committee Members:

Prof. Dr. Atilla Aydınlı _____
Physics Dept., Bilkent University

Prof. Dr. Raşit Turan _____
Physics Dept., METU

Assoc. Prof. Dr. Gülay Ertaş _____
Chemistry Dept., METU

Prof. Dr. Macit Özenbaş _____
Metallurgical and Materials Engineering Dept., METU

Prof. Dr. Vedat Akdeniz _____
Metallurgical and Materials Engineering Dept., METU

Date: *15.09.2014*

I hereby declare that all information in this document has been obtained and presented in accordance with academic rules and ethical conduct. I also declare that, as required by these rules and conduct, I have fully cited and referenced all material and results that are not original to this work.

Name, Lastname : SERİM KAYACAN İLDAY

Signature :

ABSTRACT

MULTI-SCALE SELF-ASSEMBLY OF SILICON QUANTUM DOTS INTO AN ANISOTROPIC THREE-DIMENSIONAL RANDOM NETWORK

Kayacan İlday, Serim

Ph.D., Department of Micro and Nanotechnology

Supervisor : Prof. Dr. Raşit Turan

Co-Supervisor : Assoc. Prof. Dr. Hüsnü Emrah Ünalan

September 2014, 167 pages

The most important problem limiting the impact of nanotechnology is probably the difficulty in effectively linking nanoscale materials and processes to the macroscopic world. Topology and material properties are intricately coupled and conditions that pertain to atomic, microscopic and macroscopic scales are often seemingly mutually exclusive. This thesis introduces a state-of-the-art nanostructure that hierarchically builds itself from the atomic to the microscopic scales, which can connect to the macroscopic world without detracting from its nanoscale properties. The three-dimensional anisotropic random network of silicon quantum dots is largely isotropic in the atomic scale but it grows to become anisotropic in the microscopic scale. We show that quantum confinement is preserved and the current flows through the network without relying on inefficient tunnelling currents. Former pertains to the atomic scale and latter manifesting at the microscale; these two scale-dependent features were thought to be mutually exclusive prior to this thesis. The structure is self-assembled from a silicon-rich silicon oxide thin film. Microscale self-assembly is kinetically driven under nonequilibrium conditions established by magnetron sputter deposition and relies on control of surface diffusion through a surface

temperature gradient. Atomic scale self-assembly is chemically driven under local nonequilibrium conditions provided by fast stochastic deposition and relies on control of phase separation by stabilizing nominally unstable suboxides. We show that our fabrication methodology is inherently modular, material-independent, and is not affected substantially by the initial conditions, as self-assembly under nonequilibrium conditions and nonlinear dynamics sweeps aside a large number of factors that influence the details of thin-film growth, but provides simple a couple of "rules" with clearly identifiable corresponding experimental conditions to determine the final morphology.

Keywords: Silicon nanostructure, Self-assembly, Random network, Stochastic growth, Ballistic deposition, Percolation

ÖZ

ÇOKLU ÖLÇEKTE KENDİLİĞİNDEN OLUŞAN ÜÇ BOYUTLU EŞYÖSÜZ RASTGELE SİLİSYUM KUVANTUM NOKTA AĞI

Kayacan İlday, Serim
Ph.D., Mikro ve Nanoteknoloji Bölümü
Tez Yürütücüsü : Prof. Dr. Raşit Turan
Ortak Tez Yürütücüsü : Assoc. Prof. Dr. Hüsnü Emrah Ünalan

Eylül 2014, 167 sayfa

Nano ölçekteki malzemeleri ve süreçleri makro dünya ile etkili bir biçimde bağlayabilmek hususundaki zorluk büyük ihtimalle nanoteknolojinin devrimsel etkisini sınırlayan en önemli problemdir. Malzeme özellikleri ve topolojisi birbirleri ile karmaşık bir ilişkide olup, atomik, mikro ve makro ölçek gereklilikleri genellikle aynı anda sağlanamamaktadır. Bu tez atomik ölçekten mikro ölçeğe kendini oluşturan ve nano ölçek özelliklerini bozmadan makro dünya ile iletişim kurabilen gelişmiş bir nanoyapı sunmaktadır. Üç boyutlu eşyönsüz rastgele silisyum kuvantum nokta ağı atomik ölçekte büyük oranda eşyönlü olup mikro ölçeğe doğru büyürken eşyönsüz hale gelmektedir. Bu çalışma ile bu yapılarda kuvantum hapsolma olgusunun geçerli olduğunu ve elektrik akımının ağ içerisinden verimsiz tünelleme mekanizmasına gerek duymadan aktığını gösterdik. Önceki atomik ölçeğe ait olan ve sonraki mikro ölçekte kendini gösteren bu iki özellik bu tezden önce aynı anda var olamaz olarak bilinirdi. Bu yapı silisyum-zengin silisyum oksit ince filmden kendiliğinden oluşmuştur. Mikro ölçekte kendiliğinden oluşma magnetron saçtırıcı tarafından sunulan dengede olmayan koşullarda kinetik olarak güdülmüş olup, yüzeyde oluşturulan sıcaklık farkı tarafından yüzey difüzyonunun kontrol edilmesi

esasına dayanmaktadır. Atomik ölçekte kendiliğinden oluşma ise hızlı, rastgele çökertme süreci tarafından sağlanan bölgesel dengede olmayan koşullarda kimyasal olarak güdülmüş olup göreceli kararsız oksitlerin karalı hale getirilerek faz ayrışmasının önlemesi esasına dayanmaktadır. Bu tezde üretim yöntemimizin kendi özünde modüler, malzemeden ve başlangıç koşullarından bağımsız olduğunu gösterdik. Şöyle ki; dengede ve doğrusal olmayan koşullar altında kendiliğinden oluşma, ince film büyümesi hususundaki detayları etkileyen birçok faktörün önüne geçerek deneysel koşullarda gerçekleştirilebilecek birkaç basit ‘kural' yardımı ile sonuç morfolojisini etkileyebilir.

Anahtar Kelimeler: Silisyum nanoyapılar, Kendiliğinden oluşma, Rastgele ağ, Olasılıklı büyüme, Perkolasyon, Balistik çöktürme.

To my soul, my joy, my daylight, my inspiration, my son Kayra Evrenos…

&

To the loving memory of my sister, Sibel Kayacan,
may her gentle spirit rest in peace…

"I died as a mineral and became a plant,
I died as plant and rose to animal,
I died as animal and I was Man.
Why should I fear? When was I less by dying?
Yet once more I shall die as Man, to soar
With angels blest; but even from angelhood
I must pass on: all except God doth perish.
When I have sacrificed my angel-soul,
I shall become what no mind e'er conceived.
Oh, let me not exist! for Non-existence
Proclaims in organ tones,
To Him we shall return."
Rumi

ACKNOWLEDGMENTS

I would first like to thank to my family, Fatma and Mustafa Kayacan, F. Mübeccel and M. Doğan İlday, and Seda and Mesut Laçin, for their unconditional love, endless emotional support and encouragement during my journey to pursue my passion for science. I would like to express my most sincere gratitude to my husband F. Ömer İlday for he is my mentor, my best friend, my soul mate, my role model, and my "Giskard Reventlov". Thank you for being an unofficial advisor to me on many occasions. His never-ending efforts to restore my self-confidence that helped me move on every time I felt discouraged. I am also grateful to him for providing me a meaningful life, full of joy and intellectual stimulations. Kayra E. İlday, my little son, thank you for being the fountain of my inspiration. I draw many interesting and intriguing ideas, which I intend to pursue during my coming years as a scientist, just by observing his growth starting from his very existence in my womb.

I would like to next thank to my advisor Raşit Turan for encouraging me to explore and pursue all my ideas freely, showing me lots of patience and giving me the opportunity to work in a stimulating research environment. I am also grateful for his constant help and effort to get me access to various lab equipment and facilities that were crucial to my research. I also appreciate his efforts in arranging fruitful research visits to HZDR and CNR-Catania for me, which I enjoyed and where I learned a lot.

I would like to thank to Mustafa Kulakçı, M. Emre Kabadayı, and Vaksis team for helping me deal with "constantly" impaired lab equipment day and night. I am also grateful to Gizem Nogay and İsmail Kabaçelik for helping me out with the lab work; to Seçkin Öztürk and İlker Yıldız for sparing their time for me in long XPS and TEM sessions; to Hande and Daniele Toffoli for providing MD simulations; to Alexander Houssou, Francois Horrard, Peter H. Clifton, and people at CAMECA Madison Lab. for providing APT analyses; to Zaki M. Saleh for his enthusiasm for collaboration; to Doğan Mansuroğlu and Hasan H. Güllü for sharing their lab equipment with me; and

to the technical and administrative staff of GÜNAM, namely, Yücel Eke, Nevzat Görmez, Tayfun Yıldız, Dursun Erdoğan, Harun Tanık, Buket Gökbakan, and Tuncay Güngör for making life easier for me.

I wish to extend my thanks to K-H. Heinigh, Berndt Schmidt, and David Friedrich for their company and hospitality during my visit to HZDR. I also thank David for the RBS analyses and the trip to Königstein. I wish to thank to Rene Hübner for his great efforts in EFTEM analyses. I would like to express my sincere gratitude to Salvatore Mirabella, Antonio Terrasi, Salvatore Cosentino, Isodiana Crupi, and Rosario Raciti for their great hospitality, many stimulating discussions, and their sincere friendship during my visit to CNR-Catania, which was extremely fun, productive, and educational. I also appreciate the support from and useful discussions with my co-advisor H. Emrah Ünalan; from the committee members of my graduate study Atilla Aydınlı and Gülay Ertaş; and from researchers, namely, Oğuz Gülseren, Ceyhun Bulutay, and Emel Sungur Özen I've had the pleasure and opportunity to work with.

I would like to extend my thanks to my fellow lab mates at GÜNAM, namely, İrem Tanyeli, Serra Altınoluk, Zeynep Demircioğlu, E. Hande Çiftpınar, Makbule Terlemezoğlu, Fırat Es, Olgu Demircioğlu, Mete Günöven, Engin Özkol, Mehmet Karaman, Gülsen Baytemir, Hisham Nasser, Salar S. Sedani, Fatih Uzgur, Burcu Altuntaş, Yasin Ergunt, Özden B. Balbaşı, Burcu Barutçu, Çiğdem Doğru, Zeynep D. Eygi, Kutlu Kutluer, and Nader A. Moggaddam for providing me lots of amusement, their friendship, support, and making me feel appreciated.

Last but not the least, I would like to thank Gökçe Küçükayan Doğu for being beside me whenever I need her and being a gentle guide during most difficult times. I also thank to Onur Tokel, Erçağ Pinçe, and Şafak Doğu for their friendship and half scientific, half nerdish but always intriguing discussions.

TABLE OF CONTENTS

LIST OF TABLES

TABLES

LIST OF FIGURES

FIGURES

CHAPTER 1

INTRODUCTION

"None of the global warming discussions mention the word 'nanotechnology'. Yet nanotechnology will eliminate the need for fossil fuels within 20 years. If we captured 1% of 1% of the sunlight (1 part in 10,000) we could meet 100% of our energy needs without ANY fossil fuels. We can't do that today because the solar panels are too heavy, expensive, and inefficient. But there are new nanoengineered designs that are much more effective. Within five to six years, this technology will make a significant contribution. Within 20 years, it can provide all of our energy needs."

- Ray Kurzweil, Washington Post: Artificial Intelligence, When Humans Transcend Biology, Monday, June 19, 2006

Demand for lighter, faster, smaller, smarter, and cheaper devices pushes today's everyday technologies to seek alternative solutions that can reduce the production costs, increase efficiency, and provide multifunctionality. Nanoengineered materials, designed by starting at the atomic level and building up towards intended nanoscale, microscale and macroscopic properties, offer fascinating possibilities [1-4]. However, searching for ways to incorporate nanomaterials into everyday use is one of the least-addressed aspects of nanotechnology, which requires excellent control over the processes in the nanoscale as well as establishing a link to the macroscopic world [5-10]. This is a notoriously difficult task, as topology and various material properties are intricately coupled and are often seemingly mutually exclusive over different length scales, from atomic to microscopic and to macroscopic [11-13].

Given the vast number of possible nanostructures even for a simple material system, unguided optimization is clearly not the way forward.

The aim of this thesis is to contribute addressing this 60-year-old problem and to develop a simple, generic methodology to engineer the topology of a material with programmable properties, starting at the atomic scale and building up towards the macroscopic scale [5-13]. This is a general problem; here, we focused on a specific roadblock faced in optoelectronics, most notably in photovoltaics: Achieving good current flow, which manifests at the micro/macroscale, through quantum-confined structures, which pertain to the atomic scale; two features that were thought to be mutually exclusive prior to this thesis [14-16]. Good electrical conduction requires a percolated nanocrystal network, which can be achieved at high concentrations of the conductive material (*e.g.*, Si), but this inadvertently leads to nanocrystal sizes larger than the critical Bohr radius, resulting in loss of quantum confinement [17-18]. On the other hand, if the concentration is low enough to preserve quantum confinement, most of the elements of the network do not interconnect, and conductivity has to rely on tunneling currents, which are very inefficient [17-18]. Up until now, no structure has been presented that satisfies the multiscale requirement to exhibit both good electrical conduction and quantum confinement simultaneously [14-16]. Clearly, new topologies with higher complexity, such as interconnected networks of 1D- and/or 2D-quantum-confined structures, are needed for a breakthrough [5,10,14,19-22]. Such complex structures can exhibit completely new and superior features, which are absent in their individual constituents, but emerging from their collective interactions as defined in part by their topology [5,7-9,11,13,23].

This thesis reports a novel, hierarchically ordered silicon topology that combines quantum-dot-like optical properties with electrical conduction as envisioned by Priolo, *et al.* [14]; an anisotropic 3D random network of silicon quantum dots that grows preferentially in the vertical direction, for which the quantum confinement is satisfied, and the carriers can travel along the network without relying on tunneling

currents. It is noteworthy that the structure is not only robust after exposure to air over more than a year, but also survives prolonged annealing at high-temperatures, and that it is highly uniform within a sample and highly reproducible from sample to sample. This novel, robust nanoarchitecture can pave the way for a new era in silicon photonics [4,14,15,24,25,26], and photovoltaics [14-16,19,22-24,26-29]. Apart from its potential electronic, photonic, and photovoltaic applications, this unique architecture can also be used in biophotonics [26], imaging technologies [26], Li-ion batteries [26,30,31], and chemical and biomedical sensors [32] thanks to its large surface area and very easy fabrication method, combined with its unique properties.

Beyond this technical breakthrough in multifunctional material design over multiple length scales, we effectively show that the growth dynamics of a complex material can be steered towards a stable final state with preplanned properties simply by exploiting universal stochastic growth dynamics. Fabrication of such multiscale functional materials using traditional methods generally requires advanced control over dynamical details of the system. Nevertheless, interplay between topology and material properties is not well understood and remains difficult to control [6,13,33-35]. Self-assembly is the most appealing way to fabricate stable and highly reproducible complex morphologies with good control over their long-range orders [5,13,22,23,36]. Spontaneous emergence of complex topologies through self-assembly generally requires nonequilibrium conditions under which the dynamical evolution of the system can bifurcate without requiring deliberate intervention and can be partially steered through addition of an external energy/force [10,13,21,23,37] or influence of thermal gradients, as in our case. The anisotropic 3D random network of silicon quantum dots presented in this thesis spontaneously self-assembles from a silicon-rich silicon oxide thin-film under nonequilibrium conditions through stochastic growth. Microscale self-assembly of the vertically aligned random network is kinetically driven under nonequilibrium conditions established by magnetron sputter deposition and relies on control of surface diffusion through a temperature gradient on the surface. Atomic scale self-assembly of the percolated

quantum dot network is chemically driven under local nonequilibrium conditions provided by the fast stochastic deposition process and relies on control of phase separation by creating and stabilizing a nominally unstable medium, which is composed mostly of suboxides.

The research goals pursued in this thesis were ambitious, requiring an inter-disciplinary approach and a fastidious experimental optimization effort, bringing together concepts such as multiscale, hierarchical, directed/guided self-assembly; random networks; universality in dynamic systems; nonlinear dynamics; stochastic growth; ballistic deposition; percolation; local chemical bonding dynamics; numerical modeling; and molecular dynamics simulations. While this thesis cannot realistically attempt to scrutinize every detail of the various physics involved, we provide a clear recipe, the essence of which is generally applicable to a great variety of materials. Inspired by nature's methods of spontaneous pattern formation, we have demonstrated that absolute order can be controlled through a simple, generic methodology without gaining absolute control over every dynamical detail of the system. This way, the emergent structure becomes largely independent of the nature of its constituents. This means that even though we demonstrate our methodology on a specific material, the methodology is inherently material independent and its steps are modular. Thus, it can be used as a template to synthesize other multifunctional materials and should open up new opportunities in countless applications that can benefit from the engineering of matter on the atomic scale to microscale, even to macroscale. Moreover, results presented in this thesis can be expected to provide useful insights for efforts on effective incorporation of nanomaterials into everyday use devices based on low-cost, efficient, multifunctional next-generation technologies, specifically in the field of photovoltaics.

Outline of the thesis is as follows: Chapter 2 discusses the need to link the nanoscale to the macroscopic world in order to leap forward to next-generation technologies, where we discuss the general principles of how to engineer the microscopic and

atomic scale properties of a given material system to achieve desired functionality. The details of the multiscale self-assembly along with ballistic deposition theory and Kardar-Parisi-Zhang universality are explained in detail in Chapter 3. Chapter 4 discusses the experimental conditions developed to fabricate and the analytical methodology to characterize the anisotropic 3D random network of silicon quantum dots. Investigation of silicon-rich silicon oxide thin-films with thorough structural, chemical, optical, and electrical characterization is presented in Chapter 5. Chapter 6 presents the anisotropic 3D random network of silicon quantum dots and its unique features, where we demonstrate successful achievement of several key properties: Namely, we show that the free charge carriers are confined in the silicon quantum dot network, its bandgap is tunable, and electrons can freely travel along the network. Finally, Chapter 7 concludes the thesis, where the major results and achievements are summarized and their potential impact on next-generation technologies is discussed.

CHAPTER 2

LINKING THE NANOSCALE TO THE MACROSCOPIC WORLD: TOWARDS NEXT GENERATION TECHNOLOGIES

"To see the world in a grain of sand,
And a heaven in a wild flower,
To hold infinity in the palm of your hand,
And eternity in an hour."
- William Blake, Auguries of Innocence, 1803

Mankind has always been fascinated by nature's ability to form repeating geometrical patterns that are immensely diverse yet somehow connected to each other at every scale from the nucleus to the cosmos (Fig. 1). How does nature orchestrate spontaneous pattern formation in so many different physical systems, ranging from patterns in sand dunes to primitive life forms, all the way up in complexity, to the primate brain, and modern human social constructs? We do not quite know yet, but as far as we understand, nature never cares or needs to tell precisely where each particle should go; instead, structure and functionality effortlessly emerge through "self-assembly", resulting from stochastic processes, often shaped or regulated by multiple nonlinear feedback mechanisms [38-40]. Although multiscale self-assembly that leads to multifunctionality is ubiquitous in nature, its deliberate use to synthesize designer materials remains rare partly due to the notoriously difficult problem of controlling topology from the atomic to the microscopic scales to achieve desired features. Needless to say, it is utmost important to find a way to incorporate nanomaterials into everyday use for nanotechnology to fulfill its potential.

Figure 1 Images showing repeated geometrical patterns observed in Nature: Stripes in a cloud formation, in a fish skin and in a gas giant (Jupiter); Hexagons in rocks (Giant's causeway), in a honeycomb and in a snowflake; Spirals in a galaxy (M51), in a shellfish and in a pine cone; Branches in a lightning, in a tree branch and in a human lung.

Many researchers have been and still are raving about the transformative power of nanotechnology and hail the arrival of advanced nanomaterials that will lead to a leap forward in various technologies. Despite the fact that there have been great technological advancements over the last 60 years, we are still far from benefiting from the full potential of nanotechnology. For nanotechnology and nanomaterials to

fulfill their promises, they have to operate as designed in the nanoscale, while successfully bridging to the macroscopic world without detracting from their nanoscale properties [5-10]. Although there is extensive research on the fabrication and characterization of nanomaterials, studies that are addressing specific roadblocks towards this goal are very few [11-13]. This is partly due to the fact that we neither fully understand nor can precisely control a material's topology and its desired features over vastly different length scales since they are intricately coupled.

Nevertheless, it should be possible to exploit nature's spontaneous pattern formation principles to achieve superior technological functionalities, which may be difficult or even impossible to achieve with traditional approaches. There is absolutely no physical law that forbids this, but our present understanding of the fundamentals is still lacking. Significant effort is being made in this direction in various disciplines. In this vein, we have recently demonstrated the use of nonlinear feedback mechanisms that arise from the interaction of femtosecond laser pulses with material surfaces to fabricate highly uniform self-organized, self-similar nanostructures [33]. Another example and a technologically important problem awaiting an immediate solution is that our energy consumption still largely relies on fossil fuels. Today's commercial solar cells, which are used for outdoor applications, both for industrial and residential, are mainly based on thick, solar-grade, bulk silicon wafers that need to have a large area since the charge carriers are collected along the light path and minority-carrier diffusion lengths for carrier recombination is long. This translates into high production costs of silicon wafer-based solar cells [41]. An alternative way, which can reduce production costs and increase device efficiency, is to use nanostructures where quantum confinement effect can be observed. New generation solar cells based on nanostructures not only promises to be cost-effective but could also eliminate major power-loss mechanisms by broadening the bandgap coverage, by capturing the charge carriers before they are lost to lattice thermalization and by multiplying charge carrier pair generation per high-energy photon or single carrier pair generation with multiple low-energy photons [15,27,29,42-44]. However, new

generation photovoltaic technologies are just blooming for which most of the research is currently being done in the laboratory. Startup companies are developing some of the prototypes but they still do not constitute an established technology and are not widely incorporated into commercial usage. Nevertheless, hopes for new generation solar cells are high. With enough effort, solar cells can eventually replace fossil fuels and will make huge economic and environmental impact.

In order to be realistically able to utilize the sun as our primary source of energy, photovoltaic devices should fulfill three fundamental requirements simultaneously: reduced costs of primary material, absorption of a larger fraction of the solar spectrum, and good electrical conductivity [15,27,29,43,44]. For the former, silicon is a logical material of choice as it is low-cost, naturally abundant and readily available, has a band-gap of 1.12 eV that ideally matches to the terrestrial solar spectrum, and it benefits from well-established processing technologies [15]. For the latter, simply changing the sizes of silicon nanostructures can tune their optical and/or electrical bandgaps over a range of energies, which allows for tandem arrangements to maximally absorb the solar spectrum [27,29,42-44]. For the last, a percolated nanocrystal network is required to provide direct current flow, without disturbing the size-dependent optical and electrical properties of the nanocrystals, which is the showstopper.

There are established methodologies to fabricate certain silicon nanostructures, such as quantum-dots, -wells, -wires, porous silicon, which are strong candidates for use in next-generation photovoltaic devices. However, each of these candidates addresses the abovementioned requirements individually (please refer to the Section 2.1 for further details). There have also been device demonstrations based on these nanostructures, albeit with inadequate efficiencies [45-47]. However, to our knowledge, no structure has been demonstrated to date that satisfies all the abovementioned requirements simultaneously. Given that several of these features appear to be coupled and blind optimization of one of the requirements would have

detrimental effects on another, the origin of the difficulty is evident. Clearly, new strategies to fabricate topologies with higher complexity are desperately needed to leap forward in technology.

2.1 The Search for the Ideal Silicon Nanostructure

Bulk silicon has an indirect bandgap and low absorption in visible and near-infrared frequencies. Optical transitions in indirect bandgap semiconductors require phonon absorption or emission in order to conserve the crystal momentum (Fig. 2b). This obviously decreases the conversion efficiency of absorbed photon energy into electricity [14,15,27,43]. As can be seen from Fig. 2a, in a direct bandgap semiconductor, the maximum of the valance band and the minimum of the conduction band are located at the same momentum scape. This means that a hole in the valance band and an electron in the conduction band can recombine without any loss in the absorbed energy. On the other hand, in an indirect bandgap semiconductor, the minimum of the conduction band and the maximum of the valence band are not located at the same momentum scape, which means that the recombination of an electron with a hole requires phonons in order to compensate for the change in momentum (Fig. 2b and 2c). However, when free carriers are confined within a quantum structure, Heisenberg uncertainty relations become limiting: The position of the free carriers in momentum space is not precisely defined, rather it is uncertain. This means that the tails of the electron and hole wavefunctions are extended, increasing the possibility of partial overlapping. This can give rise to quasi-direct transitions and increase probability of a radiative recombination of an electron and a hole without need for a third particle, the phonon (Fig. 2d).

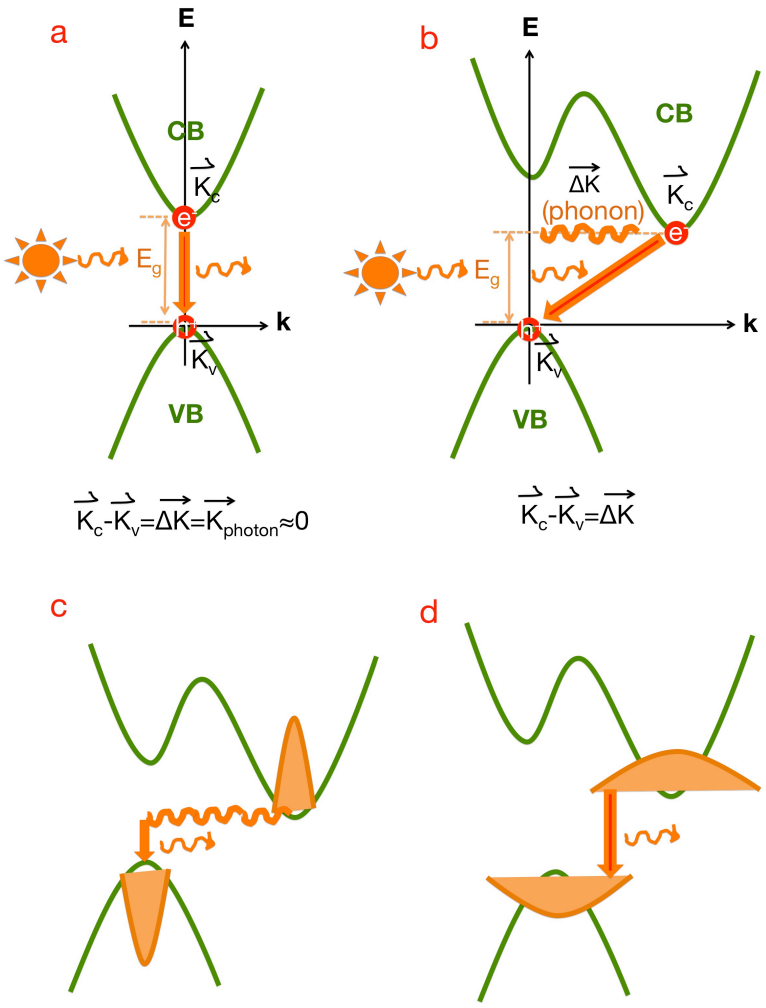

Figure 2 Sketches showing radiative recombination of free charge carriers in a **(a)** direct, and **(b)** indirect bandgap semiconductor with **(c)** large and **(d)** small indirect bandgap semiconductor crystals. Adapted from ref. [48].

The effects of quantum confinement become substantial when the diameter of the nanostructure is comparable to the wavelength of the electron wavefunction. In this condition the electron behaves like a free particle and as the confining dimension is reduced beyond a certain value, the energy spectrum starts to discretize, which results in the bandgap becoming size dependent. This phenomenon is summarized qualitatively in Fig. 3a-d.

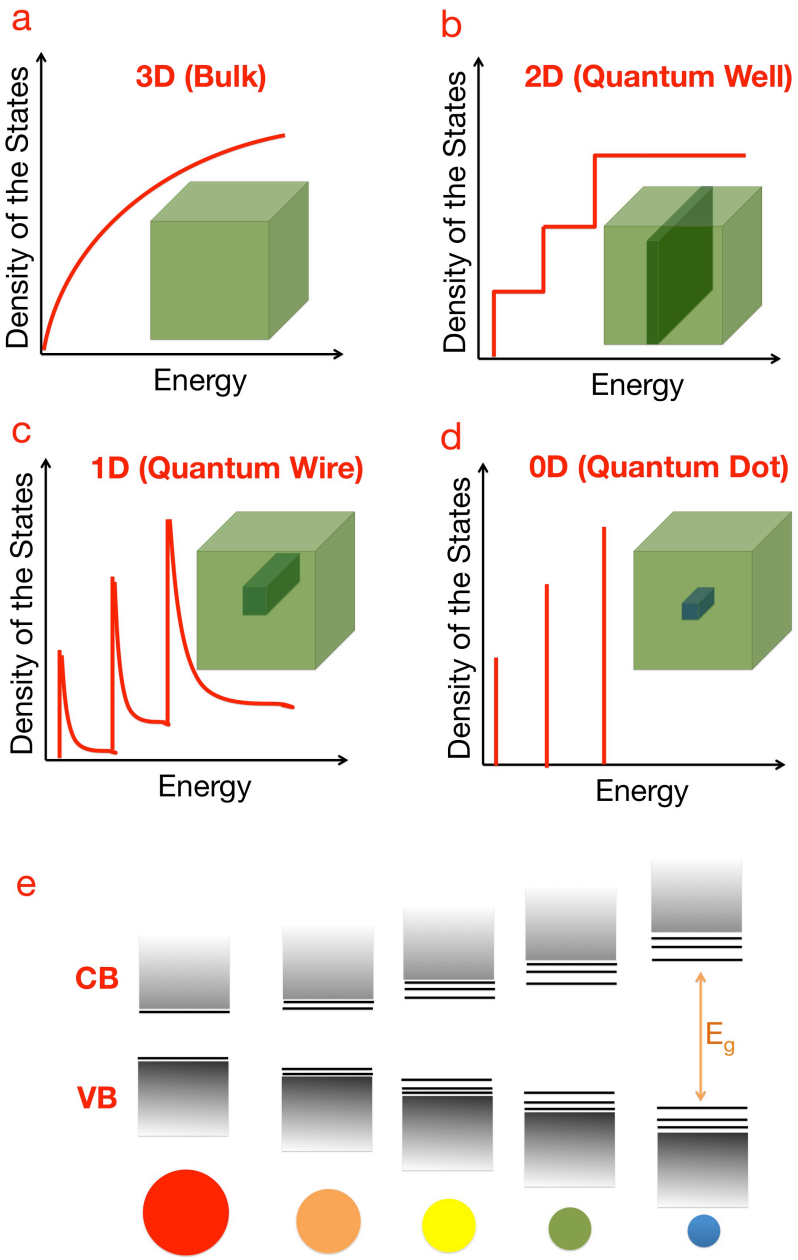

Figure 3 Graph showing quantization of density of states resulting from different levels of electron confinement for **(a)** 3D bulk, **(b)** 2D quantum well, **(c)** 1D quantum wire, and a **(d)** 0D quantum dot. **(e)** Graph showing size-dependent optical bandgap of nanocrystals. Sketches (a) to (d) are adapted from ref. [49] and (e) is adapted from ref. [50].

Quantum dots, commonly known as "artificial atoms" are nanostructures that provide 3D quantum confinement (Fig. 3d). The free charge carriers are confined in three spatial dimensions if the radius of a quantum dot becomes less than (or comparable to) the critical Bohr exciton radius, r_B. This can be explained by the following relation [51]:

$$r_B = \frac{4\pi\varepsilon_0\varepsilon_r\hbar^2}{e^2 m_0}\left(\frac{1}{m_e^*}+\frac{1}{m_h^*}\right), \qquad \text{(Eqn. 1)}$$

where ε_0 and ε_r are the permittivity of vacuum and the relative dielectric constant of the semiconductor, respectively. $\hbar = {}^{h}/_{(2\pi)} - h$ is the Planck's constant, e is the electron charge, m_0 is the electron mass, and m_e^* and m_h^* are the electron and hole relative effective masses, respectively. Depending on the ratio between the quantum dot radius and the critical Bohr exciton radius, several size quantization regimes could be defined (Fig. 3a-d).

Since simply changing their sizes can change their optical and electrical properties (Fig. 3e), quantum dots have become one of the most studied nanostructures for third-generation photovoltaic technology [54]. If quantum dots can be closely packed (Fig. 4a), the confined levels will overlap to form minibands (Fig. 4b) in quantum dot superlattices, which extends the range of electronic and optical properties that can be provided by a single semiconductor material [29,47]. If these miniband energy levels and bandwidth can be controlled, these quantum dot superlattices can be used for tandem solar cells. The tandem solar cell is basically a stack of individual solar cells with different bandgaps placed on top of each other [27,29,42-44]. Ideally, such a structure is expected to absorb different portions of sunlight at different cells with correspondingly different bandgaps, thus covering the larger spectrum of sunlight and turn it into electrical energy with significant energy efficiency (Fig. 4c). However, the main challenge for a quantum dot tandem solar cell is to get sufficient carrier mobility, hence a reasonably high electrical conductivity. In a solar cell,

quantum dots are embedded in a dielectric matrix, commonly SiO_2, Si_3N_4 or SiC to provide a potential barrier to create quantum confinement. However, the same potential barrier that underlies quantum confinement also limits extraction of free carriers from the confined environment and even when they are extracted, the carriers typically have to tunnel through a dielectric medium resulting in very inefficient current flow [12,14-16,18,52,53] (Fig. 4a). Tunneling currents require closely packed quantum dots with uniform sizes and very homogenous distribution throughout the material, which is hard to achieve. However, it has been demonstrated that one can grow thin films layer by layer with a sequence of one layer being silicon-rich silicon oxide and the other being silicon oxide [15]. This arrangement affords some control over the phase separation of silicon and silicon dioxide in the silicon-rich silicon oxide layer, which helps control the quantum dot sizes. Nevertheless, control over the phase separation is a major technical challenge since the thicknesses of the individual layers need to be extremely small (nanometer range) and the experimental conditions have to be optimized extremely carefully. Although there have been some interesting demonstrations, the photovoltaic devices showed unimpressive efficiency levels due to problems with charge transport, even in laboratory-scale conditions [45-47].

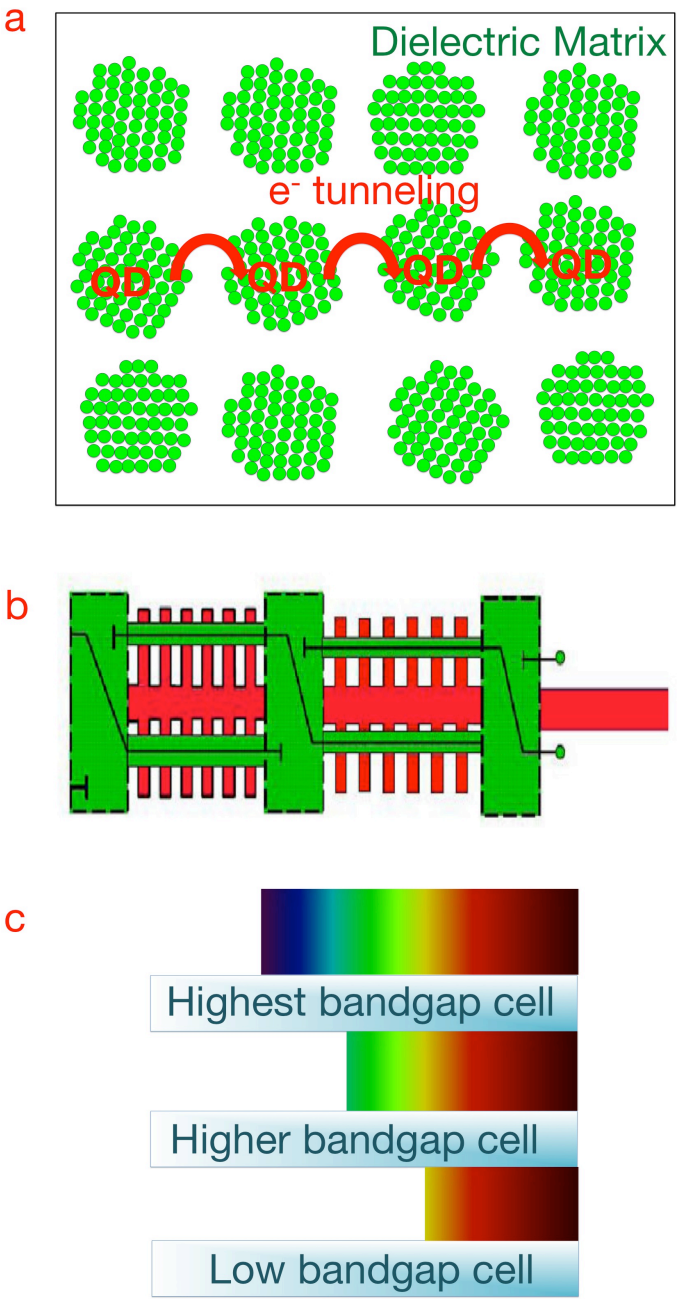

Figure 4 Sketches showing **(a)** ordered, close-packed quantum dots embedded inside a dielectric matrix, for which the electrons have to tunnel through the matrix in order to hop from one quantum dot to the other, **(b)** miniband structure resulting from closely packed quantum dots [55], **(c)** absorption of solar spectrum via a tandem solar cell. Adapted from ref. [56].

Silicon nanowires are almost perfect light trapping materials owing to their high surface area. Moreover, they are basically single crystal materials for which the current flows easily only along the wire [14-16,19]. Si nanowires are considered to be another emerging candidate for next-generation solar cells (Fig. 5a). However, individual nanowires have to be ensemble with high precision to achieve a reasonable conductivity, which is still a big concern [15,16,19]. As such, efforts to incorporate them into solar cells remain in laboratory scale.

Another alternative is porous silicon (Fig. 5b) [18]. Porous silicon has extremely large surface-to-volume ratio and a very low refraction index (<1.2). It is mainly fabricated by electrochemical etching of bulk silicon wafers, which again increases the starting material cost for large-area solar cell applications. Furthermore, control over the pore sizes and the uniformity of the pores is a major challenge from materials perspective. This leads to problems with controlling the bandgap and maintaining the electrical connection. There is also a stability problem due to the high possibility of oxidation under atmospheric conditions [14-16].

The challenge is to overcome the mutual dependency of quantum confinement and good electrical conduction and to fabricate electrically percolated, quantum-confined structures. To the best of our knowledge, no structure has been demonstrated that satisfies these requirements simultaneously. Clearly, new topologies with higher complexity, such as interconnected networks of 1D- and/or 2D-quantum-confined structures, are desperately needed to leap forward in technology considering these networks not only exhibit features different from their constituents but also benefit their collective features as well.

We would like to stress out that there are a vast diversity of topologies offered so far other than the ones summarized briefly in this section but to discuss each and every one of them is beyond the scope of this thesis. Further details on the nature and features of quantum-confined structures and their applications could be found in

references [15,57-59]. We have chosen these three structures because the majority of related research is on these structures.

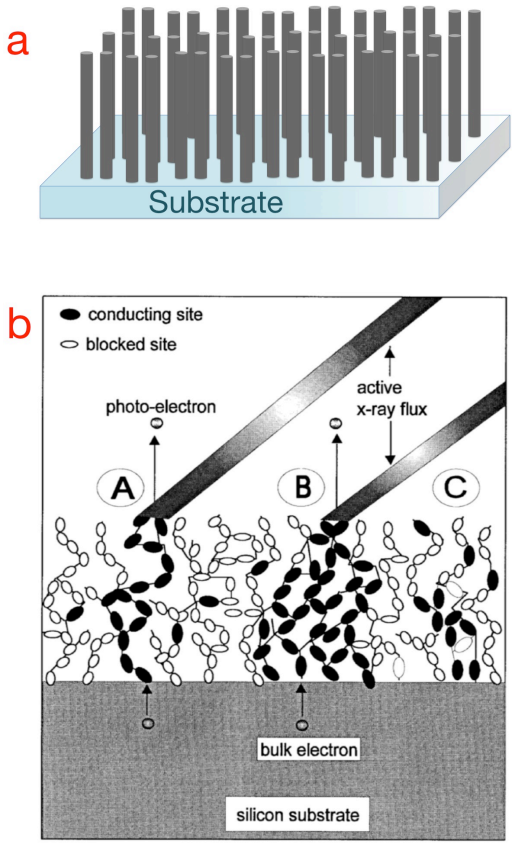

Figure 5 Sketches showing **(a)** nanowire arrays that are grown on a substrate and **(b)** growth of a porous silicon structure showing conducting and non-conducting sites. [52]

2.2 Anisotropic Three-Dimensional Random Network of Silicon Quantum Dots: A New Hope

The nature of the mutual dependency of quantum confinement and good electrical conduction along with our solution to untangling it is summarized qualitatively in

Fig. 6. As shown in Fig. 6a, good electrical conduction requires a percolated nanocrystal network, which can be achieved at high concentrations of the conductive material (*e.g.*, Si), but this inadvertently leads to nanocrystal sizes larger than the critical Bohr radius, resulting in loss of quantum confinement. On the other hand, if the concentration is low enough to preserve quantum confinement, most of the elements of the network do not interconnect, forming isolated islands. Without direct connections, conductivity has to rely on tunneling currents, which are extremely inefficient. This is a well-known conundrum, facing Si nanocrystals as a photovoltaic material.

However, a new hope emerges if one realizes that these seemingly mutually incompatible constraints can be favorably skewed by carefully adjusting the topology of the network formed by the nanocrystals. As we demonstrate here, if the threshold for quantum confinement can be pushed to higher Si concentrations, and, in addition, the threshold for electrical percolation can be pulled towards lower Si concentrations, a range of Si concentration values opens up, within which both the microscale and the atomic scale properties are satisfied simultaneously (Fig. 6b).

In order to lower the threshold for percolation, we have promoted anisotropic growth of the Si quantum dot network preferentially in the vertical direction (Fig. 6c). To this end, we resorted to ballistic deposition theory [38,60,61], which itself falls under the Kardar-Parisi-Zhang (KPZ) universality class [38,62], to guide our thinking for multiscale self-assembly: We performed thin-film deposition in a magnetron sputter system, where we kept the substrate at room temperature (the reader is referred to Chapter 4 for details). This way, we created a temperature gradient between the incoming “hot” atoms, which are energized by the magnetrons and the “cold” substrate, which is kept at room temperature. Because of this spatio-temporal temperature gradient, lateral diffusion of the hot atoms is restricted, which increases the probability of atoms being stacked up in the vertical direction, relative to the

horizontal, resulting in self-assembly of an anisotropic 3D random network of silicon quantum dots in the microscale.

In order to increase the threshold for quantum confinement, we have managed to create and stabilize a nominally unstable medium, composed mostly of suboxides (SiO_x), which surround the percolated Si quantum dots (Fig. 6d). The use of a cold substrate not only promotes vertical growth over the horizontal, but it also serves as crucial leverage for the creation and stabilization of the suboxides by forcing the adatoms to settle at minimum energy positions within a few nanometers of their collision points, instead of seeking out the global minimum over larger portions of the surface (Fig. 6e and 6f). This way, Si and O atoms are trapped into a random network that is being braid during fast stochastic deposition, which results in locking the suboxides into their non-global equilibrium states. Normally, when sufficient energy is applied to the system (generally by post-annealing at high-temperatures to promote the crystallization), suboxides break down and turn into stable forms of either Si or SiO_2 through a disproportionation reaction:

$$SiO_x \rightarrow \frac{x}{2} Si + \left(1 - \frac{x}{2}\right) SiO_2. \qquad \text{(Eqn. 2)}$$

If too many suboxides turn into Si, they inflate the effective quantum dot diameter, which eventually destroys the quantum confinement. In the other extreme, if too many suboxides turn into SiO_2, they surround and isolate the quantum dots, which have to, once again, rely on inefficient tunneling currents for conduction. The key issue is, then, to obtain nominally unstable suboxides and to prevent them from turning into stable forms of Si and SiO_2 completely upon addition of external energy thereby limiting further growth of quantum dot diameters. This way, a larger number of small-size quantum dots are obtained instead of a smaller number of large-size quantum dots in a given volume, which more readily form a percolated network due to increased density of connections.

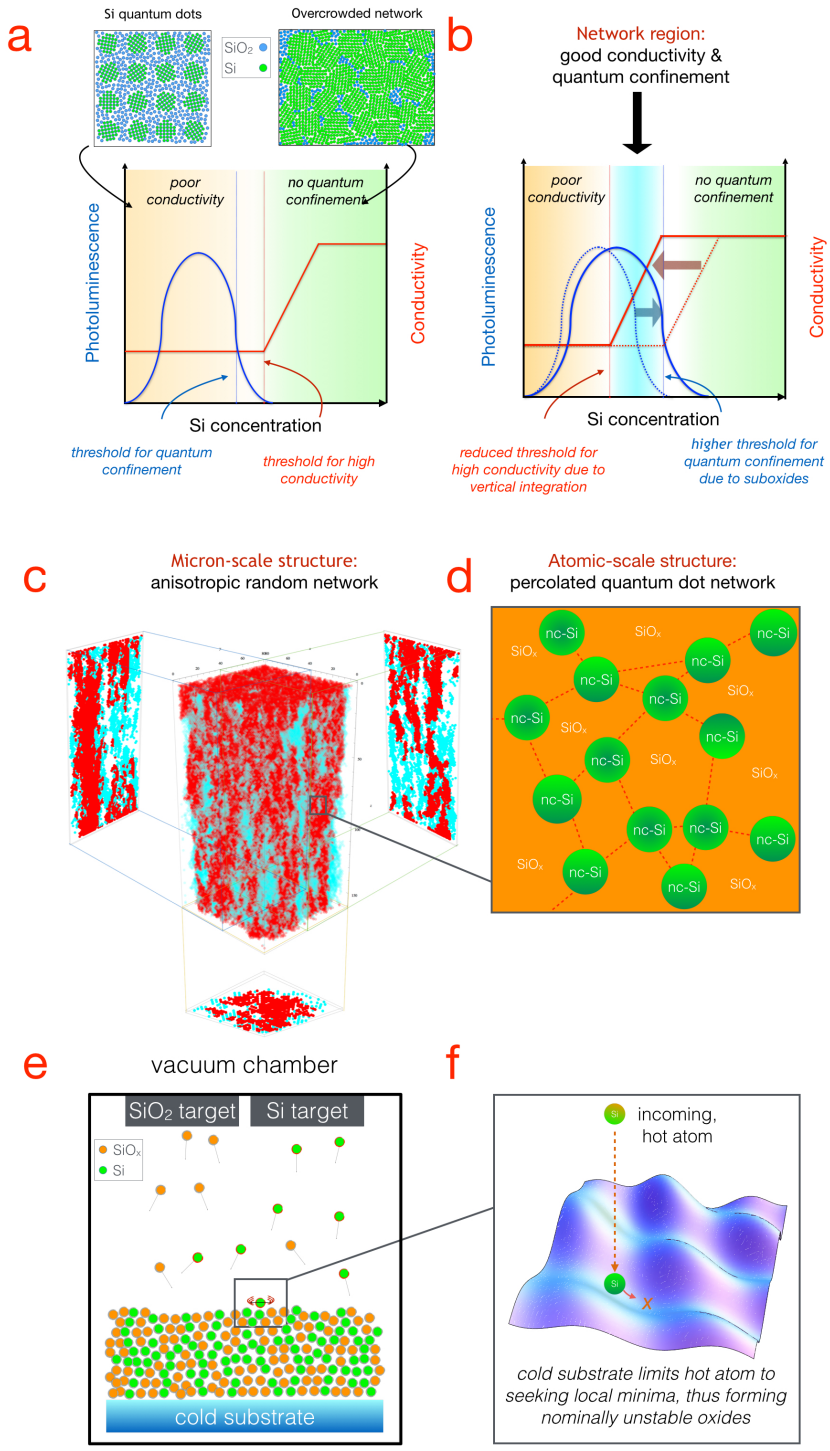

Figure 6 Sketches of dependence of photoluminescence and electrical conductivity on Si concentration: **(a)** for regular Si nanocrystal structures, regions of quantum

confinement and high conductivity do not overlap and **(b)** for the anisotropic random network of quantum dots as demonstrated here, a region of quantum confinement and high conductivity emerges. **(c)** Microscale anisotropic random network structure, showing its preferentially vertical alignment. Red and cyan dots indicate electrically percolated and isolated Si quantum dots, respectively. **(d)** Atomic scale illustration of the random network, where suboxides surrounding the quantum dots prevent overgrowth of quantum dot diameter. **(e)** Schematics of the deposition chamber. **(f)** Incoming hot atoms lose most of their kinetic energy upon collision with the cold substrate and are confined to a local energy minimum within a few nanometers of their impact points.

As it is explained earlier, good electrical conduction requires a percolated network of nanocrystals. Percolation is the spontaneous emergence of macroscopic connectedness in a network of randomly distributed connections, when a critical threshold in the density of the connections is exceeded (Fig. 6a and 6b) [63,64]. Percolation is a ubiquitous phenomenon, a random process that describes the behavior of connected clusters in a random graph. It is observed in countless real-world concepts [38, 63-79], such as neural networks (Fig. 7a) and nervous systems, propagation of a crack in a broken glass (Fig. 7b), airline flight connections (Fig. 7c), human social networks (Fig. 7d), the world-wide-web (Fig. 7e), ancient game of Go (Fig. 7f), drawings of the famous Dutch artist M. C. Escher (Fig. 7g), and so on. Figure 7 shows real-world examples to percolated random networks that have no physical relation to each other but they show similar behavior. Percolation theory provides a very simple mathematical model to understand such random events, as such predictions drawn by this theory are being used in many real-world applications, ranging from monitoring of epidemic diseases, to preventing the spread of forest fires, to mapping the credit networks and bankruptcy avalanches, to learning procedure of the brain, to the emergence of language, to coevolving ecosystems, and so on [38, 63-79].

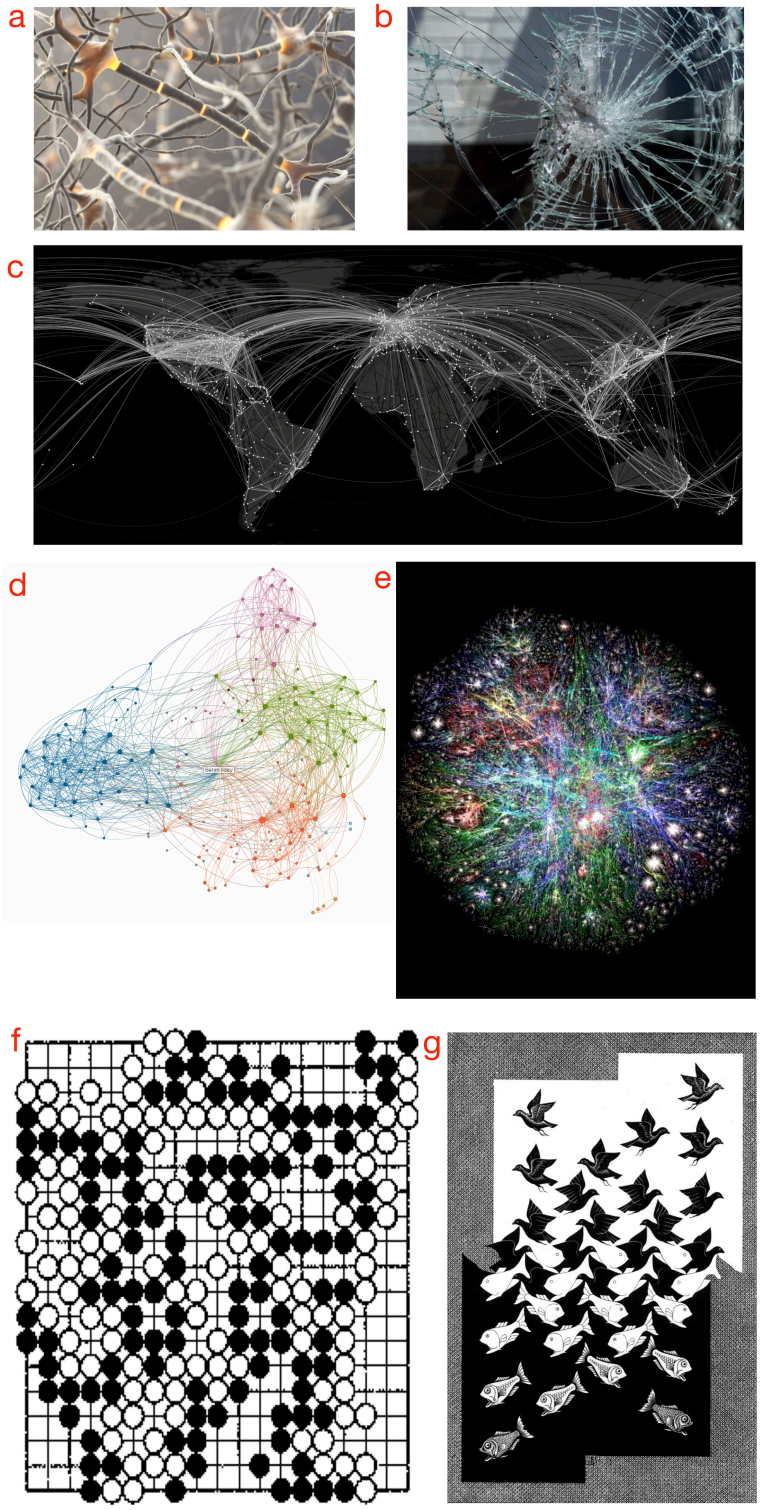

Figure 7 Real-world examples to percolated random networks: **(a)** Illustration of a neural network [72]. **(b)** Image of a propagation of a crack in a broken glass [73]. **(c)**

Map of the airports in the world with connections between them [74]. **(d)** LinkedIn social network map of the author of this thesis. **(e)** Map of the World Wide Web [75]. **(f)** Game of Go. White: Nakano Citoku, Black: Honinbo Genjo, played on November 17, 1804 in Shogun's Palace [76]. **(g)** Drawing from M.C. Escher – Sky and Water II, 1938.

Percolation has also entered popular culture. In Season 2, Episode "Soft Target" of a television crime drama called "Numb3ers" a mathematician working with the FBI is using percolation theory to help locate the person who released potentially lethal gas into the Los Angeles subway system. Percolation can also be heard in the form of interacting loops in Bach's gentle melodies [77]. Another popular culture example is the famous theatrical play, which has later been adapted to a movie, called "Six degrees of separation", where the play and the movie ruminates on the idea that everyone and everything is six or fewer steps away, by way of introduction, from any other person in the world. The idea was originally conceived of by the Hungarian author Fridges Karinthy, the abstract of which has captivated many scientists over decades. As a result of technological advances in communications and ease of travel, friendship (social) networks can grow larger and span greater distances. The modern world is "shrinking" due to this ever-increasing connectedness of human beings. Despite great physical distances between individuals all over the globe, the increasing density of human networks made the actual social distance far smaller. Percolation of random networks and its implications are also beautifully explained in the seminal books of Douglas R. Hofstadter: "Gödel, Escher, Bach: An eternal golden braid" and "I am a strange loop" [77,78]. Furthermore, it is intriguing to read many real-world examples of the theory from the popular science books such as "Linked: The new science of networks" by Albert-László Barabási [65] and "How to create a mind" by Ray Kurzweil [79].

Similarly, under the right conditions, an electrical network for which most of the nodes are connected to one another can emerge among randomly distributed silicon nanocrystals in a dielectric host matrix and this percolated network can efficiently transport the charge carriers, fulfilling the requirement of good electrical conductivity [63,64]. This is illustrated in Fig. 8a: The black dots represent silicon nanocrystals that are randomly scattered between the two electrodes (black, solid lines at the top and the bottom). Although there are small clusters, the elements of which are connected to each other (indicated by the circles), they do not contribute to the conductivity, as they remain isolated. The reason is that there is simply not enough nanocrystals to form a large connected cluster that can bridge the top electrode to the bottom electrode. On the other hand, when the number of dots is increased beyond a critical concentration, they interconnect and form a network that bridges the two electrodes (Fig. 8b). The conductivity along this network is colored red. Fig. 8c summarizes the sketches: $\theta(p)$ is the percolation probability, p is the occupation probability, and p_c is the critical probability. As can be seen from the graph, below p_c, ($p < p_c$) there are few connected clusters and individual dots that are not close enough to percolate. Above a certain threshold, p_c, *($p > p_c$)* these distant dots and clusters suddenly interconnect to form a fully percolated network. It is important to note that despite the random nature of the problem, and consequently, the value of p_c is defined as an average of an ensemble of such generated networks, the distribution of p_c is quite narrow and is quite specific. This sudden emergence of a global characteristic, connectedness or conductivity, in our case, beyond a certain critical point is the thumbprint of percolation theory. Further details on percolation theory can be found in ref. [63,64].

As mentioned above, the conundrum is that the high concentrations of silicon required for achieving percolation cause effective diameters of the nanocrystals to swell beyond the critical exciton Bohr radius (~5 nm for silicon), which ruins quantum confinement (Fig. 6a). Attempts to control silicon nanocrystal percolation by tuning stoichiometry are well known [16,52,80-85], but it was not clear *a priori*

whether quantum confinement could be preserved, as required for a tunable bandgap, while simultaneously forming a percolated random network that can efficiently transport the charge carriers. In other words, the challenge has been to engineer the material system such that there would be a reasonably broad range of Si concentrations, for which the percolation threshold is exceeded, while the exciton Bohr radius remains below the critical level (Fig. 6b). As we qualitatively demonstrated in Fig. 6c and 6d, our solution to untangle the mutual dependency of desired features in multiple length scales is through synthesis of a high-order, complex morphology that is of the form of an anisotropic 3D random network of silicon quantum dots.

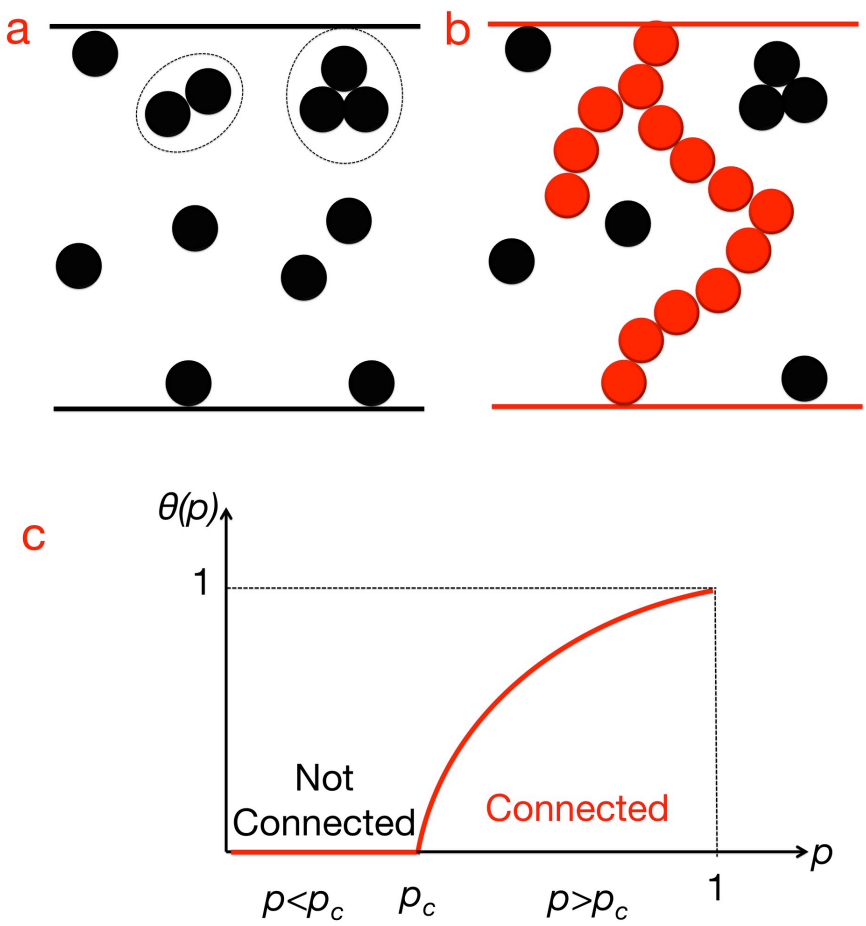

Figure 8 Sketches showing **(a)** individual dots along with small cluster of connected dots (black) that do not contribute to the conductivity between the top and bottom electrodes (black solid lines), and **(b)** a percolated network (red) along with individual dots and small clusters (black) that contribute to the conductivity between the top and bottom electrodes (red solid lines). **(c)** Graph showing percolation probability, $\theta(p)$, with respect to the occupation probability, p.

CHAPTER 3

SELF-ASSEMBLY IN MULTIPLE LENGTH SCALES: BRIDGING THE NANOSCALE TO THE MICROSCALE

"This idea that there is generality in the specific is of far-reaching importance."
- Douglas R. Hofstadter, Gödel, Escher, Bach: An Eternal Golden Braid, 1979

How did the life originate? How did it branch into immensely diverse forms? How is a human being related to, *e.g.*, a banana? These are some of the very basic questions that we are desperately trying to answer. According to an educated guess based on current scientific knowledge, emergence of life and its divergence into extraordinary forms happened mostly in thermodynamic equilibria through self-assembly. Self-assembly is simply the spontaneous, reversible transformation of basic units (building blocks) from a disordered to an ordered system through local interactions (van der Waals, capillary, π–π, hydrogen bonds) in order to form an organized, functional structure and/or to perform a specific task [40]. Lego, the construction toy, is a great analogy (even though they require an external agent to assemble). Lego structures basically consist of simple interlocking bricks (building blocks) of various types and colors (Fig. 9a) that can be assembled in many ways (Fig. 9a-c). Figure 9a shows a very simple ordering of the building blocks, however *complex multifunctional systems* require *hierarchical self-assembly* as can be seen from Fig. 9b and 9c, where Fig. 9d demonstrates self-assembly of a biological system as a real-world example. It goes without saying that bridging the smallest possible scale to the largest possible scale without disturbing their scale-dependent features is extremely important, where hierarchical self-assembly, with different topologies and different solutions at different scales (*i.e.*, hierarchies), introduces the additional degrees of freedom required to satisfy multiple constraints. In fact, the significance of hierarchy

can hardly be overstated when features belonging to or arising from different size scales need to be tackled.

Consider how various biomolecules form a nonequilibrium, complex network that constitutes a cell and how numerous cells are co-linked in myriad ways to form a biological organism, numerous kinds of which further interact to form an entire ecosystem. At every scale, functionality effortlessly emerges from one lower scale, through stochastic processes, often regulated by multiple nonlinear feedback mechanisms. In this chapter, we provide only the essence of the self-assembly concept without exploring it thoroughly. However, we suggest further readings on the subject for those who are interested, such as ref. [38,40,65-71,86].

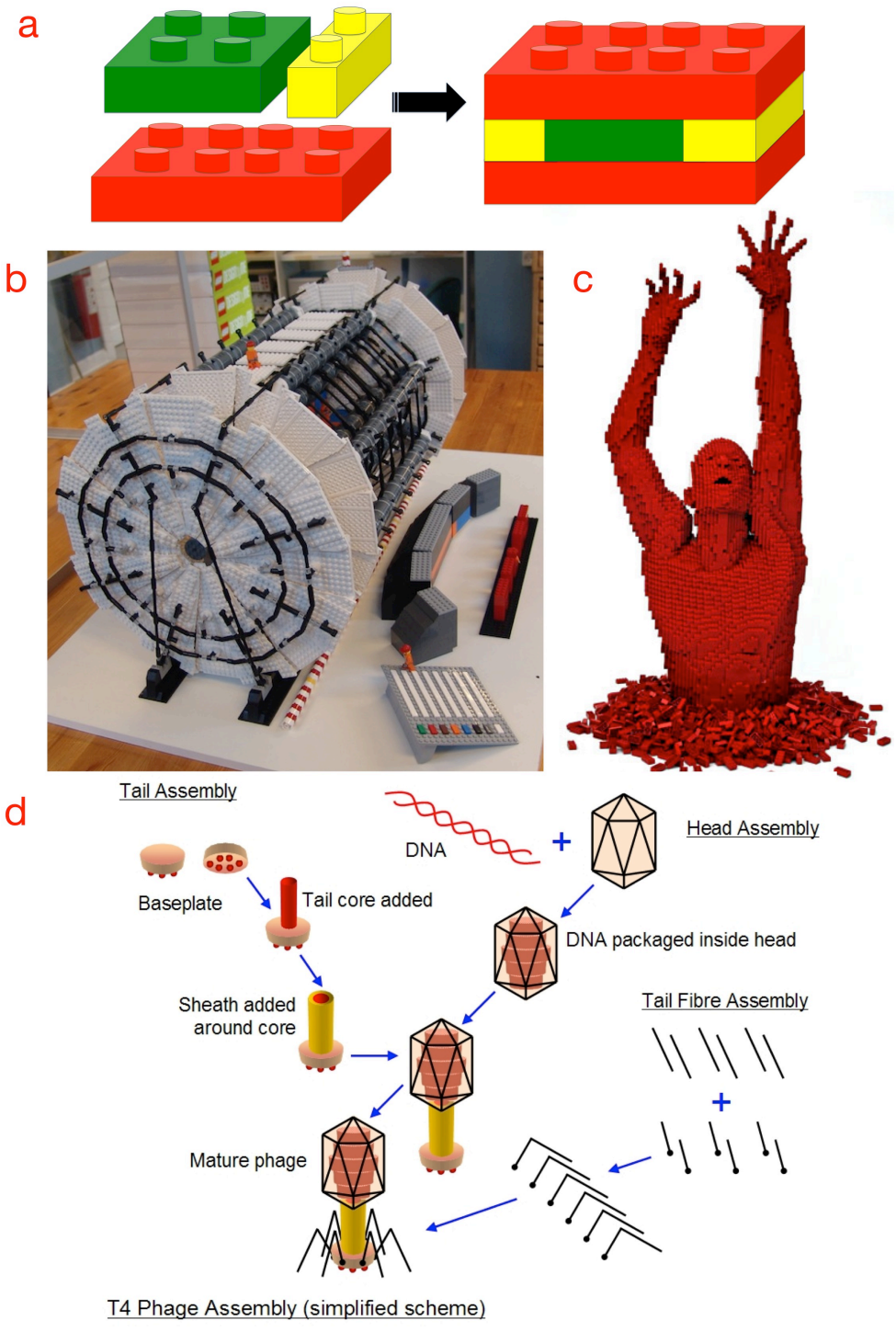

Figure 9 Lego, the construction toys, as an analogy to self-assembly process. Sketches showing **(a)** simple interlocking Lego bricks (building blocks) that are assembled into an ordered form. Images showing **(b)** a model of the Large Hadron

Collider (LHC) assembled using Lego bricks [87], and **(c)** an artwork created entirely from Lego bricks [88], as an example to hierarchical self-assembly to create complex structures. Sketch showing **(d)** the assembly of a virus from its building blocks, as an example to hierarchical self-assembly observed in the biological world [89].

3.1 Directed/Guided Hierarchical Self-Assembly

When material dimensions are decreased to nanoscale, they can exhibit entirely different properties compared to their bulk counterparts. We know now that not only size and shape makes the difference but also topology and connectedness plays a significant role in a material's electronic, optic, magnetic, and structural properties. Indeed, there is a whole new paradigm, whereby ensembles of nanostructures exhibit new features as a result of interactions between the individual building blocks [5,7-9,11,13,23]. Of course, potential use of various topologies with related features in many applications rely on our ability to understand and control the electronic, optical, magnetic interactions between the individual building blocks along with our capability to exploit their collective properties. Let us explain this using an example from popular culture: The Borg in the famous science fiction franchise Star Trek. The Borg is an interconnected "Collective," a network of billions of humanoid "nodes" from originally numerous different species in the Star Trek universe. Each "node" of the network was "assimilated" during an encounter with the Borg. The Borg absorbs the biological and technological distinctiveness of these species and adds them to its own in pursuit of perfection, at the expense of turning individuals into cybernetically enhanced humanoid drones, who no longer exhibit their individualities but are linked to the collective mind by subspace radio. The Borg acts as a single entity, and constitutes a hive mind. This way the capabilities of the Borg exceed the capabilities of any species in their neighborhood (of the galaxy). These assimilations give the Borg great technological superiority and the Borg uses it frantically in its quest towards "perfection". However, the Borg is not completely

uniform either, it is organized in hierarchical sub-units, each of which form different functions and can adapt to evolving conditions, even though the “nodes” are all similar (equivalent) in capacity and functionality. As in the Borg example, ensembles of individual building blocks can demonstrate distinctive advanced features over its individual constituents, especially when organized hierarchically to demonstrate different functions or features through different topologies of assembly at different hierarchical (often delineated by scale of size) levels. This is ubiquitous in natural, particularly biological systems, so it should be possible to exploit and use these principles to gain tremendous technological advancements, particularly in nanomaterial design and synthesis.

Self-assembly techniques offer simple and low-cost methodologies, generally applicable to wide range of materials. It often also ensures the fabrication of robust, stable, highly reproducible, long-range ordered complex topologies with well-defined sizes, shapes, aspect ratios, and chemical heterogeneity, which is vital for such applications [5,8-11,13,20-23,37,39,40,86]. Self-assembly is the most appealing way to fabricate stable and highly reproducible morphologies with precise control over their long-range orders [5,13,22,23,36]. However, the structure has to spontaneously emerge since the interplay and feedback between the complex topology and network dynamics, which is not understood thoroughly and they are difficult to control [6,13,33-35]. Self-assembly of complex structures observed in real-world examples are mostly emerged in thermodynamic equilibria that took millions of years, a luxury man-made systems do not have in the quest to score technological advancements through multifunctional complex structures. Thus, we have to explore nonequilibrium conditions and nonlinear mechanisms to direct the ensemble of the building blocks towards versatile forms and functionalities since the output of a nonlinear system is not directly proportional to its input. Spontaneous emergence of complex topologies through self-assembly generally requires nonequilibrium conditions under which the dynamical evolution of the system can bifurcate without requiring deliberate intervention and can be partially steered

through addition of an external energy or force [10,13,21,23,37], such as compressive or shear stresses, gravity, magnetic or electric fields, flow, and confinement or influence of thermal gradients, as in our case. Also note that in Fig. 9, unlike real-world examples, the Lego bricks do not "self-assemble" but require an external force, us, to direct/guide the assembly. By directed/guided self-assembly one can create structures in multiple sizes, pitches, and order in a single material system through a single layer process, which has the potential to replace lithography and to be used in next-generation technological devices (Fig. 10).

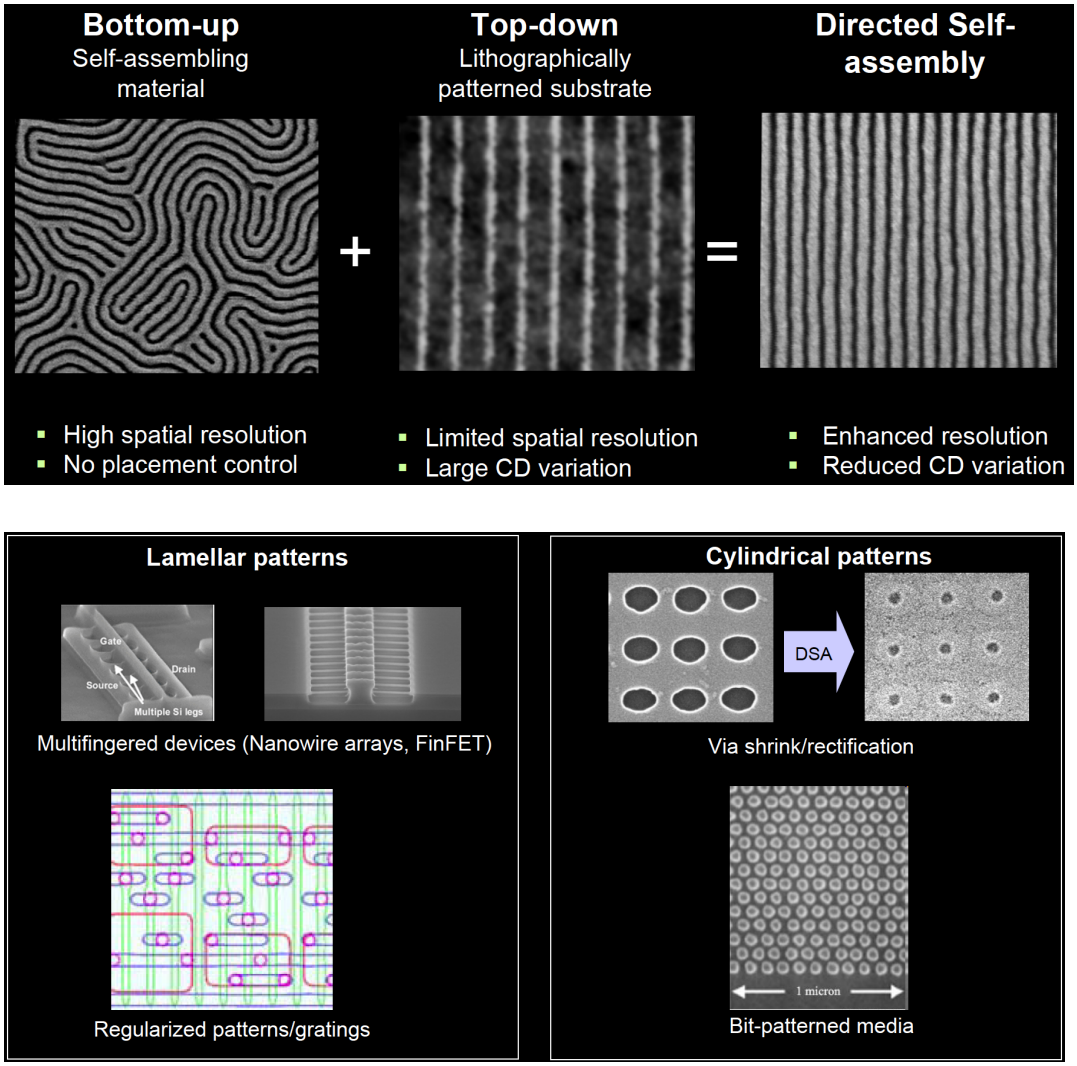

Figure 10 Examples to the directed self-assembly. (Top) Images showing the differences between (left) self-assembling block copolymer on a homogenous surface, (middle) patterned block copolymer on a lithographically patterned surface, and (right) directed block copolymer self-assembly. (Bottom) Potential applications of directed block copolymer self-assembly of lamellar and cylindrical patterns to electronic devices [Courtesy of IBM] [90].

Spontaneous self-assembly under nonequilibrium conditions requires a disturbance in the balance through spatio-temporal gradients in temperature, pressure,

concentration, viscosity, chemical potential, etc. Surely, the growth or emergence of the desired structure cannot continue infinitely, but it has to be fixed in a determined time and space to produce persistent, stable structures [5,8-11,13]. In other words, there should be feedback mechanisms (for "self" action); a positive feedback promotes the growth and organization and a negative feedback limits the growth and stabilizes the structure. It is utmost important to control these feedback mechanisms in order to control the self-assembly process. An example can be found in our recent paper [33], where we have demonstrated positive nonlocal feedback to initiate, and negative local feedback to regulate and stabilize, the growth of ultrafast laser-induced metal–oxide nanostructures with unprecedented uniformity, at high speed, low-cost and on non-planar or flexible surfaces. This process is summarized in three steps:

(1) The laser beam, with peak intensity close to the ablation threshold for the target material (*e.g.*, titanium), is focused on the surface, where it is scattered by existing nanostructures or any surface defects. The interference of the scattered and incident fields leads to intensity variations in the immediate neighborhood of the scattering point.
(2) At points where the threshold intensity for ablation is exceeded, titanium reacts rapidly with oxygen from the air, forming titanium dioxide. The use of ultrashort pulses is necessary to ensure this process occurs faster than heat diffusion, as this can smear out the nanoscale localization of the deposited laser energy. The first two steps constitute a positive feedback loop. As the nanostructure grows, so does its scattering power.
(3) The growth mechanism also has an imbedded negative feedback loop. As titanium dioxide grows on top of the titanium, penetration of oxygen through the oxide layer decreases exponentially, decelerating and eventually halting the growth process.

This is a feat that could hardly have been performed through traditional approaches with simplicity that the self-assembled process has afforded us. However cleverly chosen three simple rules or processes succeeds in generating extremely uniform nanostructures.

The hierarchical self-assembly of anisotropic 3D random network of silicon quantum dots presented in this thesis is formed from a silicon-rich siliconoxide thin-film. Since hierarchical self-assembly of such a complex system cannot be achieved in equilibrium conditions, we have employed nonequilibrium conditions, whereby we set the "rules" of stochastic growth without trying to manipulate every dynamical detail of the system, similar to our recent work with laser-induced nanostructures, as described above. Microscale self-assembly of the vertically aligned random network is kinetically driven under nonequilibrium conditions established by magnetron sputter deposition and relies on control of surface diffusion through a temperature gradient on the surface. Atomic scale self-assembly of the percolated quantum dot network is chemically driven under local nonequilibrium conditions provided by the fast stochastic deposition process and relies on control of phase separation by creating and stabilizing a nominally unstable medium, which is composed mostly of suboxides (Fig. 6). Further details of the microscale and atomic scale self-assembly of this complex network along with the driving forces of the multiscale self-assembly can be found in Chapter 6.

3.2 Kardar, Parisi, Zhang Universality and Ballistic Deposition

From a practical point of view, it is not only impossible, but also completely unnecessary to manipulate each and every building block one by one towards their self-assembly in multiple length scales. There should be an easier way to do that, which should be largely independent of the type of the starting material and initial conditions. That way, system-generated constructional pathways can depend on several basic rules and generate the same pattern in vastly diverse physical systems over and over again [5,8-11,13,20-23, 40,86]. For example, Uriel Frisch, Brosl

Hasslacher and Yves Pomeau demonstrated in 1986 that it is possible to emulate the Navier-Stokes equations that describe fluid flows using a cellular automaton of gas particles on a hexagonal lattice. This is much simpler description based on simple translation and collision rules that govern the motion of the particles. It is striking that an extremely simplified cellular automata-based microscopic description can be accurate and even yield physically correct results in agreement with the macroscopic description provided by the Navier-Stokes equations. This can be understood by realizing that the Navier-Stokes equations obey corresponding conservation laws and are largely insensitive to microscopic details, as long as the microscopic dynamics implements the relevant symmetries correctly [40,91].

Let us give you another analogy from the sociology: Crowd behavior. An ant is different than a bird or a fish or a human or a star or a broccoli bud. However, the collective behavior of an ant colony, a bird flock, a school of fish, human crowds, a galaxy or a romanesco broccoli shows the strikingly similar patterns (Fig. 11): In the absence of any centralized control, micromanaging how individuals should behave, but when these individuals or constituents move and interact with each other randomly, following simple rules, this leads their self-organization, which exhibits global characteristics that the individual constituents (including people) are not aware of [92,93]. In order to understand the mechanism behind such an identical behavior seen in a large class of interacting complex networks, which turns out of to be largely independent of the dynamical details of the system, we have to categorize and quantify it through the concept of "universality".

Simply put, *universality* is the typical behavior seen in a large variety of complex physical systems. These systems are diverse, from a crystal lattice to the Internet, arising when a large number of interacting parts come together. While individual components are important, sometimes even dominant in many, particularly small systems, in sufficiently large systems, typically, no single component can assert a dominating influence on the final state of the system. [35,38,62,66,91]. But how

large a system should be to exhibit universality? Consider four people talking, voices of each individual can be distinguished and affect the conversation. Increase the number to ten people who are talking at the same time. It is much harder to follow their voices but you can still distinguish them. Now, consider a crowd talking, you will notice that the voices of individuals are washed out and blend into a noise. So, a large, complex system demonstrates universality in a scaling limit, when a critical point, a threshold is reached in its parameters such as the concentration, density, temperature, magnetization, and so on. However, close to their critical points, a great many physical systems have been shown to exhibit strong similarities, when they share the same essential symmetry or symmetries. Various global characteristics turn out to be independent of microscopic details, but on the symmetries, dimensionality of the system and the range and type of interactions between the microscopic constituents [35,38,62,66,91].

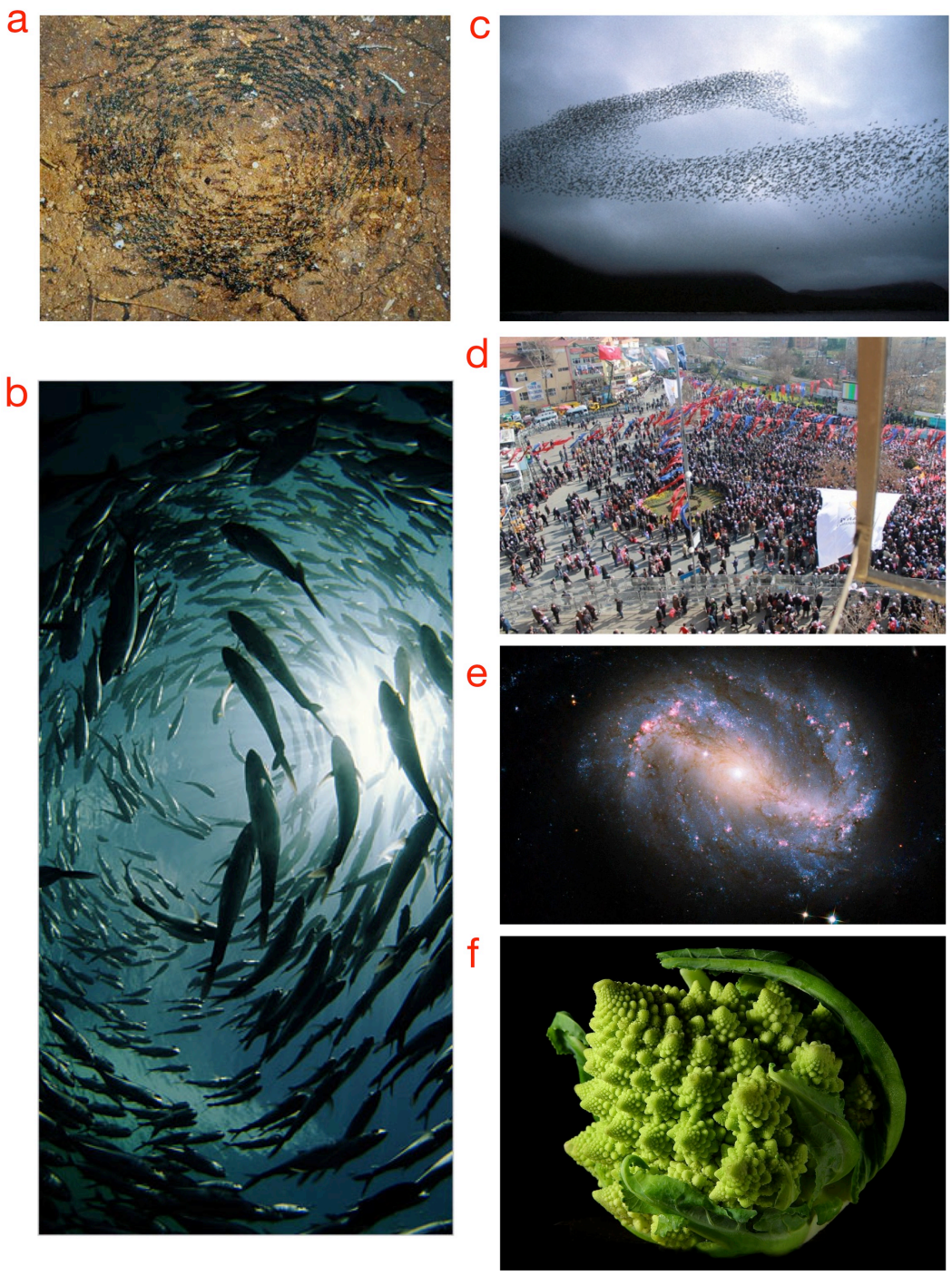

Figure 11 Real-world examples to systems exhibit universality. Images showing **(a)** an ant colony, **(b)** a school of fish, **(c)** a flock of birds, **(d)** a human crowd, **(e)** Barred spiral galaxy NGC 6217, and **(f)** a romanesco broccoli.

Obviously, there is a vast number of complex systems that shows different behaviors and symmetries but many of them can be grouped into a set of universality classes, specified by the set of relevant observables: Same symmetry properties, same critical exponents, same scaling, and same functions [35,38,62,66,91]. An exhaustive description of all the universality classes or the details of relevant observables is beyond the scope of this thesis. Instead, we will briefly discuss about Kardar-Parisi-Zhang (KPZ) universality, which is directly relevant to this study. However, the reader who is interested can be referred to comprehensive review papers on the subject [38,62,94].

The KPZ universality class first introduced in 1986 by Kardar, Parisi and Zhang to classify the growth of interfaces in nonlinear, stochastic systems [38,62,94]. It is one of the interface growth classes, which models a number of physical phenomena [38,62,94] such as 1D random growth interfaces, crack propagation, stochastic Burgers equations, thin-film crystal growth, directed polymers in random environments, facet boundaries, stochastic Hamilton-Jacobi-Bellman equations, bacteria colony growth, interacting particle systems, stochastically perturbed reaction-diffusion equations, and turbulent liquid crystals, which could not be fully described by basic universality classes. All these phenomena display characteristic, though unusual, scalings: (in one spatial dimension) a roughness exponent $\alpha=1/2$, a growth exponent $\beta=1/3$ and a dynamic exponent $z=3/2$.

The KPZ universality class is described by the KPZ equation, which is a nonlinear, stochastic partial differential equation. It is one of the continuum equations that typically describe the interface growth at large length scales. This means that the transient state that leads to the asymptotic behavior is ignored, focusing on asymptotic coarse-grained properties [38,62,94]. It is basically the nonlinear form of the well-known linear Edwards-Wilkinson equation, where Kardar, Parisi, and Zhang added nonlinear term, $(\nabla h)^2$, to describe the lateral growth as fallows:

$$\frac{\partial h(x,t)}{\partial t} = \nu\nabla^2 h + \frac{\lambda}{2}(\nabla h)^2 + \eta(x,t), \qquad \text{(Eqn. 3)}$$

where $h(x,t)$ represents height of the growing structure at time *t*, position *x*. ν is the surface tension, λ is the coefficient of the nonlinear term, and η is the stochastic varliable, *i.e.*, noise. The first term on the right hand side describes smoothing/relaxation of the interface, the second term describes the lateral growth ($(\nabla h)^2$ is being the nonlinear term) and the third term is the noise, which accounts for the surface roughening. The time derivative of the height function depends on three factors: smoothing (the Laplacian), rotationally invariant, slope dependent, growth speed (the square of the gradient), and noise (spacetime white noise).

Let us explain the difference between the linear Edwards-Wilkinson and the nonlinear Langevin KPZ equations through the example of two stochastic growth models, namely, random deposition and ballistic deposition. Random deposition model is the simplest growth model, where particles fall onto a surface with a vertical trajectory and each particle lands on an empty site or on top of an existing column of particles (Fig. 12a). For each column, independent Poisson processes drive the growth, which means each column grows with no spatial correlation to its neighbors. Gaussian distribution governs the height distribution [38,62,94]. This can be explained by linear continuum equations such as Edwards-Wilkinson. Figure 12b shows a simple numerical simulation of the random deposition model, where bright columns have no relationship with each other and appear as stripes due to the lack of lateral growth. On the other hand, in the ballistic deposition model (Fig. 12c) the incoming particles that are also falling in a vertical trajectory, but they hit and stick to wherever they land. This can be an empty site on the surface, or on top of a column or to the corner or to the site of a particle. This way the structure starts branching on its sides, which allows growth along the substrate surface [38,62,94]. This breaks down the up-down symmetry of the interface height, which cannot be described by linear continuum equations but require nonlinear continuum equations such as KPZ. Figure 12d shows a simple numerical simulation of the ballistic

deposition model, where bright columns got thicker and they have branched to their sides (Note that the outcome of the ballistic deposition can be of various forms, ranging from fairly straight columns to fan-shape structures, the details of which will be discussed below). However, this side branching has its limits due to the fact that each column is dependent to each other, which means each column grows with a lateral correlation between them. Considering this correlation in surface heights and the finite size of the system, the width eventually saturates at a certain point. In this steady state the roughness fluctuates but the average value no longer changes with time, instead it scales with the size of the underlying substrate.

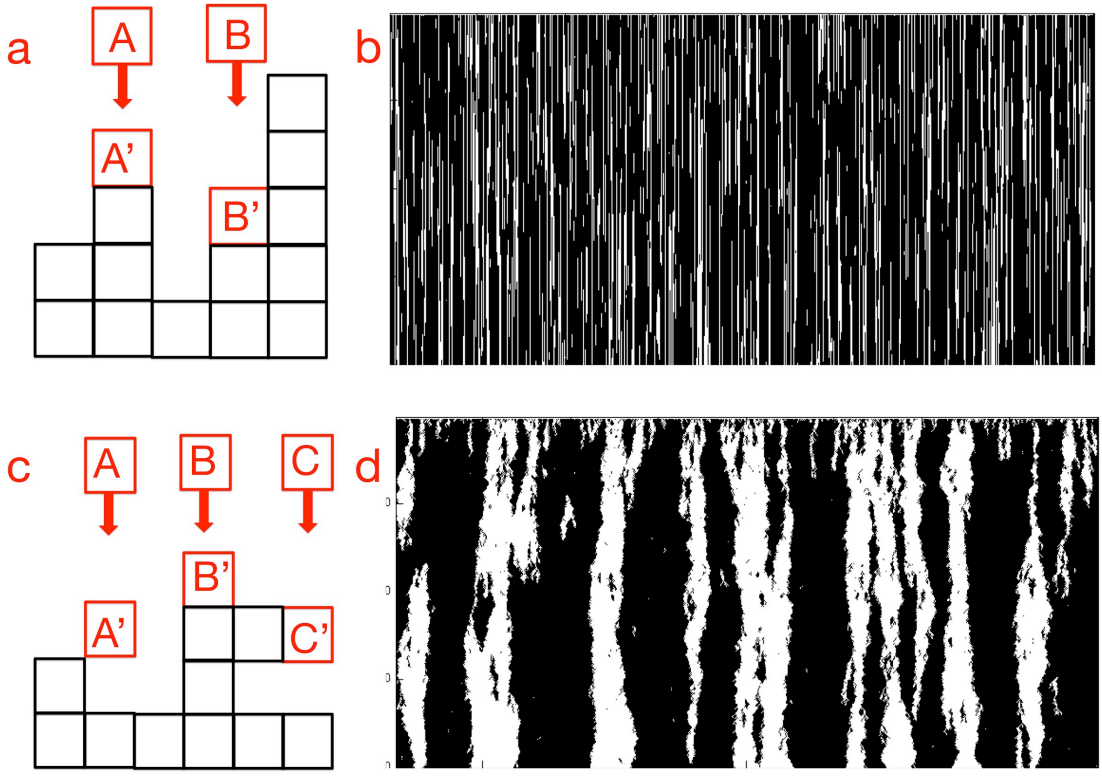

Figure 12 (a) Sketch showing random deposition model. **(b)** Numerical simulation for random deposition model. **(c)** Sketch showing ballistic deposition model. **(d)** Numerical simulation for ballistic deposition model.

As explained earlier in Section 2.2, we have resorted to ballistic deposition theory as it allows us to generate structures that have a tunable degree of anisotropy, which is related to the percolation threshold. We use this extra degree of freedom to untangle the mutual dependency of good electrical conduction and quantum confinement and create an anisotropic 3D random network of silicon quantum dots with fine-tuned anisotropicity. Using this approach, we not only promote vertical growth in the microscale but also we control phase separation through stabilized suboxides in order to preserve quantum confinement in the atomic scale. Employing ballistic deposition for multiscale self-assembly of such a complex structure makes perfect sense because it sweeps aside a large number of factors that influence the details of thin-film growth, but provides simple a couple of "rules" (with clearly identifiable corresponding experimental conditions) to determine the morphology. The two basic rules that we used are as follows (please refer to Section 2.2 and Fig. 6 for further details):

1. Creating a spatio-temporal temperature gradient on the surface achieved by keeping the substrate cold and adjusting how "hot" the deposited particles are by controlling deposition energies. This way, we control surface diffusion,
2. Fine-tuning of the stoichiometry through changing silicon concentration in order to control the phase-separation.

Ballistic deposition is a discrete algorithmic interface growth model at far from equilibrium for systems exhibiting dynamic scaling behaviors. Vold introduced the model in 1959 as a model of growth of colloidal aggregates by sedimentation [95]. According to this model, the film is grown on a substrate of finite size L, where particles are deposited randomly. The space is described as a mesh grid and time advances in discrete steps. Active growth sites are defined in relation to their nearest neighbors, where at least one neighbor must be a member (Fig. 12c). This requirement automatically introduces spatial correlation between neighboring particles on the surface. Most of the surface structures grown by ballistic deposition turn out to be self-similar, fractal structures *i.e.*, invariant under a scale

transformation. The width of the columns increases as a function of time while the surface of the growing aggregate roughens. This can simply be characterized by the following two quantities [38,62,94]:

(1) The mean height of the surface of the growing aggregate, $\bar{h}$, is defined by

$$\bar{h}(t) \equiv \frac{1}{L}\sum_{i=1}^{L} h(i,t), \qquad \text{(Eqn. 4)}$$

where $h(i,t)$ is the height of column *i* at time *t*.

(2) The surface width is the standard deviation of the surface height, which characterizes the roughness of the growing aggregate; *w* is defined by the root mean square fluctuation in the height.

$$w(L,t)^2 \equiv \frac{1}{L}\sum_{i=1}^{L}\left[h(i,t) - \bar{h}(t)\right]^2. \qquad \text{(Eqn. 5)}$$

Typically dynamical evolution of rough surfaces is characterized by the dynamical scaling of a correlation of the surface structures. The roughness of the interface initially grows with a power law dependence on time. Consequently, the spatial (surface) correlation length grows initially as a power of time. Once the entire surface is correlated, growth of both roughness and correlation length begin to scale. Not surprisingly, their values scales with the *L* of the underlying substrate. The values of these scaling exponents can be used to classify the different stochastic growth models. The roughness exponent is α, the growth exponent is β, and z is the nonequilibrium exponent, defined as $z = {}^{\alpha}/_{\beta}$. At the beginning of the growth process, the interface exhibits a power law dependence on time with the growth exponent, $W \sim t^{\beta}$. Later, when the interface growth begins to saturate, it is described

as a power law dependence on width with the roughness exponent, $W \sim L^{\alpha}$ and the nonequilibrium z exponent quantifies this dynamical behavior of the growing aggregate. As a result of these power law dependencies, the initial growth is self-similar in time and the subsequent stages of growth exhibit spatial self-similarity. This is by itself is not surprising either, since self-similarity is often observed in many natural phenomena. The identification of self-similarity in complicated, nonlinear systems can be particularly informative about the internal dynamics, since self-similarity arises after the influences of initial conditions have faded away, but the system is still far from its ultimate, equilibrium state [96,97].

We have referred to the "universal" nature of the ballistic deposition many times throughout this thesis, whereby the topology of the growing aggregate does not largely affected by its constituents or the initial conditions of the system, and rather behavior of the system is steered by a small number of factors. This is a key point, since those, few, crucial factors can possibly be manipulated to engineer the overall morphology. This way similar topologies and behaviors can be achieved for different materials, irrespective of their specifics. Figure 13 presents compelling experimental evidence for our claims, where electron microscope images exhibit strikingly similar morphologies for different kind of materials, namely, WO_3 [98], TiO_2 [99], Si [100], Pd [101], Co [102], and Ni [102].

Note that in addition to the fact that the structures shown in Fig. 13 are made of different kind of starting materials, these thin-films were also produced at different laboratories, with entirely different equipment and starting conditions. However, none of these details matters for the final topology, what matters is that the process is stochastic and it follows the simple rules described by ballistic deposition theory and leads to similar morphologies.

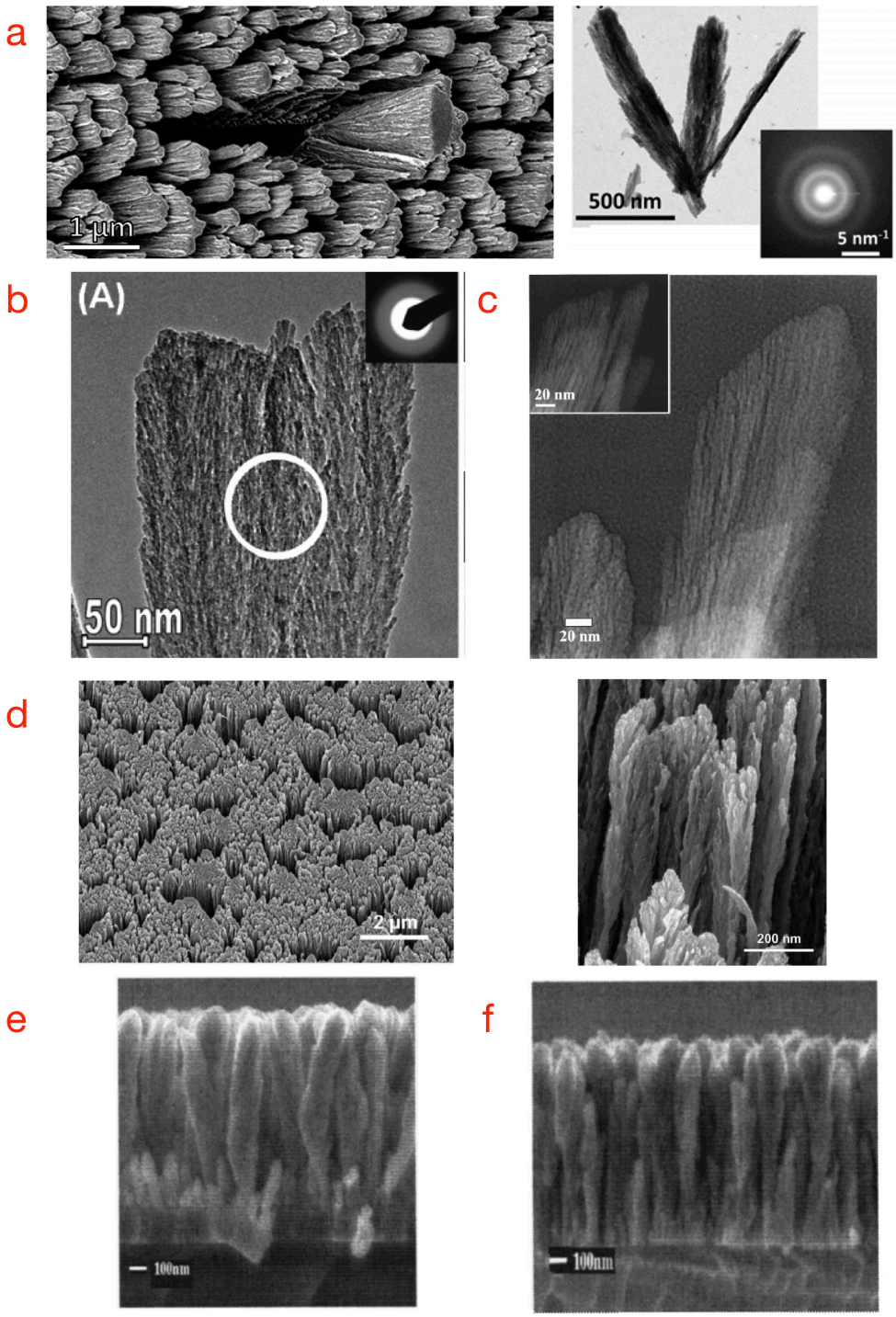

Figure 13 HRTEM and SEM images showing similar morphologies for thin-films of **(a)** WO_3 [98], **(b)** TiO_2 [99], **(c)** Si [100], **(d)** Pd [101], **(e)** Co [102], and **(f)** Ni [102] that were grown using conditions determined according to ballistic deposition theory.

We have also fabricated amorphous and nanocrystal silicon thin-films via ballistic deposition using an inductively coupled plasma-assisted chemical vapor deposition (ICP-CVD) system using H_2-diluted SiH_4 as the source gas, where we have observed fan-shaped silicon nanostructures as shown in Fig. 14, very similar to those shown in Fig. 13. The presence of universality does not imply lack of adjustability. Small or large modifications on the final morphology can be made by adjusting the deposition conditions such as substrate temperature [98-105], energy of the incoming particles [103], deposition pressure [105], concentration [104], angle of incident flux [103], and rotating the substrate [100]. What invariant is the essential of the resulting geometry of the topology, which is best described by the scaling coefficients.

As an example to the small modifications that can be deliberately imposed on the final morphology, we show in Fig. 14a an aggregate of Si:H fan-shaped structure and an individual Si:H bundle splatted from this aggregate in Fig. 14b. Another bundle of Si:H is shown in Fig. 14c, which is fabricated under different deposition pressure than the one shown in Fig. 14b. It is seen that the morphology does not change dramatically by changing the deposition pressure; rather the structure simply smoothens, but preserving the overall topology.

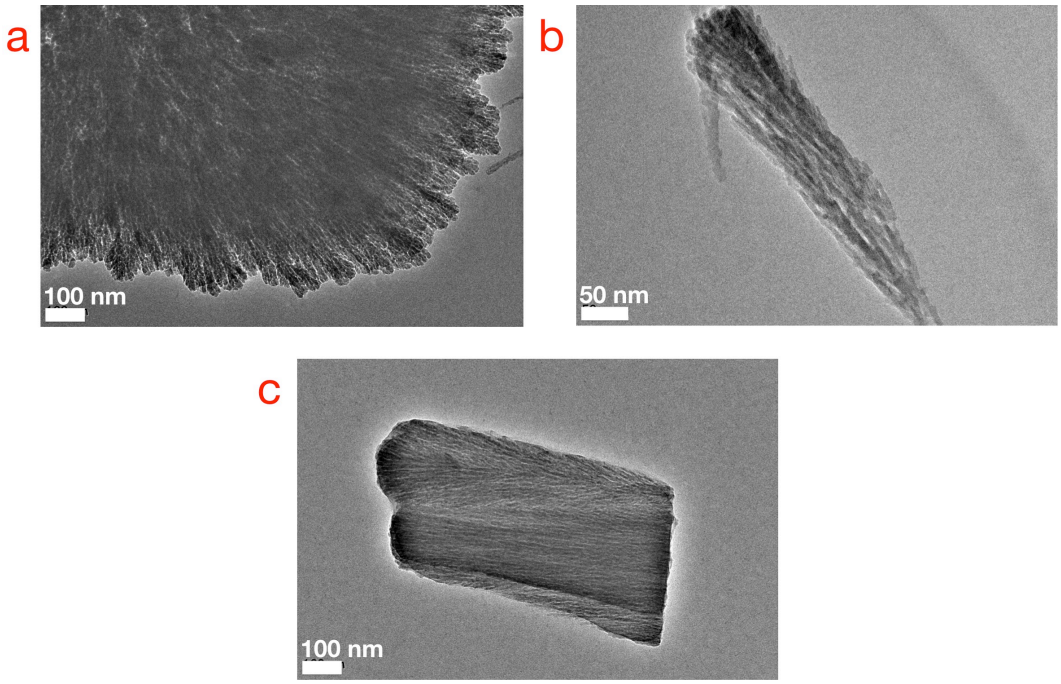

Figure 14 HRTEM images showing fan-shaped Si nanostructures fabricated via ballistic deposition using an ICP-CVD equipment. **(a)** An aggregate of Si:H fan-shaped structure and **(b)** an individual Si:H bundle splatted from the aggregate. **(c)** An individual Si:H bundle fabricated with different deposition pressure showing a smoother fan-shaped structure [105].

There are also interesting studies that report large modifications on the final morphology such as helices (Fig. 15a), rods (Fig. 15b and 15c), and zigzag patterns (Fig. 15d), which are obtained by simply changing the angle of incident flux.

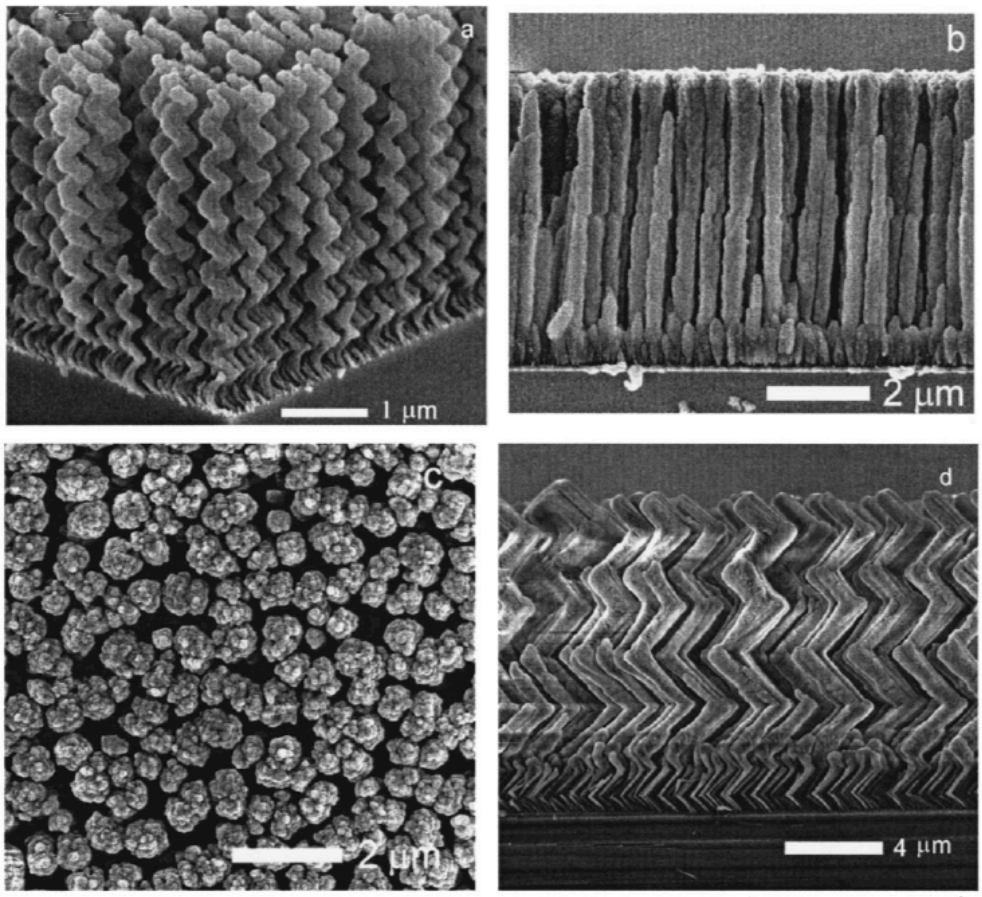

Figure 15 SEM images showing various morphologies for thin-films that are deposited using ballistic deposition theory [103]. **(a)** Helices deposited using an incident flux at $\boldsymbol{\theta = 85°}$, **(b)** rod structure deposited using an incident flux at $\boldsymbol{\theta = 85°}$, **(c)** top view of the rod structures shown in (b), **(d)** zig-zag structures deposited using alternating left and right incident flux at $\boldsymbol{\theta = 86°}$.

Lastly, we have compared ballistic deposition of silicon nanocrystals using ICP-CVD (Fig. 16a) and anisotropic 3D random network of silicon quantum dots that we have fabricated using PVD (Fig. 16b) (please refer to Chapter 4 for more details on the fabrication methodology). Note that the ICP-CVD thin films contain only one component, Si, on the other hand, PVD thin-films contains two components, Si and SiO_2.

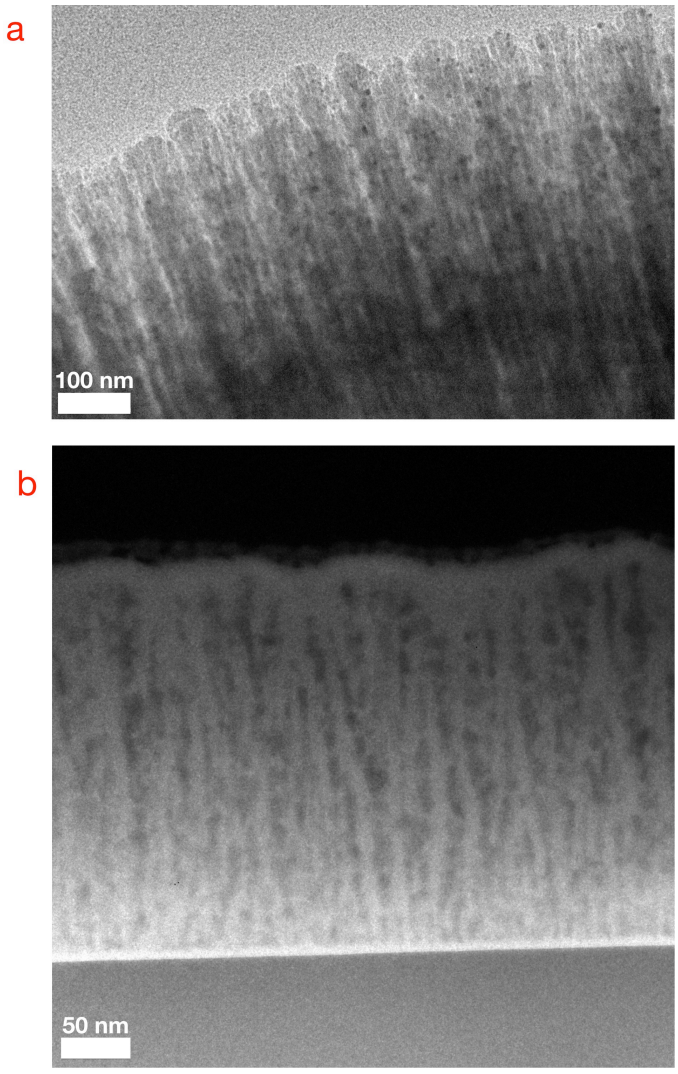

Figure 16 TEM images showing the morphological differences of the ballistic deposition of **(a)** a single component thin film composed of Si fabricated using ICP-CVD [105] and **(b)** a two-component thin film composed of Si (dark) and SiO_x (bright) fabricated using PVD [104].

As can be seen from the figure the morphology is substantially modified when two components are used for ballistic deposition. The single-component structure is highly porous and it is composed of individual fan-shaped bundles (Fig. 16a). In contrast, the two-component structure shows vertically oriented individual columns

that are branched sideways (Fig. 16b). Moreover, the structure shown in Fig. 16b is more robust and long-term stable compared to the structure shown in Fig. 16a. The detailed results on the ballistic deposition of silicon-rich silicon oxide thin films can be found in Chapters 5 to 7.

CHAPTER 4

METHODOLOGY

"Before the Gates of Excellence the high Gods have placed sweat."
- Hesiod, Works and Days

4.1 Thin-Film Fabrication and Post-Annealing Procedure

Most of the research in self-assembly involves chemical processes, meaning the desired structures are fabricated within a solution. Although thin films are technologically more relevant, there are very few studies on the subject, presumably because self-assembly of thin-film structures is commonly believed to be difficult to synthesize and to control. On the contrary, we believe that thin-film fabrication methods offer great advantages in achieving multiscale self-assembly since they provide readily stochastic deposition under nonequilibrium conditions, along with convenient control of several key experimental parameters, in particular those that control the thermodynamic conditions. Thus, it was only logical for us to use magnetron-sputtering technique as the fabrication method, since it provides extremely uniform, smooth films, where film properties can be controlled easily. Magnetron sputtering process simply relies on the momentum transfer between the atoms at the surface of the “target” material and inert gas ions that are accelerated to the target surface (Fig. 17): Once released into the vacuum chamber, gas atoms are ionized by the magnetrons and confined in a magnetic field close to the target material, where they collide with the target surface atoms and jettison them [106].

The magnetrons create a magnetic field parallel to the target surface once an electric field perpendicular to it is applied. This helps establish a magnetic field in the vicinity of the target surface, where secondary electrons (byproducts of gas

ionization) are confined and constantly colliding with the gas atoms to create more ions and more secondary electrons. Upon returning to their ground energy state, these excited electrons release photons, which is the reason behind the characteristic plasma glow. Although more gas atoms means ionization of atoms, there is a limit to this, due to the amount of gas introduced into the system. "Mean free path" is the typical distance that an ejected target atom will travel before without colliding with another atom or molecule, which has to be larger than the distance required to reach to substrate surface. Since the target surface is a cathode and the substrate an anode, the ejected target atoms are accelerated to the substrate surface, where they aggregate and form a thin-film. Thus, thin-film properties are affected by the power applied to the target, electrical state of the substrate, base pressure and working pressure of the chamber, substrate temperature, the distance between the target and the substrate, and so on. Importantly, these parameters can be controlled quite easily, once the basic operation of the technique is understood.

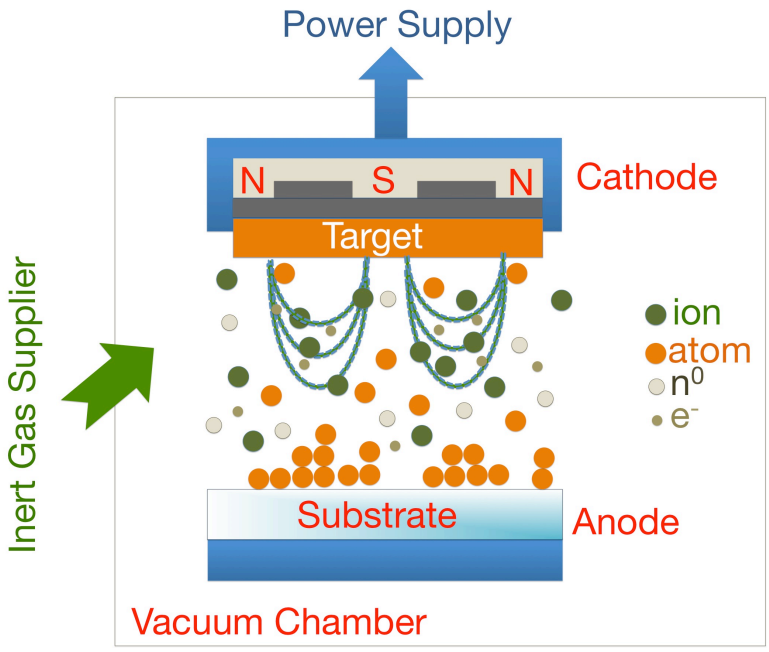

Figure 17 Sketch showing a magnetron sputtering process.

We have chosen magnetron-sputtering technique in order to fabricate anisotropic 3D random network of Si quantum dots via ballistic deposition due to the fact that it provides nonequilibrium conditions, thin-films with good uniformity, and few number of parameters to control. Si-rich SiO_x thin-films were deposited onto p-type, 1-5 Ω·cm, (100)-oriented Si wafers and quartz substrates via Vaksis, NanoD-100 PVD magnetron sputtering system (Fig. 18a and 18b). The substrates were cleaned by first rinsing in ultrasonic baths of acetone and methanol, then using piranha (3:1, H_2SO_4:H_2O_2) and diluted HF (5%) solutions and dried under nitrogen gas. 3"-diameter 99.995%-pure SiO_2 and Si targets were co-sputtered with RF (P_{SiO2} = 180 W) and DC ($10 < P_{Si} < 200$ W) powers applied, respectively. Depositions were performed at room temperature and 99.99% pure Ar was used as the process gas, for which the base pressure was ~$2x10^{-6}$ Torr. The target-substrate distance was kept at 150 mm during deposition. The ambient argon gas pressure was adjusted to 4 mTorr for all depositions. Post-annealing was performed in a high-temperature furnace for 1 h under constant flow of N_2 gas at 1000 °C and 1100 °C temperatures.

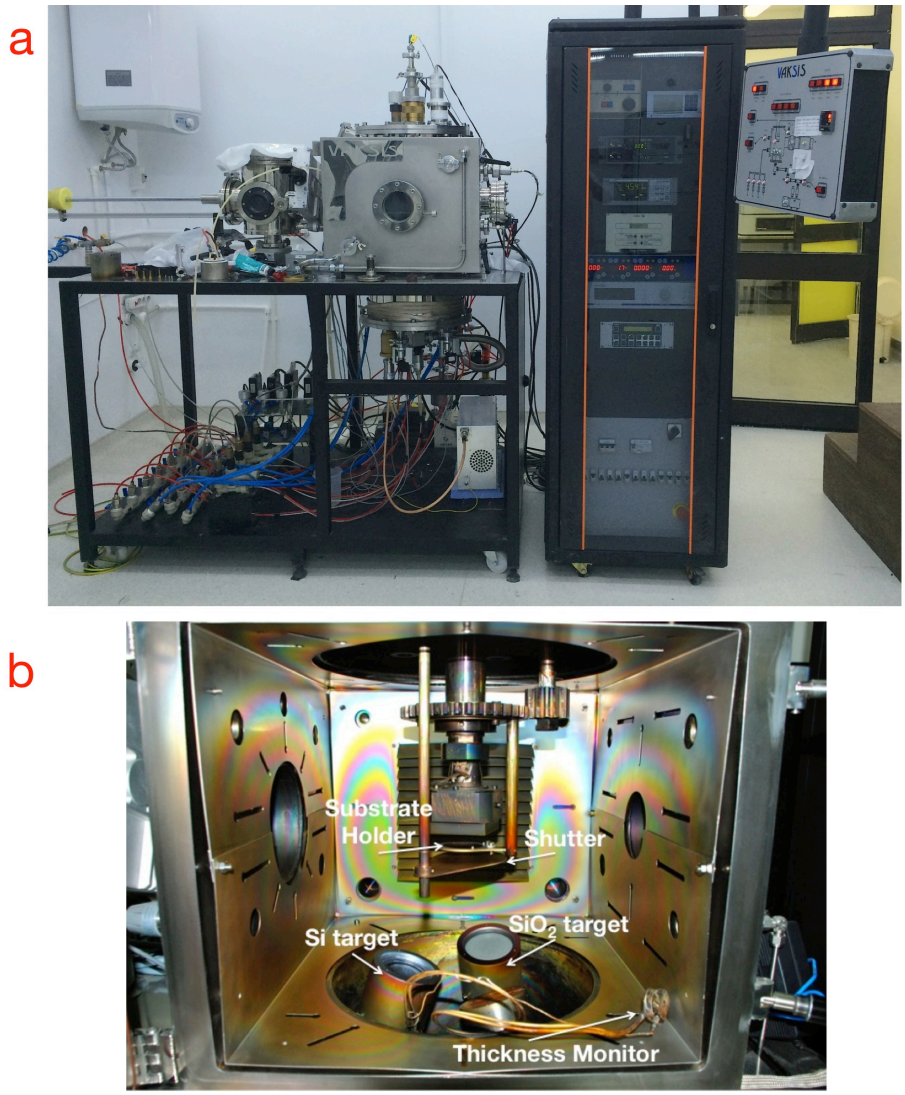

Figure 18 Images showing **(a)** Vaksis, NanoD-100 magnetron sputter system with which the thin-films are deposited. **(b)** Interior design of the sputter chamber.

4.2 Analytical Methods and Tools for Thin Film Characterization

Given the complex, high-order morphology of the anisotropic 3D random network of Si quantum dots, its fabrication from Si-rich SiO_x thin films required fastidious optimization. In order to achieve such an elegant architecture, it is important to first

identify the chemical and structural properties of the thin films, starting from their stoichiometry, homogeneity, crystallinity, chemical, optical and electrical properties and finally, topology. The procedure is described step by step below.

4.2.1 Chemical Characterization

The Si quantum dots are fabricated inside a SiO_x matrix by thermal annealing of magnetron-sputtered thin-films in a wide range of x values ($0 < x < 2$) in order to produce practically all-possible SiO_x species. Stoichiometry, x in SiO_x, were derived from Rutherford backscattering spectroscopy (RBS) elemental analyses and confirmed through X-ray photoelectron spectroscopy (XPS) elemental analyses. RBS analyses were performed using 1.7 MeV He^+ ions accelerated by a Van-de-Graaff generator. After normal incidence backscattered ions were detected at 20° exit angle, where their charge was chosen to be 10 μC for good S/N ratio. SimNMR software (version 6.03) was used to fit and analyze the elemental composition. RBS analyses were performed on the as-deposited thin-films, without any post-annealing procedure. Si wafer was used as the substrate however we have deposited thin layer of carbon before the deposition of thin-film in order to achieve a clear RBS signal. Atomic fractions and areal densities obtained from RBS and XPS measurements were used both in the numerical model and in the molecular dynamics simulations.

XPS analyses were performed using PHI-5000 VersaProbe equipment with monochromatic Al K_α excitation as the X-ray source. XPS depth profile analyses were conducted using 99.99% pure Ar ion bombardments, where the energy of incoming ions was kept at 2 keV. Si and SiO_2 test samples were prepared to ensure that sputtering does not affect the chemical state of Si and that the information obtained from depth profiling reflects the actual Si chemical states within the system. Test samples were also used to determine the elemental peak positions and FWHM of the signals assigned to Si^{0+} and Si^{4+}. Later, we have followed the methodology described by Barbagiovanni *et. al.* [107] XPS spectra were charge-corrected to the main line of the C 1*s* peak set to 284.8 eV and Peakfit software (version 4.12) was

used to fit the spectra by fixing the oxidation states of Si^{n+} (n = 1,2,3,4) to the standard shifts with respect to Si^{0+} using Shirley background, Gaussian-Lorentzian line shapes.

Fourier-transform infrared spectroscopy (FTIR) analyses were performed using Brucker Equinox 55 IR Spectrometer in absorbance mode. The vibrational spectra of the thin films were recorded between 300 and 4000 cm^{-1} at a resolution of 4 cm^{-1} at a 40° angle of incidence. A bare Si wafer was used to determine the background to remove the effect of Si phonon modes that originate from the substrate. Thermally grown and magnetron-sputtered SiO_2 test samples were prepared to ensure the peak position and FWHM of the three characteristic absorption bands arising from the Si−O−Si groups, especially the strongest signal of Si-O-Si anti-symmetric stretching vibrations (~1080 cm^{-1}). Longitudinal (LO) (in the frequency range of 1190–1300 cm^{-1}) and transverse (TO) optical modes of absorption bands (in the frequency range of 1010–1140 cm^{-1}) corresponding to silicon oxide structures with different bridge oxygen bond angles [15,108] were studied with the aim of identifying the structural evolution of the dielectric matrix. A shoulder in the FTIR spectra appearing at lower frequencies was attributed to the presence of SiO_x species. Peakfit software (version 4.12) was used to fit the FTIR spectra using Gaussian-Lorentzian line shapes.

Crystalline structure of the prepared films was verified through Raman spectroscopy (RS). Analyses were performed at room temperature using a Horiba-Jobin Yvon i550 system equipped with a CCD camera. A laser with 532 nm wavelength was used as the excitation source.

4.2.2 Structural Characterization

In order to reveal the morphology in the magnetron-sputtered and post-annealed thin-films, energy-filtered transmission electron microscopy (EFTEM) imaging was performed at the HZDR, Dresden, Germany using an image-corrected FEI Titan 80-300 microscope operating at an accelerating voltage of 300 kV and equipped with a

Gatan Imaging Filter 863. While high-resolution TEM (HRTEM) imaging allows the visualization of Bragg-oriented Si nanocrystals larger than a minimum size, amorphous precipitates as well as non-Bragg-oriented Si nanocrystals cannot be observed with HRTEM, leading to an underestimation of the fraction of the Si phase. For these reasons, EFTEM analysis is a suitable alternative for Si morphology studies. In particular, valence-band plasmon energy-loss imaging is an appropriate approach, since the Si plasmon peak at $E_{loss} \approx 17$ eV is, except the zero-loss peak, the most intense feature in the electron energy-loss spectrum. It has a narrow energy distribution width of a few eV, and thus, allows one to distinguish the Si phase from the SiO_x compound, which was also imaged at $E_{loss} = 27$ eV. Pseudo-coloured images, which are a superposition of a Si plasmon EFTEM image (green) and the corresponding SiO_x plasmon EFTEM image (red) were used for representing the analysis results. Classical cross-sectional TEM specimens were prepared by sawing, grinding, dimpling, and final Ar^+ ion-milling. The same analysis results were obtained for TEM lamellae prepared by *in situ* lift-out using an NVision 40 CrossBeam device (Zeiss). Prior to each TEM analysis, the specimen mounted in a double-tilt analytical holder was placed for 45 s into a Model 1020 Plasma Cleaner (Fischione) to remove organic contamination.

TEM images are 2D images, so its utility in determining the 3D structure is limited. We have further characterized the third dimension of the unique network structure through atom probe tomography (APT). APT is a combination of a field ion microscope and a mass spectrometer, which produces 3D compositional images at the atomic scale with very high analytical sensitivity. The specimen is prepared as a sharp needle to which a very high electric field is applied to controllably extract atoms (ions) from its tip. Ions travel through a time-of-flight mass spectrometer and are recorded by a position-sensitive detector. The extracted ions then projected onto a position-sensitive detector for recording their location. Time-of-flight measurements on the ions provide their isotopic identity as a mass-to-charge ratio of the ion.

The APT analyses in this thesis were conducted using a local electrode atom probe (LEAP) 4000X-HR equipped with laser pulsing capability at the CAMECA Atom Probe Technology Center, Madison, Wisconsin, USA. Sharpened needle-like specimens were prepared using a focused ion beam (FIB) instrument. The specimen was cooled at high vacuum. In this study, a 355-nm-wavelength laser was focused on the specimen to promote field evaporation.

4.2.3 Optical Characterization

Photoluminescence (PL) measurements were taken under Nd:YAG laser excitation (532 nm line) at room temperature. PL setup used to record the PL excitation spectra comprises a Nd:YAG laser, Hamamatsu C7041 detector head, Oriel Instruments MS257 monochromator and a series of lenses and mirrors. The spectra were recorded in the range of 550-1100 nm. Broad PL signal between ~650-1100 nm was observed for $0.6 < x < 1.5$ each centered around 860 nm while the signal intensity differed with x value.

Optical bandgap values were extracted from Tauc plots calculated through transmittance, reflectance, and absorbance spectra taken in the 180-1200 nm wavelength range using a double beam scanning Cary 100 UV-Vis spectrophotometer equipped with a Czerny Turner monochromator.

In order to derive the information on the optical bandgaps of the thin-films, we have first calculated the absorption coefficient using formula below [109]:

$$\alpha = \frac{1}{d} ln \frac{T^Q (1 - R^s)}{T^s} \ , \qquad \text{(Eqn. 6)}$$

where α is the absorption coefficient, T^Q is the transmittance of the quartz substrate, d is the film thickness, T^s is the transmittance of the sample, and R^s is the reflectance

of the sample. Then, we have used Tauc law in order to calculate the optical bandgap values through below equation [110]:

$$\alpha = \frac{B}{\hbar\omega}\left(\hbar\omega - E_g\right)^2 , \qquad \text{(Eqn. 7)}$$

where, α is the absorption coefficient, B is the Tauc coefficient, which is proportional to the oscillator strength of the optical transition through the optical matrix element, $\hbar\omega$ is the photon energy, and E_g is the optical bandgap of the material. Lastly, we have plotted $\sqrt{\alpha\hbar\omega}$ as a function of $\hbar\omega$ and calculated E_g by linear fitting of the spectra.

Spectroscopic ellipsometry (SE) analyses were conducted using SEMILAB SOPRA GES5E equipped with Sopra Winelli II software and derived the information on the optical constants of the thin-film as described below step-by-step:

- First, thin-films were measured using SE equipment,
- Second, an optical model was developed to describe the thin-films,
- Third, experimental data were simulated using the optical model until achieving a good fit, and
- Last, optical information was extracted from mathematical modelling.

Ellipsometric angles Ψ, describing the amplitude ratio, and Δ, describing the phase difference between polarizations parallel (p) and perpendicular (s) to the plane of incidence, are calculated using Fresnel reflection coefficients (R_p and R_s) as follows [111].

$$\rho = tan(\psi)e^{i\Delta} = \frac{R_p}{R_s} , \qquad \text{(Eqn. 8)}$$

where ρ is the polarization state.

Optical constants were derived through following equations [111]:

$$N = n + ik \ , \qquad \text{(Eqn. 9)}$$

where N, n, and k are the complex refractive index, refractive index, and extinction coefficient, respectively. The relationship between the complex refractive index and the dielectric constants (ε) could be derived from Maxwell equations:

$$\varepsilon = N^2 \text{ where } \varepsilon = \varepsilon_r + i\varepsilon_i \qquad \text{(Eqn. 10,11)}$$

$$\varepsilon_r + i\varepsilon_i = (n + ik)^2, \qquad \text{(Eqn. 12)}$$

where the imaginary part is: $\varepsilon_i = 2nk$ and real part is: $\varepsilon_r = n^2 - k^2$.

Ellipsometric angles, Ψ and Δ, were measured over the spectral range of 240-840 nm at 70° angle of incidence at room temperature with a xenon lamp as source. A generic optical model is developed to describe the thin-film content (please refer to the Section 5.3 for details). Si suboxide volumetric fractions were extracted from XPS analyses. SE data is interpreted through Tauc-Lorentz (TL) and Bruggeman effective medium approximation (BEMA) models. TL is used to describe the optical functions for a-Si and insulator matrix, whereas a combination of TL and BEMA is used to describe the optical functions.

4.2.4 Electrical Characterization

Conductivity analyses were first carried through both lateral (Fig. 19a) and vertical (Fig. 19b) *I-V* measurements. p-type, 0.01-0.05 Ω·cm, (100) oriented Si wafers were used for vertical *I-V* measurements whereas quartz substrates were used for lateral *I-V* measurements (Fig. 19a). For vertical *I-V* analyses the current flow was measured between thermally evaporated aluminium point contacts (~1 μm thick) on film surface and Al contact evaporated onto the back surface of the Si wafer (Fig. 19b). For lateral *I-V* analyses ~1 μm-thick coplanar Al contacts were thermally evaporated

with 1.5 cm spacing onto film surface on a quartz substrate. Current flow between the thin-film and the Si substrate for vertical *I-V* analyses and current flow between the coplanar electrodes for lateral *I-V* analyses were measured via a Keitley 2440 ammeter and a Hewlett - Packard 4140B picoammeter, respectively. Newport Oriel Sol3A Class AAA solar simulator at 0.9 A.M. was used for the light-illuminated *I-V* measurements. Furthermore, we have sputtered an aluminum zinc oxide (AZO) layer between the thin-film and Ag point contacts in order to gather current flow from the entire film surface (Fig. 19c).

Conductivities were extracted from *I-V* measurements where vertical current flow was measured at 10 different points on the film surface and their average was taken. We have used Ohm's law to calculate conductivity using following equations:

$$I = \frac{V}{R} \ , \qquad \text{(Eqn. 13)}$$

where, I, V, and R are current (A), voltage (V), and resistance (Ω), respectively.

$$R = \rho \frac{l}{A} \text{ and } \sigma = \frac{1}{\rho} \ , \qquad \text{(Eqn. 14,15)}$$

where, ρ, l, and A are resistivity (Ω·m), the length of the conductor (m), and the cross-sectional area (m^2), respectively. σ is the conductivity (S/m).

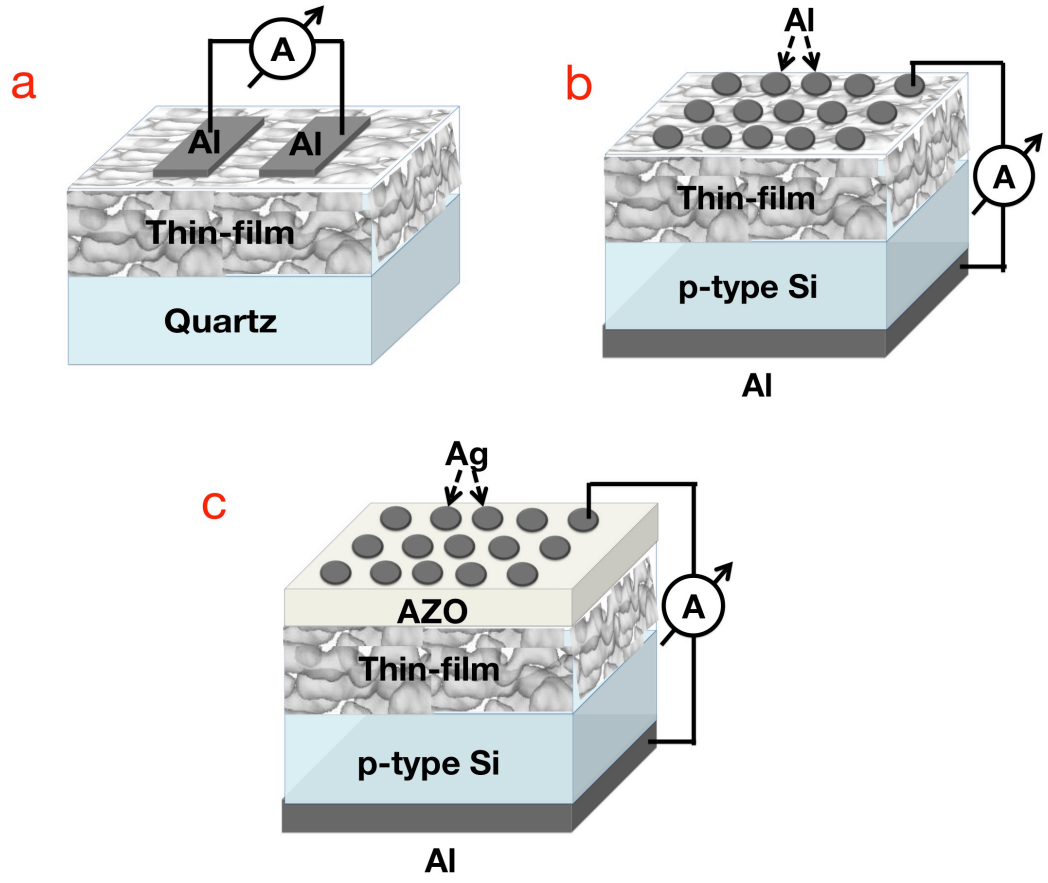

Figure 19 Sketches showing various configurations used for *I-V* measurements: **(a)** Quartz/thin-film/Al**, (b)** Al/p-Si/thin-film/Al, and **(c)** Al/p-Si/thin-film/AZO/Ag.

4.3 Theoretical Studies

4.3.1 Numerical Model of the Ballistic Deposition

Monte-Carlo simulations were used to analyze the random network formed by the ballistic deposition process and guide the experiments in an iterative manner, with the numerical model being fine-tuned based on experimental results. In collaboration with Dr. F. Ömer İlday, we developed a simple model based on layer-by-layer and stochastic allocation of Si and SiO_2 atoms to sites in a 3D grid. The probability of

any site being occupied by a Si atom, p_0, depends on the overall deposition rate of Si. Given the cold substrate, the mobility of a Si atom is heavily reduced. Thus, when considering the affinity of Si atoms to seek out and stick to each other, we considered only the nearest-neighbors, which were described by two probabilities, p_1 (for the site directly below) and p_2 (for the immediate neighbouring sites), respectively. The relative strength of p_1 over p_2 determines the tendency towards vertical growth (anisotropic growth) over branching off laterally (isotropic growth). The value of p_0 was fixed by experiment as it directly determines the Si concentration value of x. The values of $p_1 = 10$ and $p_2 = 100$ were chosen to reproduce the 3D morphology of the structure as observed from the TEM images as closely as possible. Although the values of p_1 and p_2 cannot be fixed precisely by experiment, we found out that the critical x value to achieve percolation in the vertical or horizontal direction does not change appreciably by the specific values of p_1 and p_2, as long as they are chosen to resemble the experimentally observed structure. The algorithm can be summarized as follows. When the simulation code is run, each site is calculated to be either a Si site, flagged with a value of 1 or a non-Si site, flagged with a value of 0, layer by layer until the full thin film is built up. After the simulation of the deposition process is finished, we calculate which Si sites are connected through each other to conducting layers at the top and bottom of the grid, representing electrodes sandwiching the thin film. We use a recursive algorithm to determine the connections, starting from each site at the top and the bottom layers. For each site, the code takes steps in all six directions, unless the stepped into site is outside of the boundaries of the grid. If a stepped-into site is a Si site, it is flagged with a value of 2 and further steps are taken in all 6 directions starting from that site. If the site is a non-Si site, then its flag is left unchanged and no other steps are taken from that site. When the simulation code exhausts sites from which to take further steps, the final state is a grid with each site flagged as 0, 1 or 2, representing a non-Si site, a disconnected Si site and an electrically connected Si site. The ratio of number of total flag 1 and flag 2 sites to flag 0 sites corresponds to $x/(1+x)$. Next, we calculate the ratio of number of flag 2 sites to flag 1 sites, corresponding to the ratio of connected Si sites to disconnected

Si sites. Since the photoelectrons generated at disconnected sites are thermalized and do not contribute to current formation, except for the possibility of tunneling, for which the probability is low enough that it can safely be ignored, high-efficiency device operation necessitates the connected sites to dominate over disconnected sites by a ratio of ~5 or more. The simulation is very strongly recursive, and the number of sites to visit scales with order of 6^n, where n is the total number of sites in the grid. The simulations for each case were repeated numerous times, using a random number generator with uniform distribution, for each value of x, checking for numerical convergence to an average value. The connectedness ratio was found to be independent of the grid size (beyond a minimum size of approximately 100x100x100) and vary little from run to run, rendering the results robust. The simplicity of our model allowed straightforward interpretation, serving as guide to the experiments. Agreement with experiments was quite good, which is to be expected given the universality of such growth models, rendering results largely independent of many details.

4.3.2 Molecular Dynamics Simulations

Molecular dynamics simulations were conducted in collaboration with Dr. Hande Üstünel Toffoli and Dr. Daniele Toffoli, on homogeneous Si:SiO_x systems for $0.5 < x < 1.5$ at the experimental annealing temperature. The atomic scale of this approach allows for a local map of Si-O bonding and determination of individual Si partial charges for various x values and all histograms were drawn as a percentage of the total number of Si atoms in the system. Si-Si, O-O, and Si-O atomic interactions were modeled using the charge-optimized many-body (COMB) potential [112,113] and the open-source molecular program suite LAMMPS was used for the calculations [114]. The simulation runs were conducted in a 2.6 nm x 2.6 nm x 2.6 nm cubic simulation cell with periodic boundary conditions. A total of 1000 Si and O atoms were initially regularly positioned on a cubic grid, with a predetermined O:Si ratio of x (x = 0.5, 0.7, 1.0, 1.2 and 1.5). The distribution of Si and O atoms on the grid were chosen at random from a uniform probability distribution. A time-step of

0.5 fs was chosen for the integration of equations of motion. An initial 20000-step long equilibration stage conducted in the NVE ensemble was followed by a 200000-step long simulation using the Langevin thermostat at a nominal temperature of 1100 °C. Charges of each Si and O atoms were treated as a dynamical variable in the COMB potential and updated at every step of the simulation. The Si-Si, O-O and Si-O interaction thus include both covalent effects and charge transfer. The Coulombic charge assigned to each of the atoms in the simulation was recalculated at every integration step.

CHAPTER 5

INVESTIGATION OF SILICON-RICH SILICON OXIDE THIN-FILMS: TOWARDS OPTIMIZATION FOR A MULTI-FUNCTIONAL MATERIAL DESIGN

"I don't know anything, but I do know that
everything is interesting if you go into it deeply enough."
- Richard P. Feynman,
Omni interview: The Smartest Man in the World, 1979

Among silicon nanocrystal fabrication methods, nucleation from Si-rich SiO_x thin-films is one of the most popular. This is largely because the dielectric SiO_x matrix creates a potential barrier for the charge carriers to be confined inside Si nanocrystals, turning them into quantum dots. Moreover, the matrix helps eliminate the dangling bonds by forming Si-O bonds. Apart from the Si nanocrystals themselves, the chemical structure of the dielectric matrix they are embedded in and the interface between the matrix and the nanocrystals have dramatic impact on the light emission properties of the Si-rich SiO_x systems [15,107,108,112,113]. This opens up a lot of possibilities in nanomaterial engineering; yet fulfillment of these possibilities requires a solid grasp of the local chemical bonding dynamics and the experimental capabilities to tailor them. A straightforward and highly effective way to understand the chemical structure of the matrix is to fine tune the stoichiometry of Si-rich SiO_x thin-films and to characterize the outcome thoroughly. Attempts to control the dynamics of these systems by tuning stoichiometry are well known [15,16,52,80,84,85], but it was not clear *a priori* whether quantum confinement could be preserved, as required for a tunable bandgap, while simultaneously forming a percolated random network that can efficiently transport the charge carriers. Thus,

a systematic study was conducted. In this chapter, we will guide the reader through this process and describe how we searched for signs of substantial changes in the properties of the system and how we intervened with the dynamics towards fabrication of the anisotropic 3D random network of Si quantum dots. For the sake of simplicity, we have sectioned this chapter into four sub-sections to guide the reader through detailed chemical, structural, optical, and electrical investigations of Si-rich SiO_x thin-films, in that order.

5.1 Chemical Investigations

The stoichiometry, homogeneity, chemical bonding dynamics, and crystallinity of the Si-rich SiO_x thin-films have been investigated through RBS, XPS, FTIR, and RS analyses. As mentioned earlier in Section 4.1, during magnetron deposition, we have applied a constant RF voltage to SiO_2 target and various DC voltage levels (2 W/in^2 < P_{Si} < 22 W/in^2) to the Si target in order to alter the amount of excess Si in thin-film content. This way we have been able to analyze the stoichiometry (x = O/Si ratio) in order to pinpoint the values for which the thin-film's chemical, structural, optical, and electrical properties were substantially changed.

The most influential parameters is x, which needs to be determined as precisely as possible. First, we have calculated the x values from RBS analyses and independently verified them through XPS analyses. Table 1 shows the data on thicknesses, elemental compositions, and areal densities of the atoms calculated from RBS analyses of the thin-films with various excess Si content. The x values are simply calculated by dividing the atomic percentages of O to Si for each thin-film with various Si content.

Table 1 Table showing the thickness, elemental concentrations, and areal densities of the as-deposited thin-films with various excess Si concentrations.

P_{Si} (W)	Thickness (d/nm for 2.2g/cm³)	Concentration (at.%)			Areal Density (10^{15} atomic entities/cm²)
		Si	O	Ar	
18	276	36,5	63	0,5	1780
36	286	43,5	56	0,5	1770
45	314	40,5	59	0,05	2000
54	312	43,5	56	0,05	1950
63	262	45,5	54	0,05	1620
72	267	52	47,5	0,5	1580
81	300	48	51,5	0,05	1830
90	281	48,5	51	0,05	1710
99	282	51	48,5	0,05	1690
144	283	58	41,5	0,5	1620
171	278	63,5	36	0,5	1550
180	260	64,5	35	0,5	1440
189	284	65	34,5	0,5	1570
198	267	66	33,5	0,5	1470

We have also determined atomic concentrations of Si and O through XPS depth-profiling analyses. An example can be seen in Fig. 20, where the point 0 in the x-axis represents the surface. After first 2 min. the surface oxide is etched down. Between the 2nd and 10th min. of the depth profiling, the thin-film was etched away. After 10 min. of etching it appears that the etching continued on with the Si wafer evidenced from the lack of O and increased atomic percentage of Si.

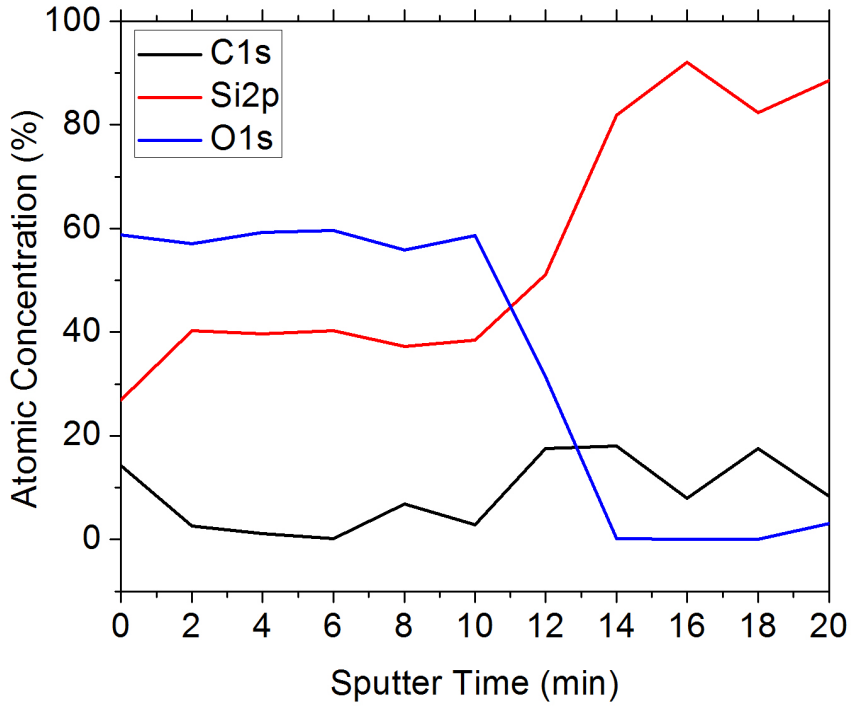

Figure 20 Graph showing atomic percentages of Si, O, and C atoms as a function of sputtering time during XPS depth profiling.

Next, let us consider *x* values obtained both from RBS and from XPS analyses as a function of DC power applied to the Si target (Fig. 21). As seen from the figure that the stoichiometry "*x*" is well determined and the *x* values, which are calculated from XPS and RBS analyses, are highly correlated.

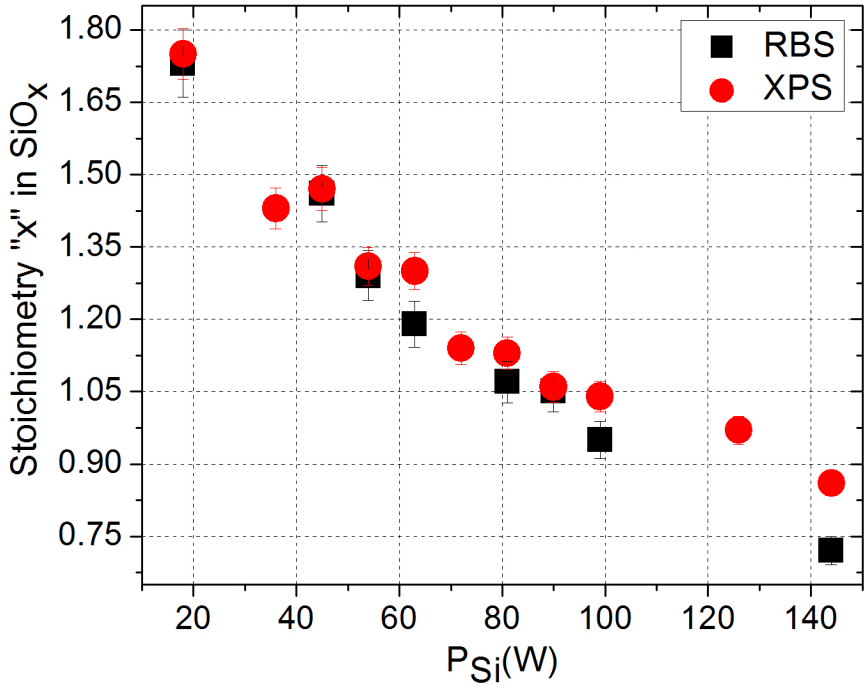

Figure 21 Graph showing *x* values calculated from XPS and RBS analyses of the thin-films as function of the DC power applied to the Si target during magnetron sputter deposition.

Second, we have verified the homogeneity of the thin films. Figure 22 shows the XPS depth-profiling analyses performed on Si 2*p* signal of the Si-rich SiO_x thin-film with x = 1.07. As can be seen from the figure, the first layer is the surface oxide layer, which is rich in Si-O bonds. The preceding four layers belongs to the thin-film, where the numbers of Si-Si and Si-O bonds are almost equal, which is not surprising since the stoichiometry of the film is almost equal to 1. Thin-film layer is followed by six layers of the substrate (Si wafer), as evidenced from the lack of signal originating from the Si-O bonds located at 103.4 eV [15,107] and the presence of an intense signal originating from the Si-Si bonds located at 98.2 eV [15,107]. Figure 22 also shows that the Si-Si and Si-O bonds are homogenously distributed throughout the thin-film. Note that we only present homogeneity of the film with x = 1.07 here

for brevity, but we have performed depth profiling to every thin film sample with various stoichiometries, where we have confirmed the homogeneity for all of them.

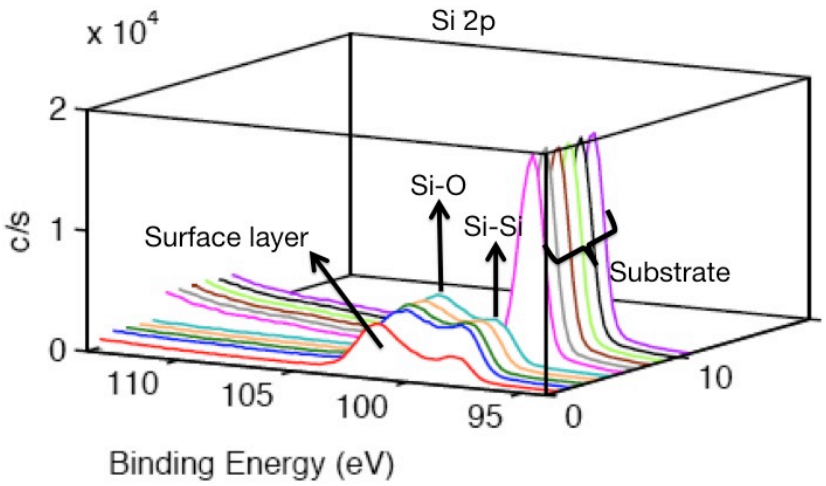

Figure 22 Graph showing the XPS depth-profiling analyses performed on Si 2*p* signal of the 1100 °C post-annealed thin-film with $x = 1.07$ [121].

Third, we have performed XPS peak fitting analyses in order to identify the Si oxidation states (refer to Section 4.2.1 for details). An example is given in Fig. 23, which is showing that the XPS spectrum is dissected into five signals originating from Si^{+0} (light blue), Si^{+1} (green), Si^{+2} (pink), Si^{+3} (brown), and Si^{+4} (dark blue) that belong to Si, Si_2O, SiO, Si_3O_2, and SiO_2, respectively. The envelope signal of these five signals (red) perfectly matches with the experimentally obtained spectrum (black). In order to fit the spectra, we have locked the oxidation states of Si^{n+} (n = 1,2,3,4) to the standard shifts with respect to Si^{0+} using Shirley background, Gaussian-Lorentzian line shapes [15,107].

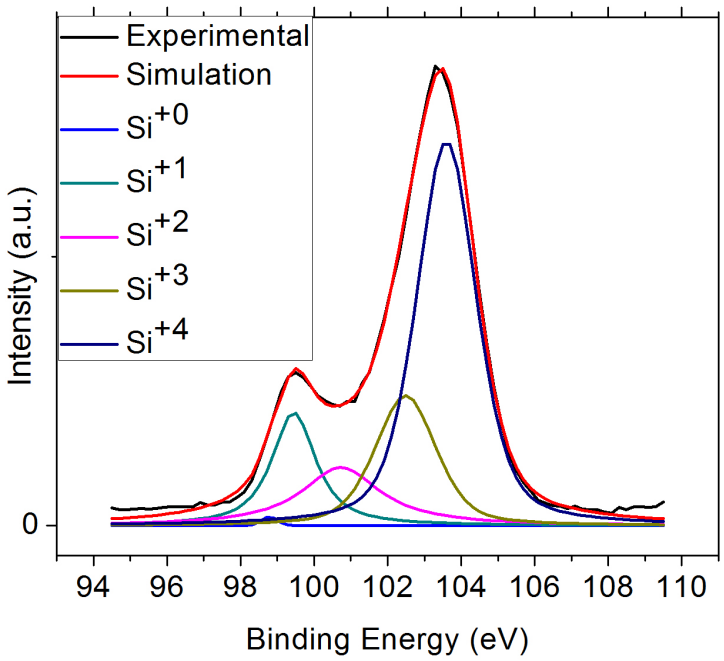

Figure 23 Graph showing an example of the XPS peak fitting analyses. The spectrum is dissected into five signals originating from Si^{+0}, Si^{+1}, Si^{+2}, Si^{+3}, and Si^{+4} that belongs to Si, Si_2O, SiO, Si_3O_2, and SiO_2, respectively. The envelope signal of these five signals is colored red and the spectrum obtained experimentally is colored black.

Later, we have calculated the integrated peak areas of the signals originating from Si^{+n} and plotted them with respect to the x values in order to understand the chemical composition of the thin-films (Fig. 24). It is seen from Fig. 24 that there seems to be three regions with similar features:

- When $x < 0.9$, the structure is dominated by stoichiometric Si, and there is little stoichiometric SiO_2.
- When $0.9 < x < 1.4$, the structure is composed mostly of substoichiometric Si_2O, SiO, and Si_2O_3. In fact, this is the only region where all Si^{+n} and, strickingly, SiO are present.
- When $x > 1.4$, the structure is dominated by stoichiometric SiO_2.

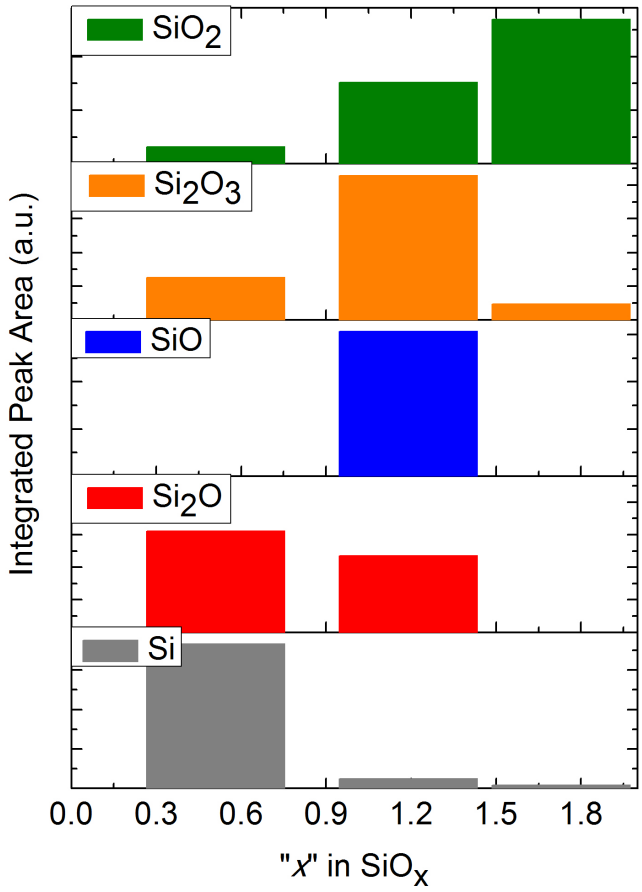

Figure 24 Graph showing relative contributions of XPS signals emanating from substoichiometric (Si_2O, SiO, and Si_2O_3) and stoichiometric (Si and SiO_2) components to the Si 2*p* XPS spectra of the 1100 °C post-annealed thin-films [121].

In other words, we can say that the three representative regions are:

- Si-rich region for $x < 0.9$,
- Intermediate region for $0.9 < x < 1.4$, and
- SiO_2-rich region for $x > 1.4$

This is also observed in Fig. 25, where the depth-profiling analyses are shown for various *x* values that are representative to the three regions described above.

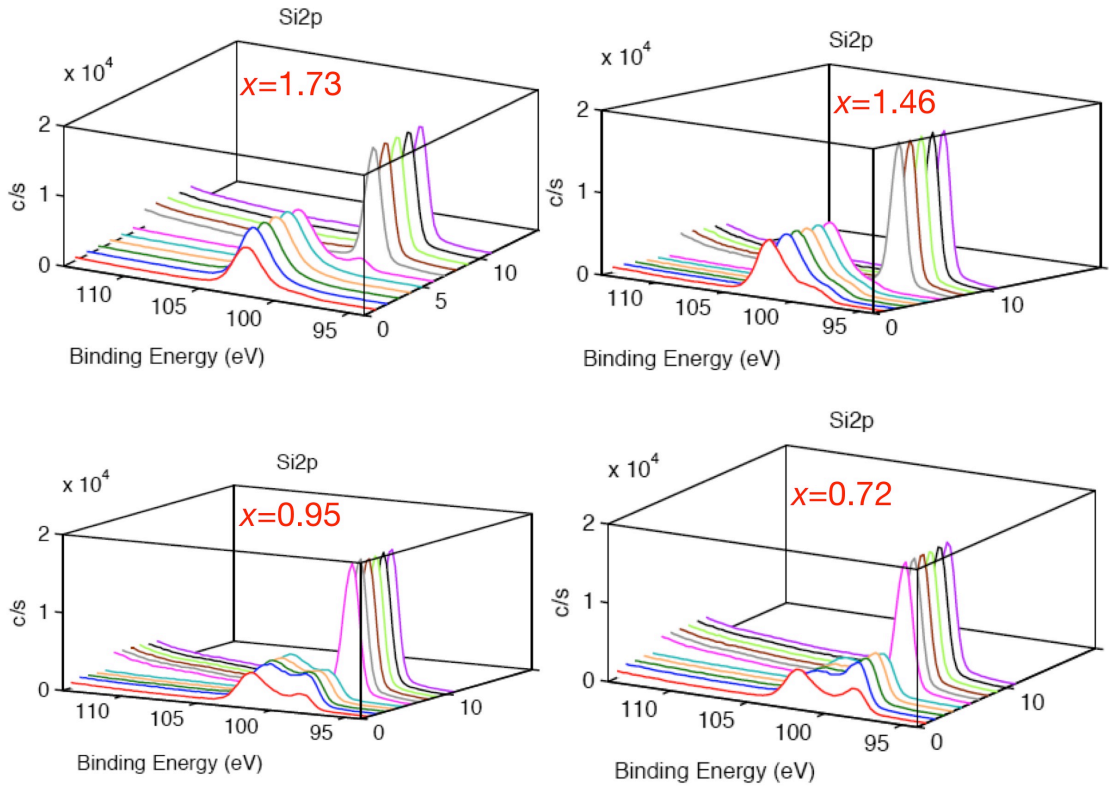

Figure 25 Graph showing the XPS depth-profiling analyses performed on Si 2*p* signal of the 1100 °C post-annealed thin-films for x = 1.73, x = 1.46, x = 0.95, and x = 0.72.

Figure 25 shows that Si-Si bonds dominate the Si-rich region for x = 0.72, whereas the number of Si-Si and Si-O bonds is almost equal in the intermediate region of x = 0.95. On the other hand, the SiO_2-rich region for x = 1.46 and x = 1.73 are dominated by the Si-O bonds, specifically those originating from the stoichiometric SiO_2 that are positioned at 103.4 eV. As can be seen from the spectrum for x = 1.73, when the stoichiometry approaches to x = 2, the signal originating from the substoichiometric Si-O bonds are further diminished, whereas the signal originating from the stoichiometric SiO_2 is enhanced.

The reader should bear in mind that the XPS analyses presented so far have been performed on post-annealed samples, which were annealed at 1100 °C for 1 h under constantly flowing N_2 atmosphere. This means that the unstable suboxides have indeed been stabilized in the intermediate region for $0.9 < x < 1.4$. This is a very interesting and fortunate outcome since one would expect that when a substantial amount of external energy is added to the system via post-annealing, the unstable suboxides should be phase separated to stable forms of Si or SiO_2 through a disproportionation reaction (Eqn. 2). This expectation is realized and the system nearly fully phase separated when $x < 0.9$ and $x > 1.4$. However, we find that for $0.9 < x < 1.4$, the full phase separation is prevented.

In order to illuminate this point, we have performed XPS depth-profiling analyses on as deposited and 1000 °C post-annealed samples as well. Figure 26 shows XPS depth-profiling analyses performed on Si 2*p* signal of the thin-films for three representative regions: Si-rich region ($x = 0.72$); intermediate region ($x = 1.07$, $x = 1.19$, $x = 1.29$); SiO_2-rich region ($x = 1.46$ and $x = 1.73$) for as-deposited (Fig. 26a), and for 1000 °C (Fig. 26b) and 1100 °C (Fig. 26c) post-annealed samples, where spectrum with different colors refer to the layer numbers that were etched during depth-profiling, where "layer 1" is the surface layer, "layers 2 to 6" are thin-film layers, "layer 7" is the interface layer between the thin-film and the substrate, and "layers 8 to 11" are substrate layers. The substrate is a Si wafer. As can be seen from Fig. 26, for Si-rich region ($x = 0.72$) the thin-film layers (layer 2) are mostly composed of nominally unstable suboxides evidenced from the broad signal located between 98 eV and 104 eV, where the signal for stable Si is located at 98.2 eV, which is seen from the substrate layers of 8-11. Also, surface layers (layer 1) are, as expected, mostly composed of stable SiO_2, evidenced from the signal located at 103.4 eV. The suboxides are distributed between these two signal positions with standard shifts with respect to signal originating from stable Si in following order: Si^{+1}, Si^{+2}, and Si^{+3}.

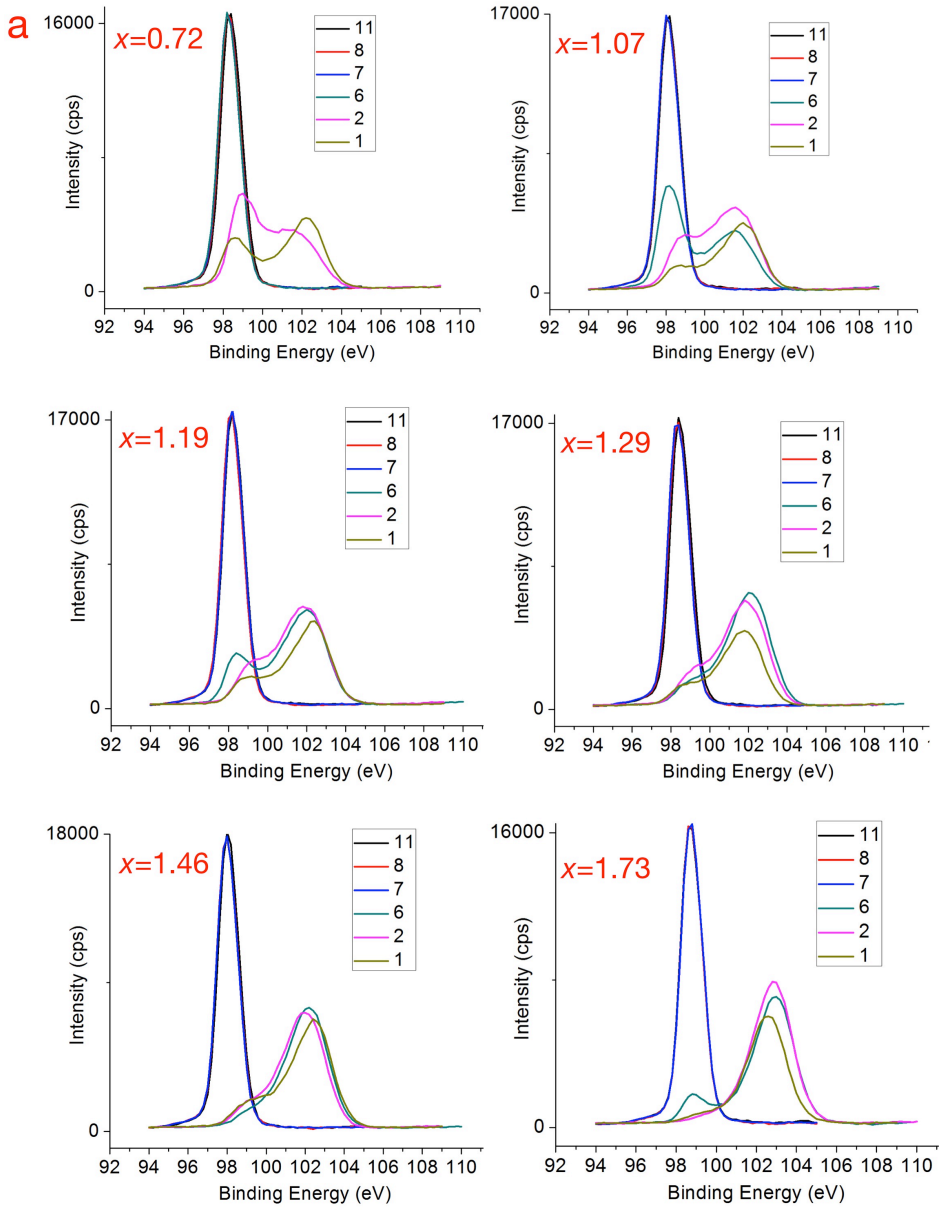

Figure 26 Graph showing the XPS depth-profiling analyses performed on Si 2*p* signal of the silicon-rich silicon oxide thin-films for three representative regions: Si-rich region (x = 0.72); intermediate region (x = 1.07, x = 1.19, x = 1.29); SiO_2-rich region (x = 1.46 and x = 1.73) for **(a)** as-deposited, and for **(b)** 1000 °C, and **(c)** 1100 °C post-annealed samples, where spectrum with different colors represents the information obtained from different layers during depth-profiling.

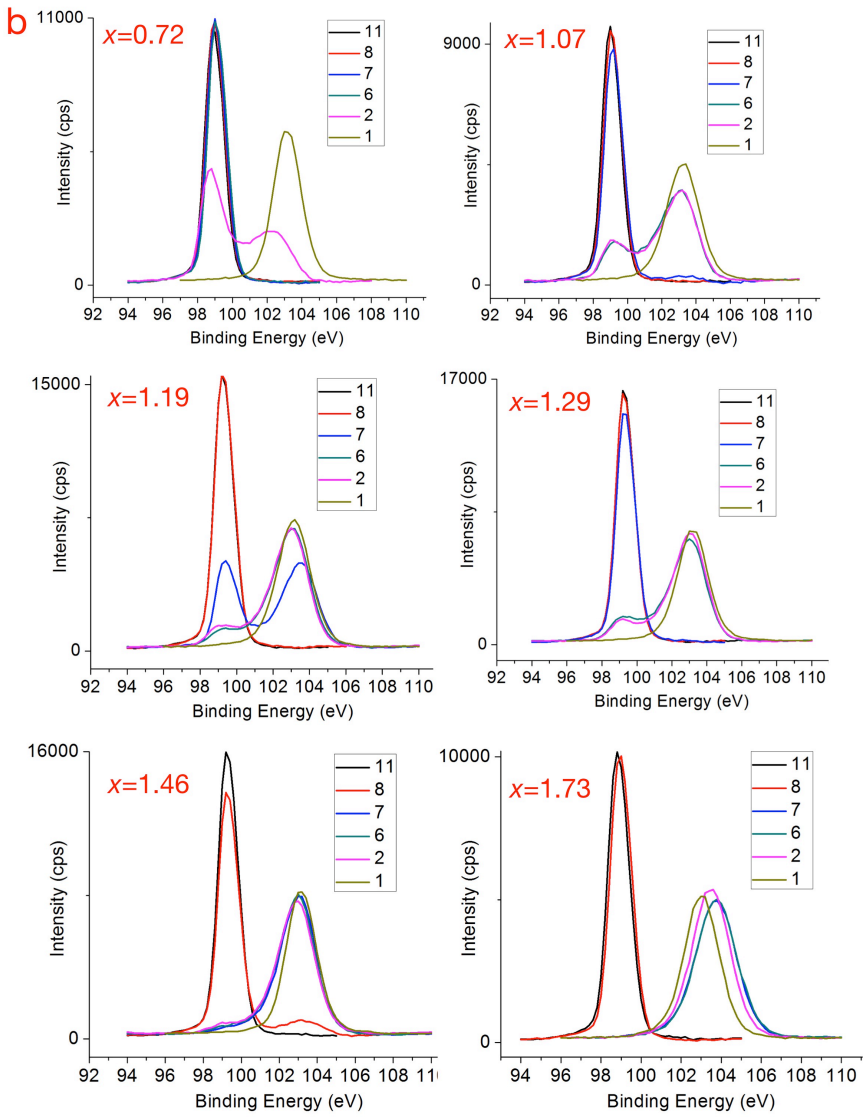

Figure 26 (Continued)

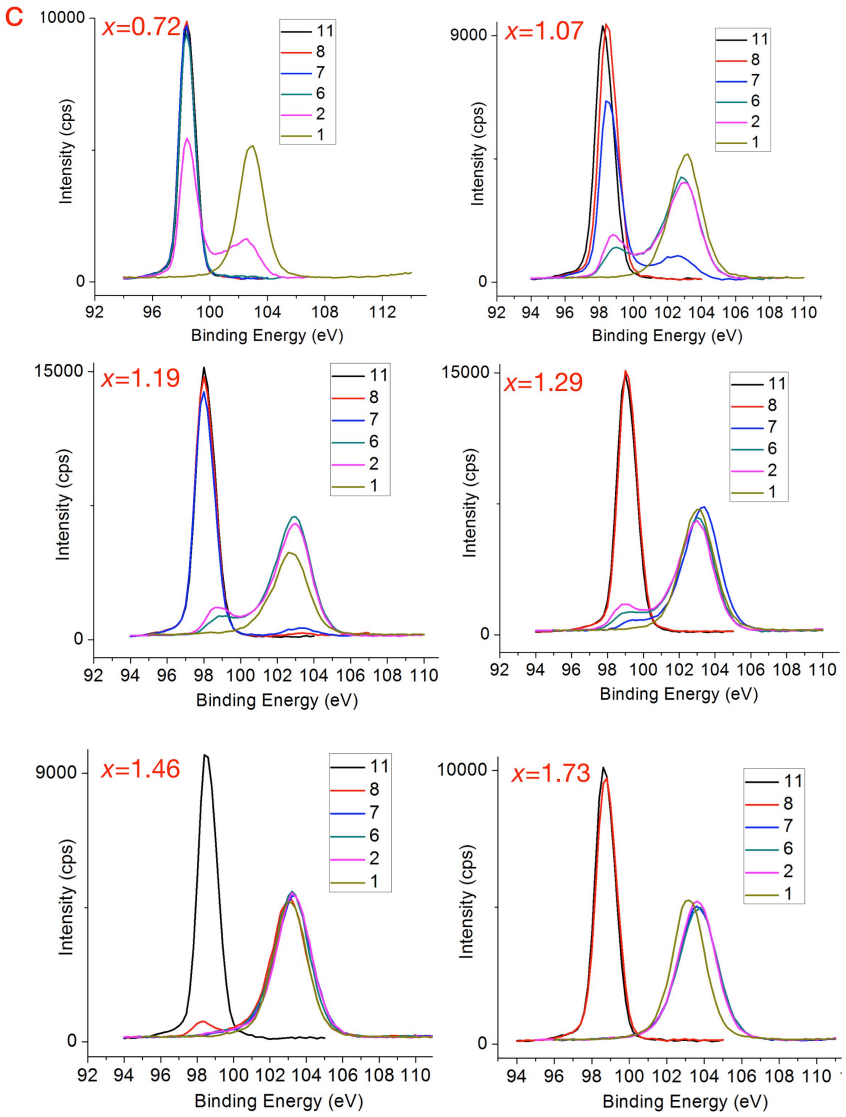

Figure 26 (Continued)

At first glance, it is seen that the chemical bonding dynamics significantly varies between the as-deposited and post-annealed samples. As it is seen from Fig. 26a, for the as-deposited thin-films, the suboxide content varies from region to region: In Si-rich region (x = 0.72), the intensity of the signal shifts towards Si, on the other extreme; it shifts towards SiO_2 for SiO_2-rich region (x = 1.46 and x = 1.73). Upon

post-annealing of the thin-films, we observe a clear phase separation of the nominally unstable suboxides into stable Si and SiO_2, evidenced by results shown in Fig. 26b and 26c. Moreover, we observe that the phase separation continues when the annealing temperature is increased from 1000 °C (Fig. 26b) to 1100 °C (Fig. 26c). It is seen from the figures that the SiO_2-rich region is almost completely phase separated, the intermediate region is still largely composed of suboxides and the Si-rich region is mostly composed of Si. These results independently confirm the results shown in Fig. 24, where the nominally unstable suboxides are seem to have been stabilized for the intermediate region.

The importance of creating and stabilizing of the nominally unstable suboxides towards self-assembly of the anisotropic 3D random network of Si quantum dots is explained in detail earlier in Chapters 1 to 3, specifically in Section 2.2. The information obtained from XPS analyses points out that the intermediate region might have the desired multi-scale complex structure. For this reason, we will keep an eye on this region and try to extract the differences possibly introduced by this unique network throughout the thin-film characterization procedure.

FTIR is a great tool to characterize chemical bonding dynamics of silicon oxides. The FTIR signal originating from stoichiometric Si-O-Si anti-symmetric stretching vibrations is located at ~1080 cm^{-1} and the FTIR signal originating from the substoichiometric SiO_x species appears as a shoulder at lower frequencies [15,108]. We have performed FTIR analyses on 1100 °C post-annealed thin-films to verify the XPS results, namely that there are three representative regions and that the suboxides have been stabilized for the intermediate region. Figure 27 shows FTIR spectra that are background corrected, normalized, and y-shifted after normalization for as-deposited and for 1000 °C and 1100 °C post-annealed samples.

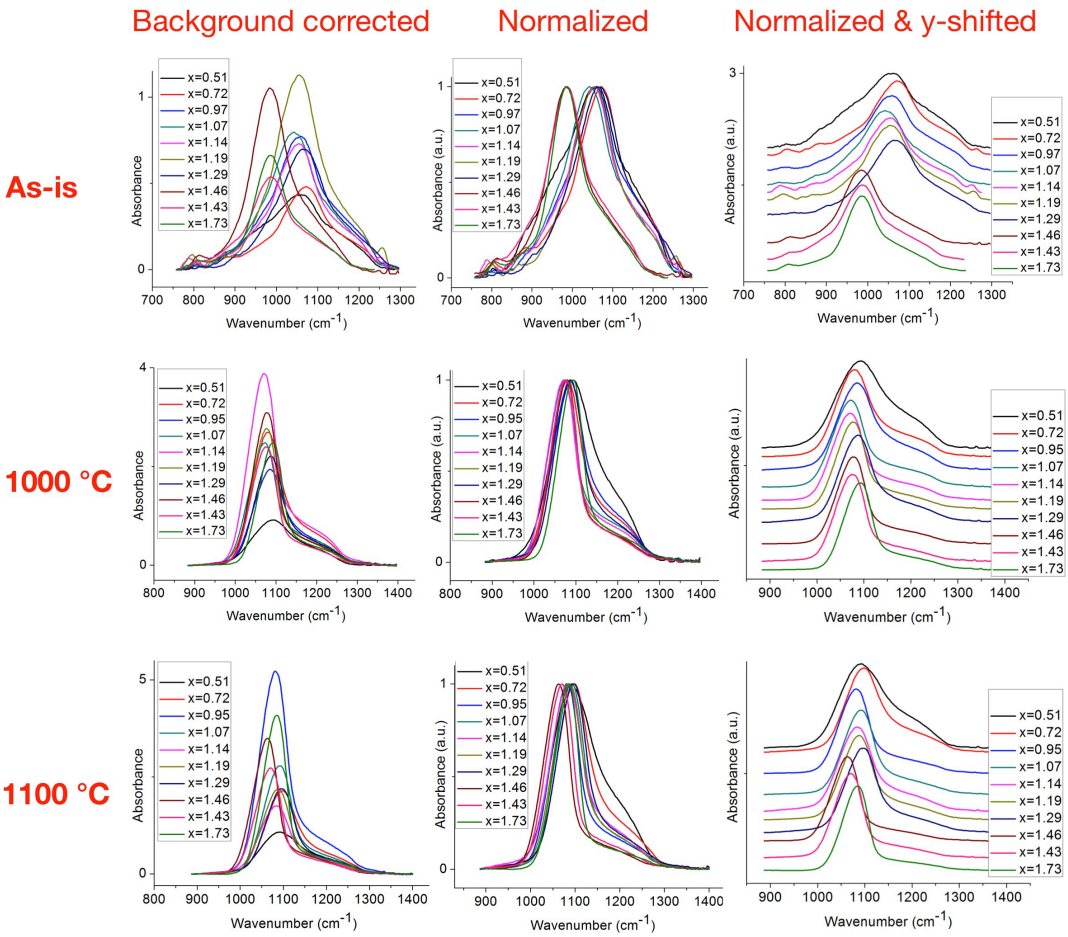

Figure 27 Graphs showing FTIR spectra that are background corrected, normalized, and y-shifted after normalization for as-deposited and for 1000 °C and 1100 °C post-annealed thin-films.

As can be seen from the figure, FTIR spectra of the as-deposited thin-films are broader compared to those of the post-annealed thin-films. As can be seen through the normalized spectra, the full-width at half maximum (FWHM) of the signal originating from Si-O-Si anti-symmetric stretching vibrations decreases when thin films are annealed at high temperatures and it further decreases when the annealing temperature is increased to 1100 °C. Furthermore, evidenced from the evolution of the shoulder seen in high frequencies, annealing procedure clearly affects the

longitudinal (LO) (in the frequency range of 1190–1300 cm^{-1}) and transverse (TO) optical modes of absorption bands (in the frequency range of 1010–1140 cm^{-1}) corresponding to silicon oxide structures with different bridge oxygen bond angles [15,108]. More importantly, a very interesting phenomenon is revealed when the normalized spectra are shifted along the y-axis for thin-films with various stoichiometries: The spectrum appears to behave similar for a group of x values:

- First group: $x = 1.73$, $x = 1.46$, and $x = 1.43$,
- Second group: $x = 1.29$, $x = 1.19$, $x = 1.14$, and $x = 1.07$,
- Third group: $x = 0.97$, $x = 0.72$, and $x = 0.51$, verifying the finding of XPS analyses.

The range of x values for these three groups matches to the three representative regions revealed in XPS analyses:

- Si-rich region for $x < 0.9$,
- Intermediate region for $0.9 < x < 1.4$, and
- SiO_2-rich region for $x > 1.4$

It is fascinating to see that these three regions are not only seen for the post-annealed samples, but also appear for the as-deposited samples. This suggests that the thin-film deposition procedure significantly influences the chemical bonding dynamics, as to be expected from ballistic deposition.

Next, we performed peak-fitting analyses on FTIR spectrums of the thin-films with various x values (please refer to Section 4.2.1 for details). An example is given in Fig. 28. Figure 28a shows that the FTIR spectrum is dissected into five signals originating from Si-O-Si anti-symmetric stretching vibrations, denoted by TO_2, (green), SiO_x (light blue), TO_3 (pink), LO_1 (brown), and LO_2 (dark blue). The envelope signal of these five signals (red) perfectly matches with the experimentally obtained spectrum (black). Figure 28b shows the peak positions of these signals originating from TO and LO modes of silicon oxide FTIR spectrum along with peak

position of the SiO_x signal for various x values. Figure 28c shows the integrated peak areas of these signals with respect to x values.

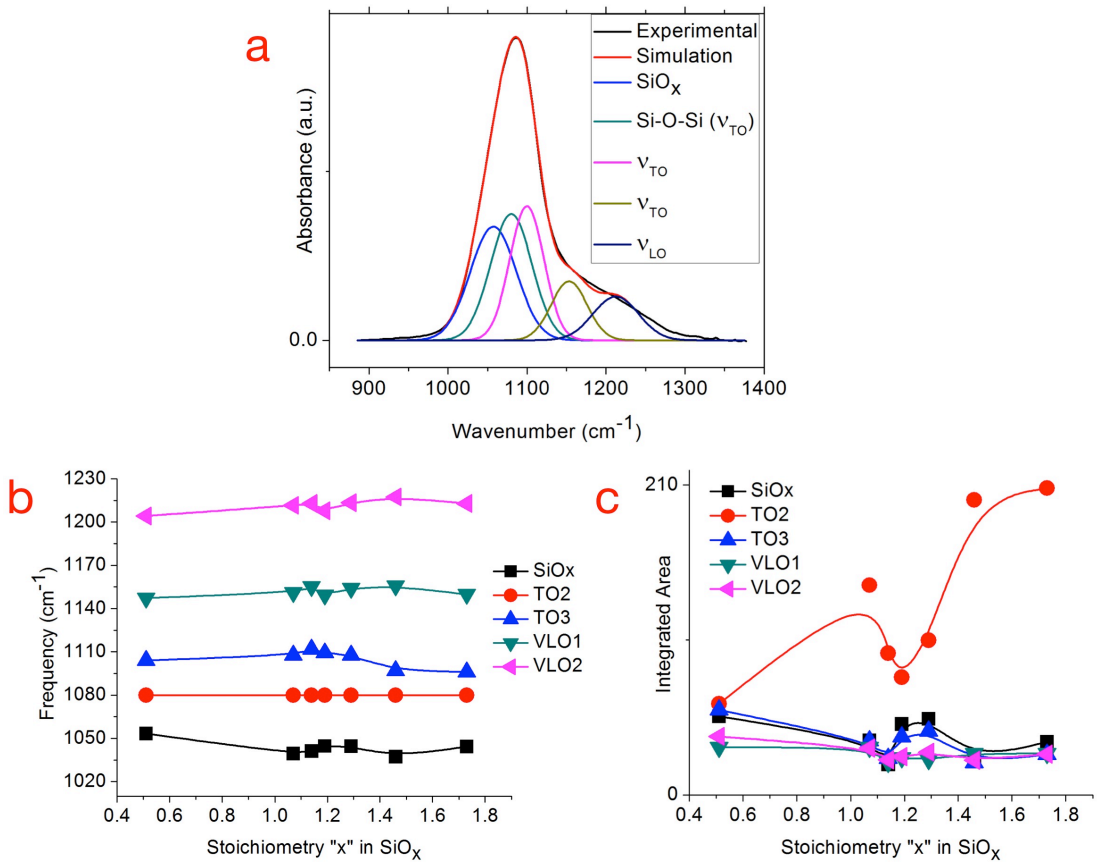

Figure 28 (a) Graph showing an example of the FTIR peak fitting analyses, where the spectrum is dissected into five signals originating from TO and LO FTIR modes of silicon oxide along with the SiO_x signal. The envelope signal of these five signals is colored red and the spectrum obtained experimentally is colored black. **(b)** Graph showing FTIR peak positions and **(c)** integrated peak areas of the signals originating from TO and LO FTIR modes of silicon oxide along with the peak position of the SiO_x signal for 1100 °C post-annealed thin-films with various x values.

It is clearly seen from Fig. 28c that the influence of stoichiometric SiO_2 signal (TO_2) is at its maximum for the SiO_2-rich region, whereas it gradually decreases towards the Si-rich region. However, it is important to note that the influence of this signal abruptly decreases in the intermediate region and the influence of SiO_x signal increases abruptly for the same region. This is another very strong confirmation of the results derived from XPS analyses, namely that there are three representative regions for a set of thin-films, one of which is an intermediate region for which the nominally unstable suboxides are stabilized.

Thus far, we have identified the thin-film stoichiometry, verified thin-film homogeneity, and investigated the chemical bonding dynamics. In order to conclude our chemical investigation, we finally present analysis of crystallinity of the thin-films examined through RS analyses (Fig. 29). Figures 29a and 29b shows RS spectra of the thin-films with various x values that are post-annealed at 1000 °C and 1100 °C, respectively. As can be seen from the figures, the RS spectrum is quite broad with two prominent signals located at 521 cm^{-1} and 485 cm^{-1}, which are originating from crystalline and amorphous phases of Si, respectively [15]. There is also a signal originating from the c-Si/a-Si interface located at 510 cm^{-1} [15]. As seen from the figures, increasing annealing temperature to 1100 °C further enhanced crystallinity, as evidenced from the reduced FWHM of the signal originating from crystalline Si. We have also calculated thin-film crystallinity from the integrated areas of the signals through the equation below and plotted it with respect to various x values as shown in Fig. 29c [115].

$$X_c = \frac{I_c + I_i}{(\alpha I_a + I_c + I_i)},$$

where X_c is the crystallinity, α is a constant, and I_a, I_i, and I_c are the integrated areas of the RS signals originating from the a-Si, c-Si/a-Si interface and c-Si, respectively.

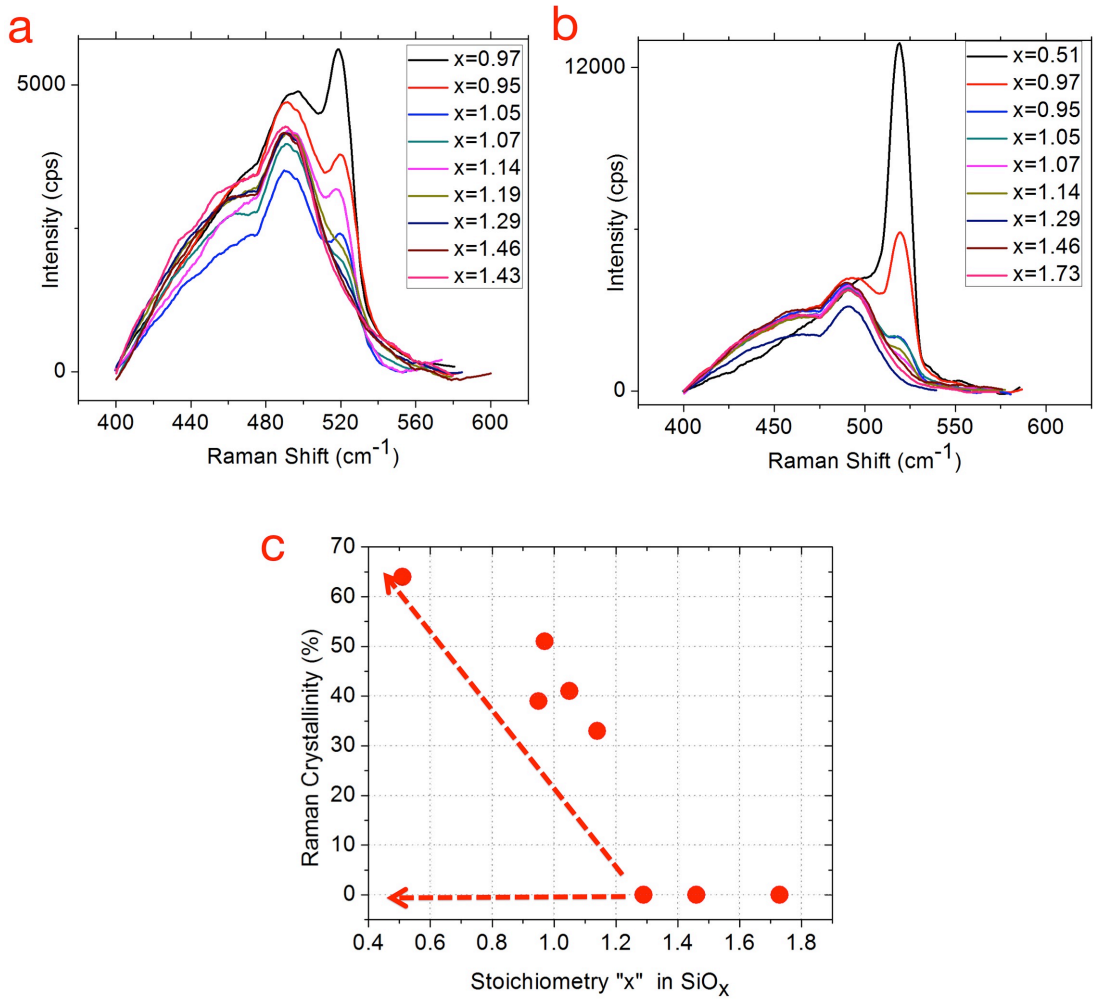

Figure 29 Graph showing RS spectra of the thin-films with various *x* values that are post-annealed at **(a)** 1000 °C and **(b)** 1100 °C. **(c)** Graph showing percentage of c-Si content of the thin-films with various *x* values.

As can be seen from the figure, crystalline content of the thin films increases abruptly when $x < 1.3$ for the intermediate and Si-rich regions, whereas there is no or very small number of c-Si for the SiO_2-rich region. Furthermore, it is evident from the graph that the c-Si content of the thin films is between 30% and 50% for the intermediate region.

To conclude the section, we would like to stress that chemical investigations point to the presence of three regions: Si-rich ($x < 0.9$), intermediate ($0.9 < x < 1.4$), and SiO_2-rich ($x > 1.4$) regions for thin-films with various x values that were fabricated via ballistic deposition. More importantly, the results confirm independently that the intermediate region is composed mostly of substoichiometric, nominally unstable suboxides and that they were not affected by the post-annealing at high-temperatures. This indicates that the intermediate region should be our target range for x values towards fabricating an anisotropic 3D random network of Si quantum dots.

5.2 Structural Investigations

2D- and 3D-morphologies of the Si-rich SiO_x thin-films were investigated through EFTEM and APT analyses (please refer to Section 4.2.2 for the details). We have first examined the effect of post-annealing on the final morphology. Figure 30 shows EFTEM images of as-deposited and 1000 °C and 1100 °C post-annealed thin-film with $x = 1.07$ that belongs to the intermediate region, in which we are interested.

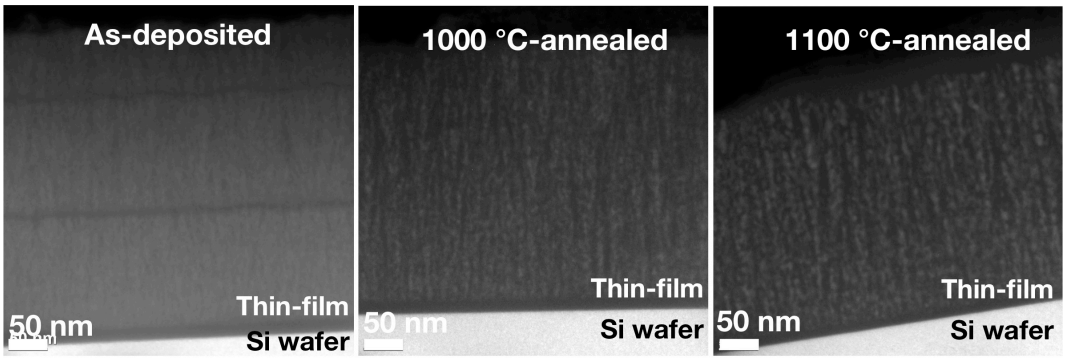

Figure 30 Plasmon EFTEM images showing as-deposited and 1000 °C and 1100 °C post-annealed thin-film samples with $x = 1.07$. Si is bright and SiO_x is dark coloured.

The images show crystallization of Si (bright) after the post annealing procedure. Moreover, they show that the crystallization is further increased when annealing temperature is increased to 1100 °C, evidenced from larger aggregates of Si. It is also observed that Si grows in a columnar fashion inside the thin-film. Even in as-deposited film, the columnar sequencing of Si is apparent, which confirms that the deposition is performed as predicted by the ballistic deposition model. For the sake of clarity, we also present enlarged cross-sectional image of an as-deposited sample in Fig. 31.

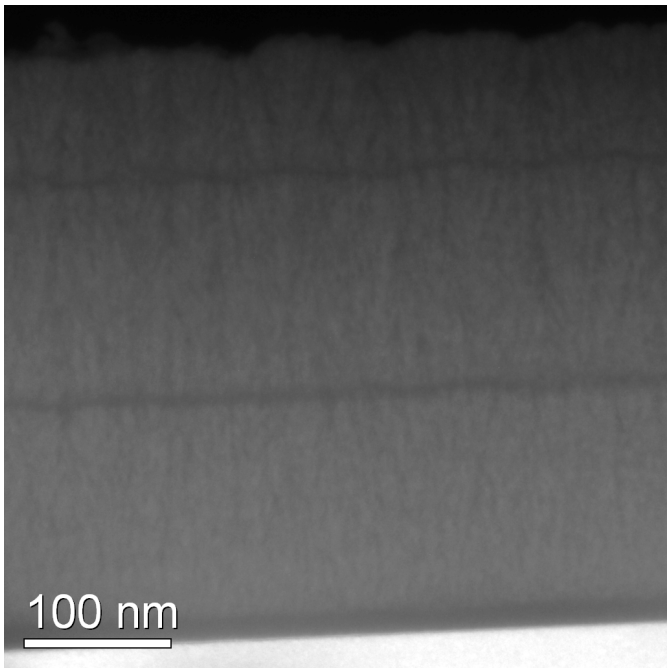

Figure 31 Plasmon EFTEM image showing preferential vertical growth of Si (bright) inside SiO_x matrix (dark) for as-deposited thin-film sample with $x = 1.07$.

We prepared this specimen as a test sample to rule out the possibility that the preferential vertical growth could be the result of a post-annealing procedure. During deposition of this test sample, sputtering from the Si target was interrupted twice to

ensure that the directional growth could reinitiate, as would be expected considering that the growth is stochastic and obeys the rules we have predetermined to control surface diffusion. As observed in Fig. 31, two thin dark layers comprising only suboxides after which the vertical growth of Si has continued in the same manner. This is very strong evidence that the vertically oriented growth is indeed result of the stochastic growth dynamics during ballistic deposition.

Next, we have performed EFTEM analyses on 1100 °C post-annealed thin-films with x = 12.9, x = 1.07, x = 1.01, and x = 0.95 to see if and when the quantum dots are percolated towards a random network (Fig. 32).

EFTEM images of thin-films of an area with dimensions of approximately 300 nm by 300 nm with x = 1.29, x = 1.07, x = 1.01, and x = 0.95 can be seen on the left hand side of Fig. 32 and approximately 50 nm by 50 nm area focused EFTEM images of the same area of the same sample can be seen on the right hand side of Fig. 32. All images on the left hand side show that Si is crystallized and aligned in a vertical direction. Furthermore, when the value of x decreased towards the Si-rich region, meaning that the excess Si concentration of the thin-films is increased, the nanocrystals grow in size. This is clearer from the right hand side images, where it is observed that average sizes of nanocrystals for x = 1.29 are ~2 nm, whereas it increases with decreasing x value to ~6 nm for x = 0.95. It is also seen that the dynamic range of nanocrystal sizes for x = 1.29 sample is wider compared to the other samples, as evidenced from the large number of scattered very small quantum dots and small number of larger dots, which are starting to align along the vertical direction. In the other extreme, the dynamic range of nanocrystal sizes for x = 0.95 sample is much smaller compared to the other samples, considering that the larger quantum dots are almost completely uniform in size and are aligned along the vertical direction. Images for x = 1.07 and x = 1.01 shows similar behavior, where both lateral and vertical connections between the quantum dots are clearly seen, which are more likely to be the random network that we are searching for.

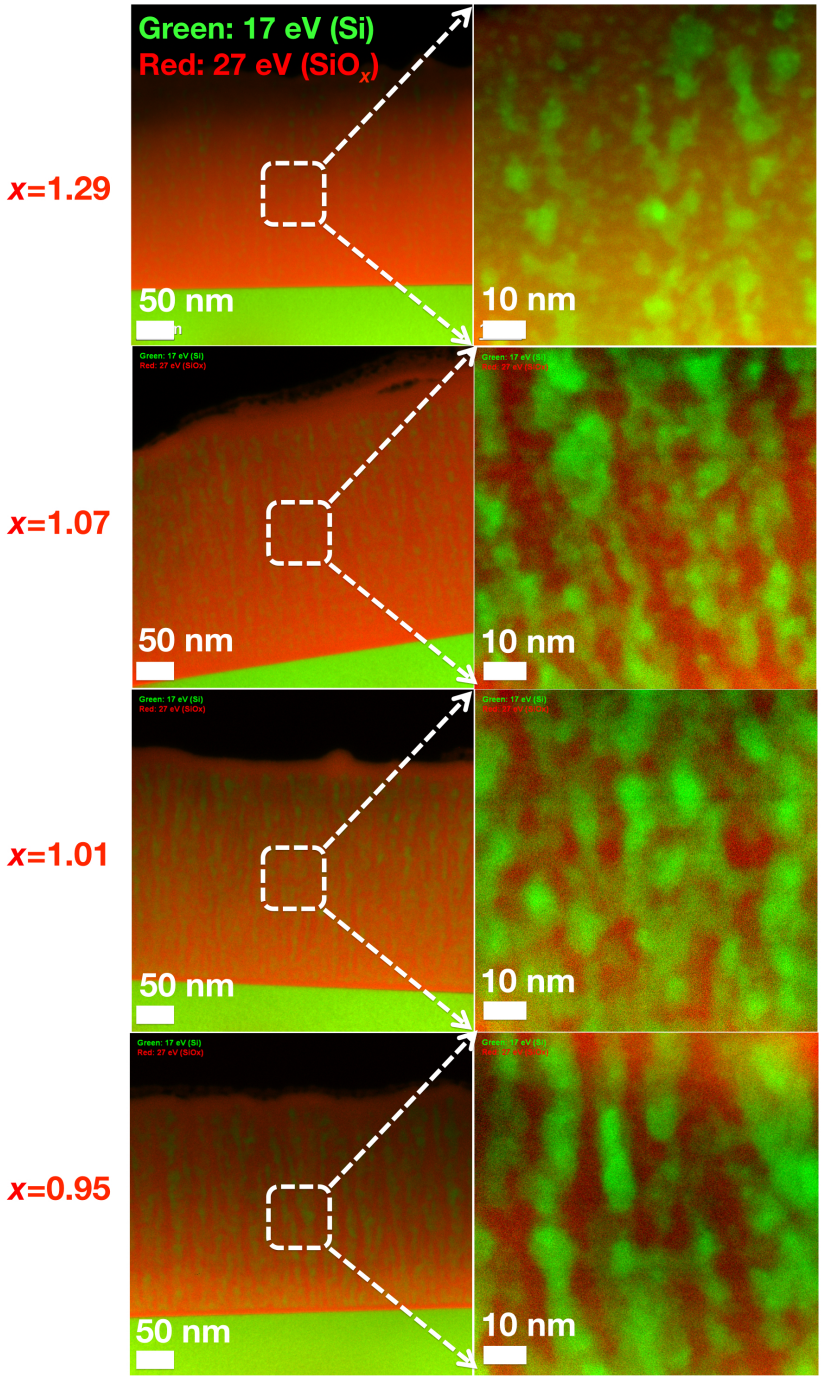

Figure 32 Superposition of the Si (green) and the SiO_x (red) plasmon EFTEM images showing anisotropic, random network of silicon quantum dots for 1100 °C post-annealed thin-films films with x = 12.9, x = 1.07, x = 1.01, and x = 0.95.

More importantly, Fig. 32 is an excellent and completely independent confirmation of the findings of the chemical investigations presented in Section 5.1 that our predictions for intermediate region are valid and that we may have fabricated a random network of Si quantum dots both in lateral and in vertical directions.

Since we have confirmed the network for the intermediate region, we shall call it the "network region" for the rest of this document. In addition, we shall postpone further arguments regarding this region, until after the discussion of the optical and electrical investigations, since our intention was that these networks should exhibit quantum-dot-like optical properties and the current should be flowing through this network without relying on (extremely inefficient) tunneling currents. Instead we shall precede our structural investigations by analyzing the effect of annealing temperature on the microscale and nanoscale morphologies, along with the investigation of the interfaces forming between the thin film and the substrate and between the thin-film and air (Fig. 33 and 34).

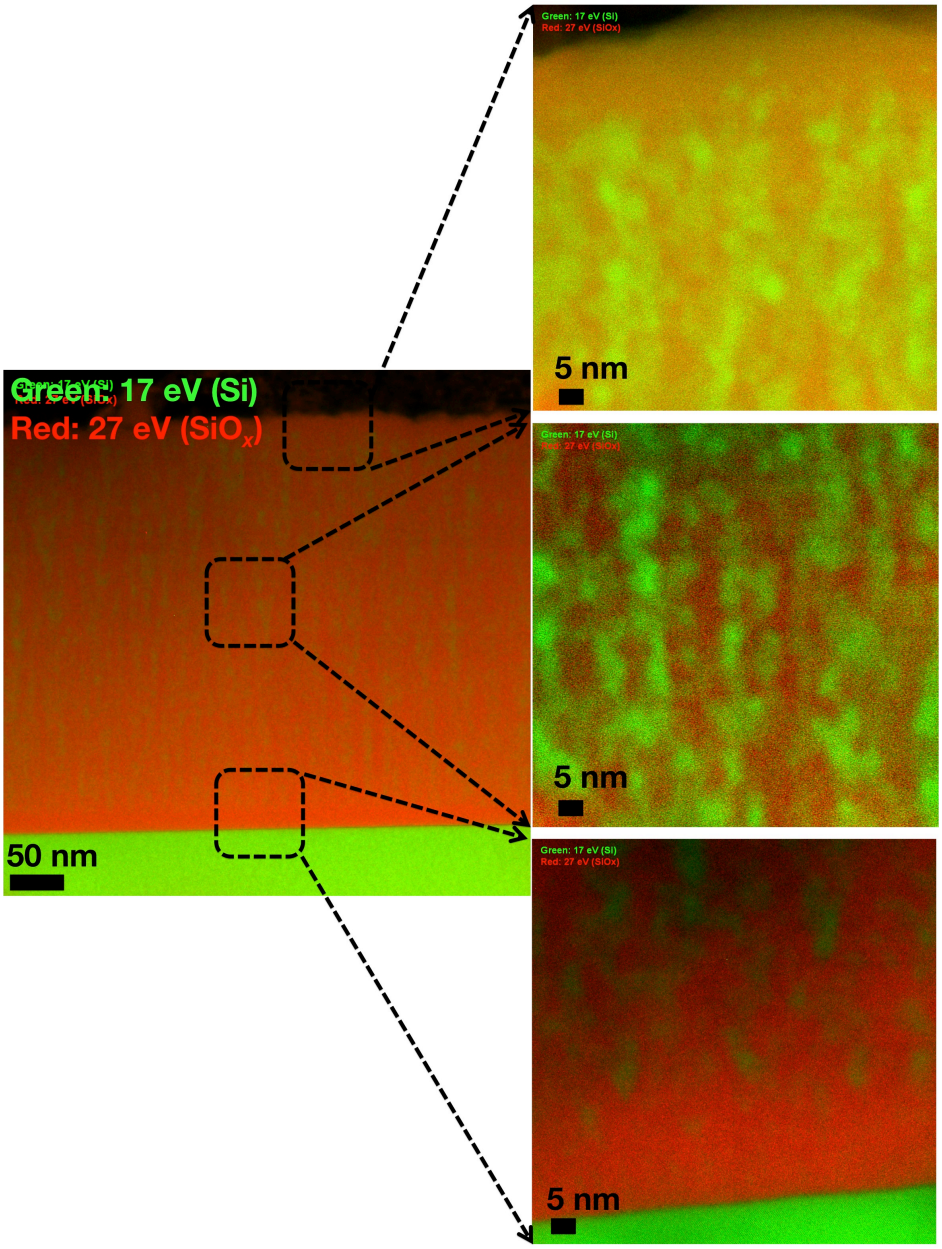

Figure 33 Superposition of the Si (green) and the SiO_x (red) plasmon EFTEM images for 1000 °C post-annealed thin-film with x = 1.07 showing the morphology for approximately 300 nm by 300 nm area (on the left hand side) and interfaces between the thin-film and the air (top), thin-film (middle), and interface between the substrate and thin-film (bottom) for approximately 50 nm by 50 nm area (on the right hand side).

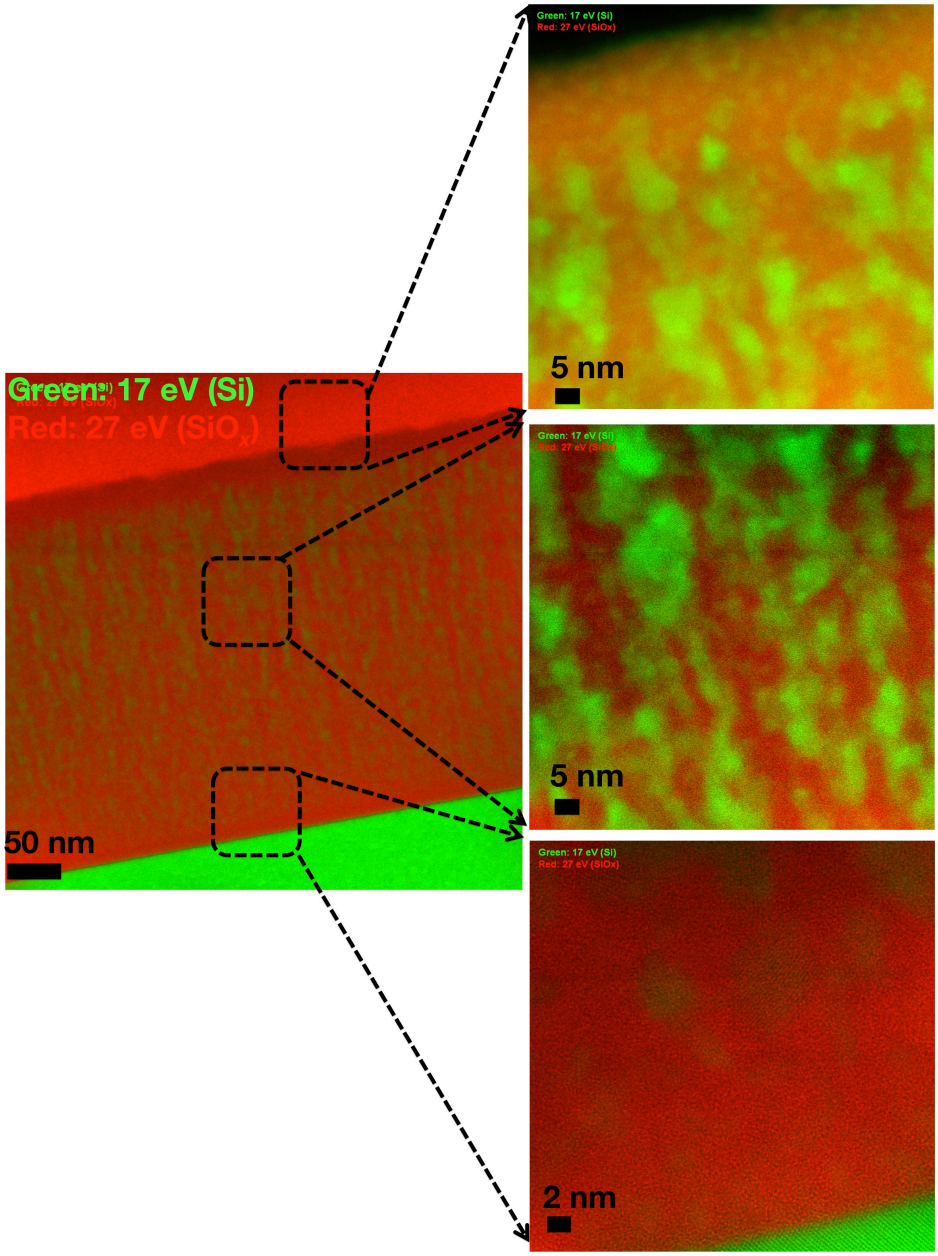

Figure 34 Superposition of the Si (green) and the SiO_x (red) plasmon EFTEM images for 1100 °C post-annealed thin-film with x = 1.07 showing the morphology for approximately 300 nm by 300 nm area (on the left hand side) and interfaces between the thin-film and the air (top), thin-film (middle), and interface between the substrate and thin-film (bottom) for approximately 50 nm by 50 nm area (on the right hand side).

Figures 33 and 34 presents EFTEM images for the 1000 °C and the 1100 °C post-annealed thin-films with x = 1.07, where the images on the right hand side shows the morphology of the interfaces between the thin-film and the air, thin-film, and the interface between the substrate and thin-film, respectively from top to bottom.

As we have concluded before, when discussing the images shown in Fig. 30, increasing the annealing temperature increases the crystallinity, evidenced from increased diameters of the individual quantum dots of the network, as also seen from the Fig. 29, 33 and 34. Upon focusing on the detailed morphology at the interfaces and at the center of the films, we see that both images show ~10 nm-thick surface oxide layer at the surface of the thin films. This confirms the XPS depth-profiling analyses, where we have demonstrated that the first layer etched away is a surface oxide layer (Fig. 22 and 25). In addition, a SiO_x interface is also formed between the substrate and the thin-film. Furthermore, the center of the films seems to be quite homogenous, again confirming the XPS depth-profiling analyses, and quantum dots appears to be percolated.

We have developed a theoretical model and Monte Carlo simulations to understand the effect of ballistic growth on shape anisotropy and percolation of the random network and to help optimize the experimental parameters (please refer to Section 4.3.1 for details). We have run the simulations for various excess Si concentrations and calculated which Si clusters are connected through each other (indicated as blue dots) ultimately to conducting layers at the top and bottom, representing electrodes sandwiching the thin-film (Fig. 35).

First of all, Fig. 35 confirms the vertical orientation of Si nanostructures in the microscale, which theoretically anticipates and even proves our experimental findings that the morphology is the result of ballistic deposition.

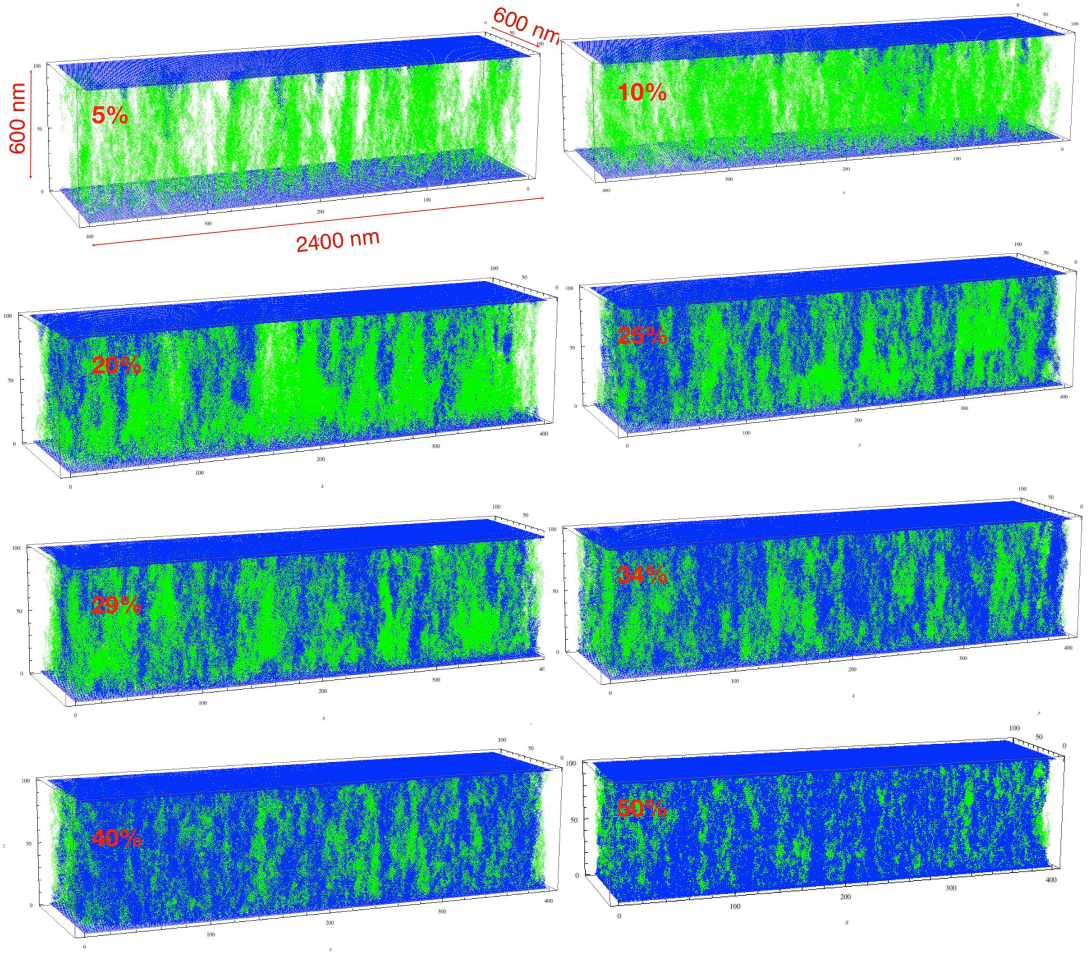

Figure 35 Monte Carlo simulations of ballistic deposition show thin-film morphology for various excess silicon concentrations (as percentages denoted by red color on the top-left of each figure), where green points are isolated and blue points are electrically percolated silicon clusters that are ultimately touching the conducting layers at the top and bottom, representing electrodes sandwiching the thin-film.

Second, as expected, when Si concentration is increased, the fraction of connected Si clusters is increased: At 5% and 10% concentration levels, most of the sites do not contribute to the current flow, since they are not connecting to both of the conducting layers. However, further increase in Si concentration resulted in increasing number

of connections between larger Si cluster networks. At around 40% the number of isolated Si clusters is decreased to a level, at which the network seems to be almost fully connected. In order to evaluate the situation, we have used the data to calculate the ratio of connected Si clusters to those that are isolated and plotted it as a function of percentage of total site occupation with respect to Si ratio (Fig. 36).

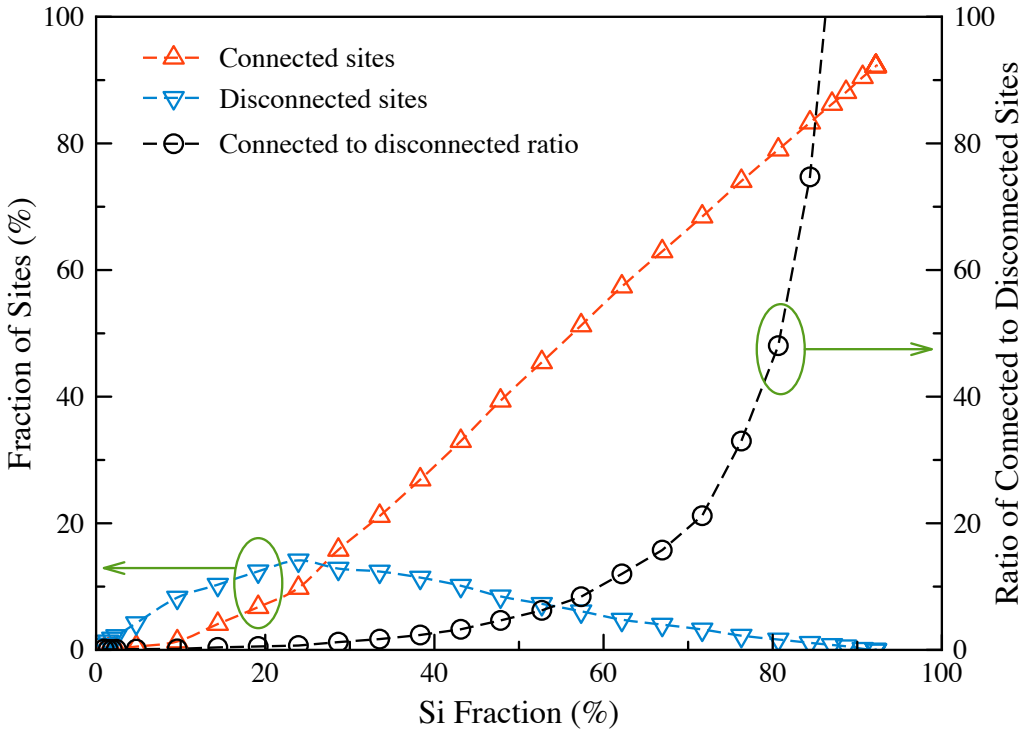

Figure 36 Fraction of connected (red, up-pointing triangles) and disconnected (blue, down-pointing triangles) silicon sites and ratio of connected to disconnected silicon sites as a function of fractional silicon concentration.

It is seen from the figure that when the fraction of Si is increased to ~30%, the number of connected Si sites overtake the number of disconnected sites. However, this still means that approximately half of the charge carriers would not reach the

electrodes. For efficient device operation, the majority of the sites should be connected. The ratio of connected to disconnected Si sites is ~5 at 50% Si concentration and ~10 at 60% Si concentration. These results reveal that at low concentrations, most of the Si sites lack paths connecting them to the electrodes above and below the thin-film. Thus, the disconnected Si sites form small islands of various sizes, like an archipelago, and do not contribute to the conductivity.

More importantly, the numerical model correctly predicts the range of x values for experimentally observed transition from a disconnected archipelago of quantum dots (for $x > 1.3$), to a sparse, but percolated network (for $1.3 > x > 0.8$), finally to a highly connected but overcrowded network (for $x < 0.8$).

We have also confirmed Si percolation for the network region ($x = 1.19$) through molecular dynamics simulations (please refer to Section 4.3.2 for details). An empirical potential was used to optimize the charges of the atoms, which allowed us to use variable charges. This way we were able to run the simulations for several microseconds during which the atomic charges dynamically change at a certain temperature. Figure 37 shows frames captured at various times during these simulations, where Si atoms are colored red and the O atoms are colored blue.

As can be seen from the figure, the simulation starts with an ordered lattice and ends with a relatively disordered lattice for which Si atoms starts to get together to form clusters.

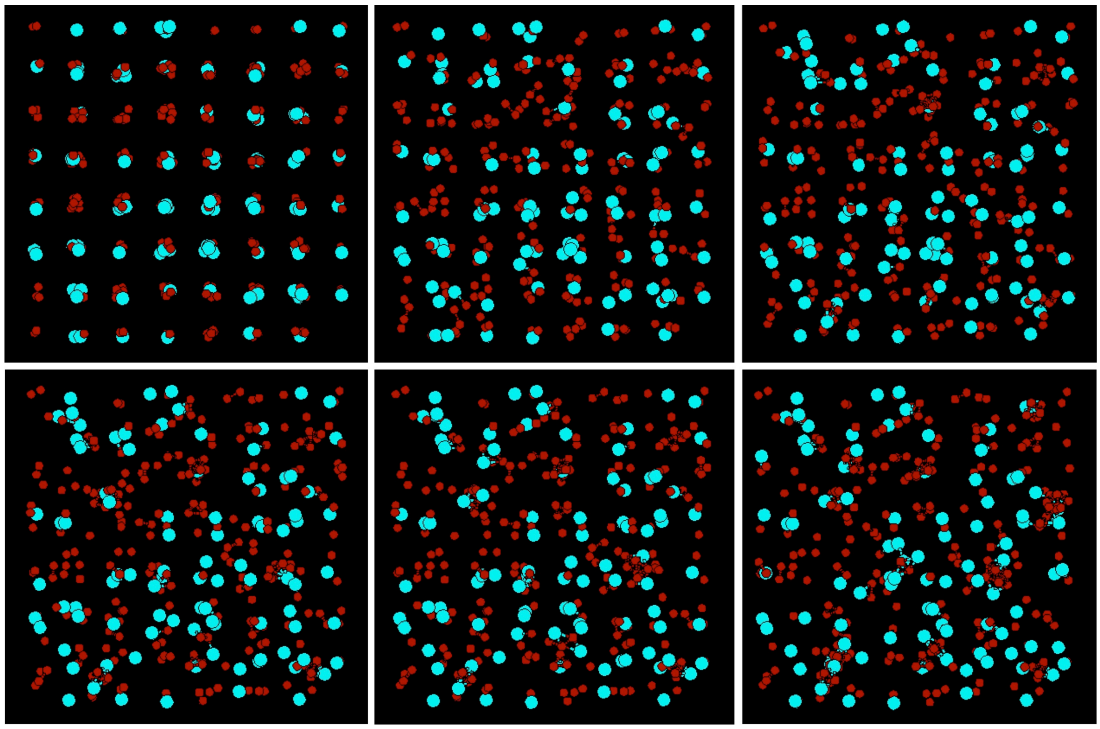

Figure 37 Images showing frames captured at various times during molecular dynamics simulations of SiO_x system, where Si atoms are colored red and the oxygen atoms are colored blue. First frame is the beginning and the last frame is the end of the simulations.

We should stress that these simulations cannot predict the final morphology of the system because they ran for a relatively short period of time compared to the experimental conditions. However, we have managed to isolate Si after several runs and created a 3D image of isolated Si in a 2.6 Å x 2.6 Å x 2.6 Å cube, as seen in Fig. 38, which shows that the atoms are randomly percolated.

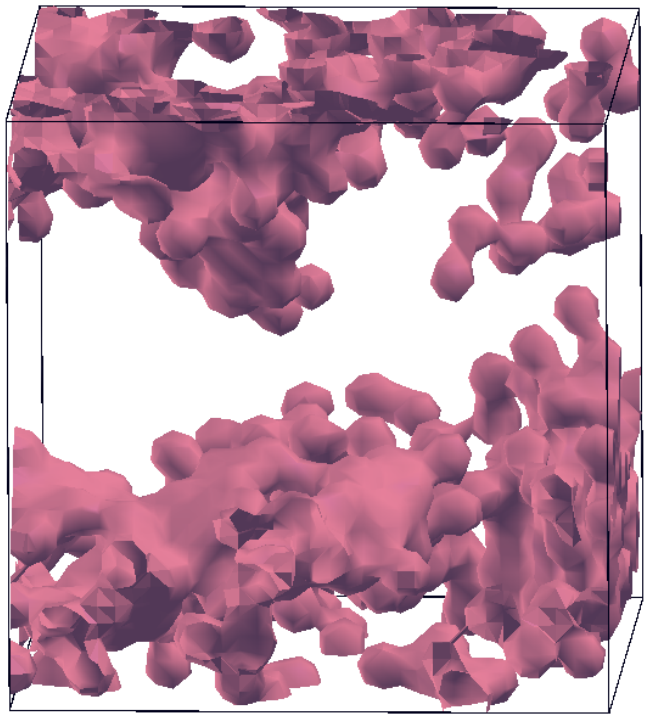

Figure 38 A 3D image of randomly percolated Si atoms (pink) in a SiO_x matrix (white) in a 2.6 Å x 2.6 Å x 2.6 Å cube, calculated from molecular dynamics simulations of SiO_x system.

The simulations also provide a reasonably accurate estimate regarding the presence and amount of Si oxidation states for Si-rich SiO_x systems. We have compared the molecular dynamics simulation results to the XPS- and FTIR-based measurements, regarding the presence and distribution of Si oxidation states with respect to *x*. For the sake of simplicity, we have drawn our XPS findings (Fig. 24) in a sketch as shown in at the top of Fig. 39, where we plot the distribution of Si^{+n} with respect to the three representative regions and the bottom of Fig. 39 displays the coordination number of each Si atom, defined as the number of O atoms that were found within a radius of 2.5 Å, where the density chosen in these simulations was ~5.0 x 10^{22} atoms/cm^3 and the simulations were conducted at a nominal temperature of 1100 °C for three representative regions.

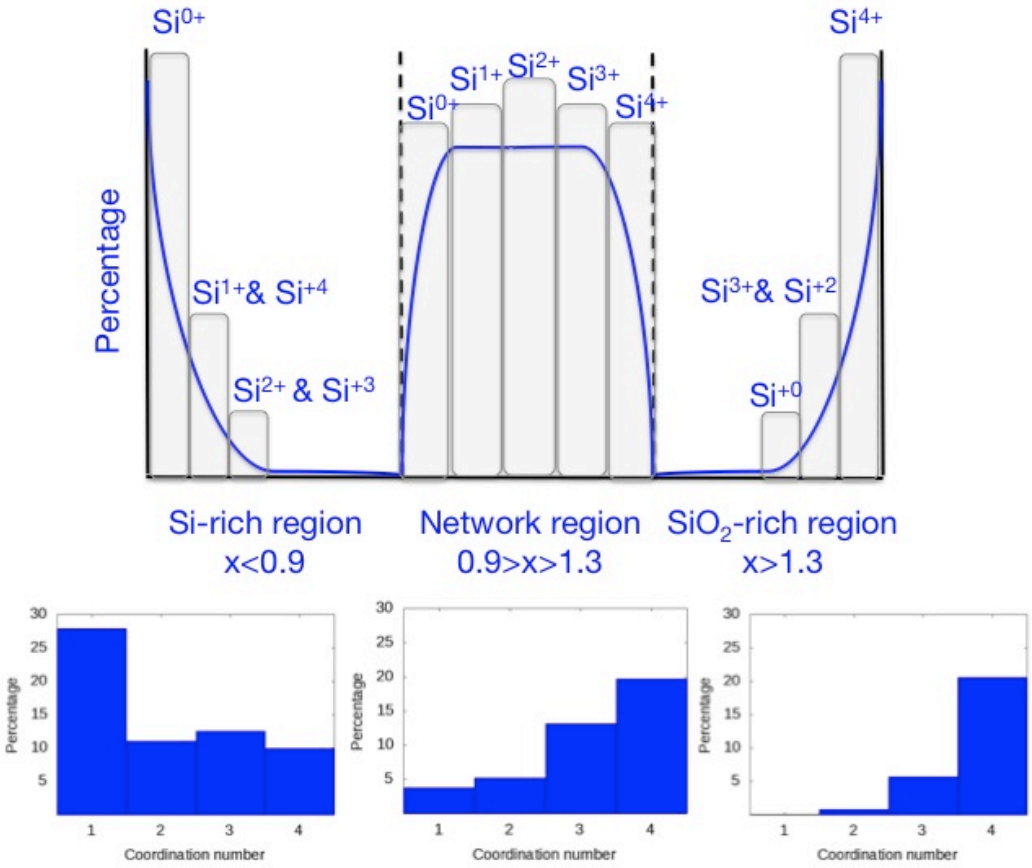

Figure 39 Sketch showing a summary of XPS findings, which shows the distribution of Si^{+n} with respect to three representative regions (top) and histograms displaying molecular dynamics simulations for three representative regions, where the coordination number of Si atoms that are found within a radius of 2.5 Å for atomic density of 5.0 x 10^{22} atoms/cm^3 at a nominal temperature of 1100 °C (bottom). The coordination numbers 1, 2, 3, and 4 of the histograms represents Si^{+1}, Si^{+2}, Si^{+3}, and Si^{+4}, respectively.

As can be seen from the figure, the simplified sketch of XPS findings (Fig. 24) has a very good correlation for the coordination number histograms that were calculated from molecular dynamics simulations for the three representative regions. The

coordination numbers 1, 2, 3, and 4 of the histograms represent Si^{+1}, Si^{+2}, Si^{+3}, and Si^{+4}, respectively. Note that the coordination number of each Si atom is defined as the number of O atoms that are found within a radius of 2.5 Å, which means the percentage of Si^{+0} (Si) is neglected. The histograms show that Si^{+1} (Si_2O) dominates the Si-rich region, Si^{+4} (SiO_2) dominates the SiO_2-rich region, and the network region is mostly composed of suboxides (Si^{+1}, Si^{+2}, and Si^{+3} that are Si_2O, SiO, and Si_2O_3, respectively) verifying the experimental results.

So far, we have presented random network morphology of the thin-films from 2D EFTEM images and verified through theoretical studies. In order to complete the structural investigation, we will present the third dimension of the random network from APT analyses. In order to perform these analyses, the specimen had to be shaped as a needle with an atomically sharp tip. Thinning procedure is performed using an FIB and it is shown step-by-step with SEM imaging as presented in Fig. 40.

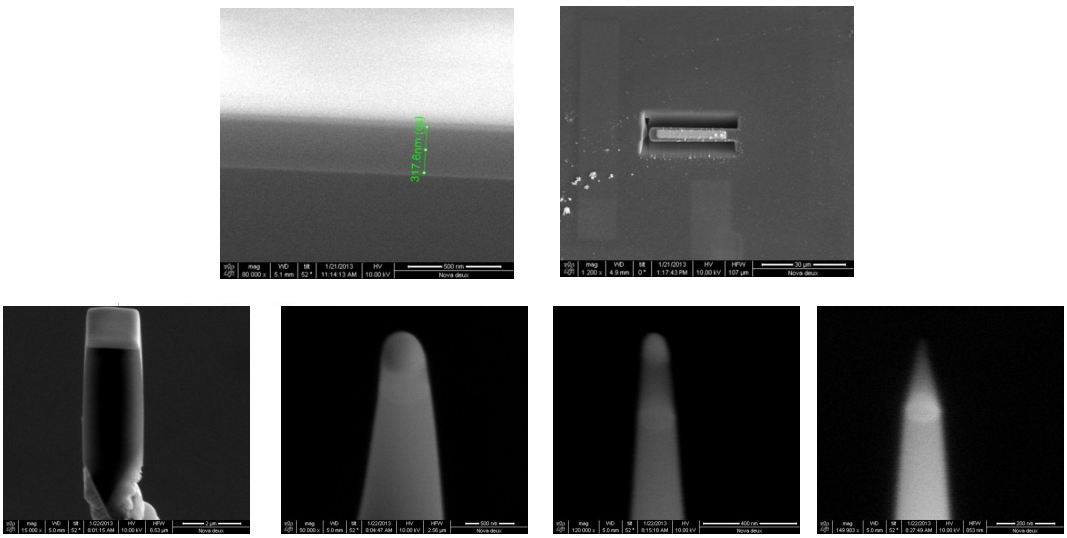

Figure 40 SEM images showing step-by-step shaping of the thin-film to a needle with an atomically sharp tip. TEM image of the thin-film (top, left). SEM image of the FIB-lift out sample is taken from the surface (top, right). Sections of the lift-out

wedge mounted to a series of microtip posts (bottom, left). Each specimen was then sharpened through a series of annular mills (bottom, left to right) to form the final specimen tip (bottom, right).

Figure 40 displays the ~300 nm thick thin-film that is clearly visible from the TEM image (top, left). A FIB lift-out sample was taken from the surface (top, right). Sections of the lift-out wedge mounted to a series of microtip posts (bottom, left). Each specimen was then sharpened through a series of annular mills (bottom, left to right) to form the final specimen tip (bottom, right). The interface between the thin-film and the Si wafer substrate is visible (bottom, left to right).

Since APT analyses cannot be performed for the entire volume for the specimen at once, a cubic volume should be chosen to begin with the analyses. We have tried to acquire the largest volumes possible, four of which were presented in Fig. 41. As can be seen from the figure, the largest volume obtained has dimensions of 65 nm x 65 nm x 110 nm, where Si and O atoms are colored grey and blue, respectively. It is also seen that Si quantum dots are visibly percolated in all of them.

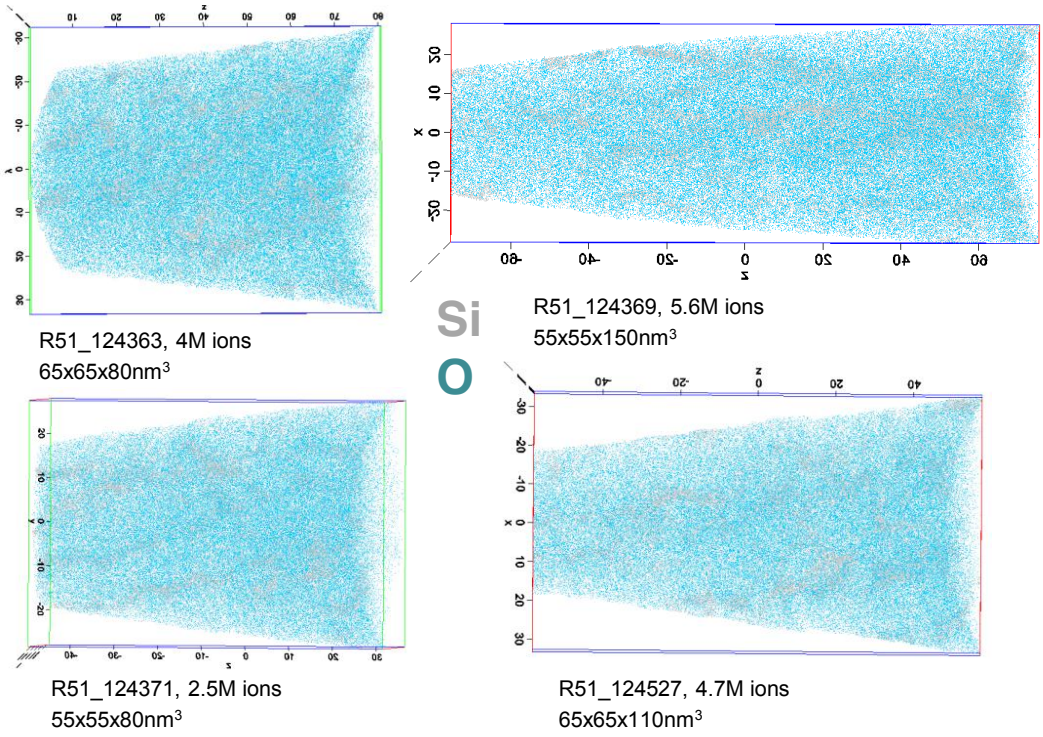

Figure 41 APT images obtained from the 1100 °C post-annealed thin-film with x = 1.07 showing four largest volumes obtained at the beginning of APT analyses, where Si and O atoms are colored grey and blue, respectively.

The next step is to select the correct Si concentration in order to explicitly identify the interconnections between Si quantum dots. This is done through isoconcentration surface analyses. Isoconcentration surfaces can be set to delineate and measure interfaces. An isosurface is a contour. Mathematically it is a 3D surface representation of points with equal values such as concentration, pressure, temperature, density, or concentration in our case, in a 3D data distribution [116]. Figure 42 displays three images obtained for three different isosurface concentrations, namely, 50 at.%, 60 at.%, and 70 at% of Si.

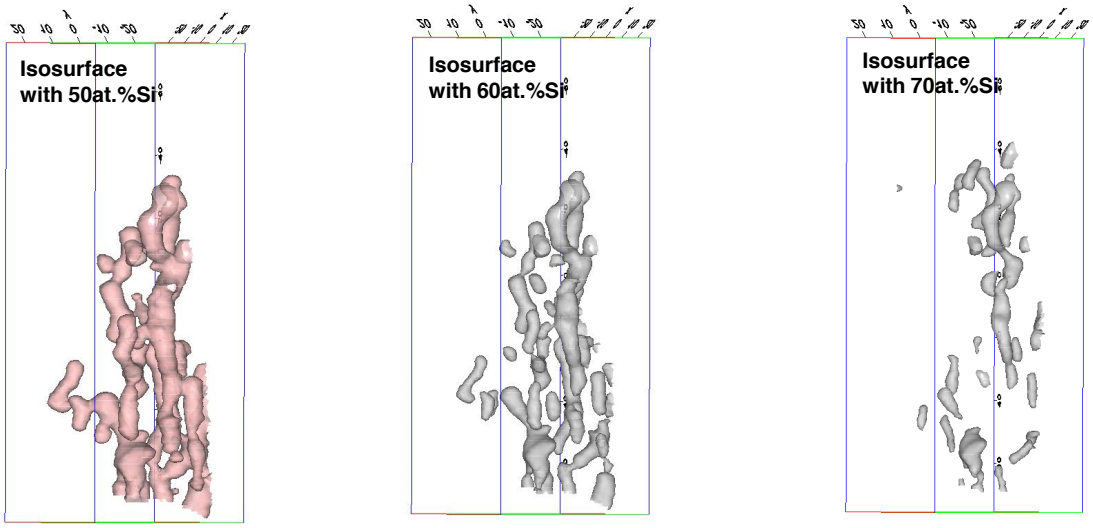

Figure 42 Images showing isoconcentration surfaces of 50 at.% (left), 60 at. % (middle), and 70 at.% (right) of Si concentrations.

The left image show a single, large percolated region of Si quantum dots when the Si isosurface concentration level is chosen as 50 at.%. Center image display a more discontinuous structure when the Si isosurface concentration level is chosen as 60 at.% and the image on the right demonstrates a highly discontinuous structure when the Si isosurface concentration level is chosen as 70 at.%. Note that in isosurface concentration analyses, Si at.% are randomly chosen to determine the optimum concentration for which a correct 3D image can be drawn. As it is obvious, the 50 at.% isosurface is the best concentration level to describe the network morphology and this isosurface level was used to reveal the 3D morphology. Figure 43 shows the result of APT analyses that shows the anisotropic 3D random network of Si quantum dots for an area of 65 nm x 65 nm x 110 nm. Further detailed explanations on APT analyses can be found in ref. [117].

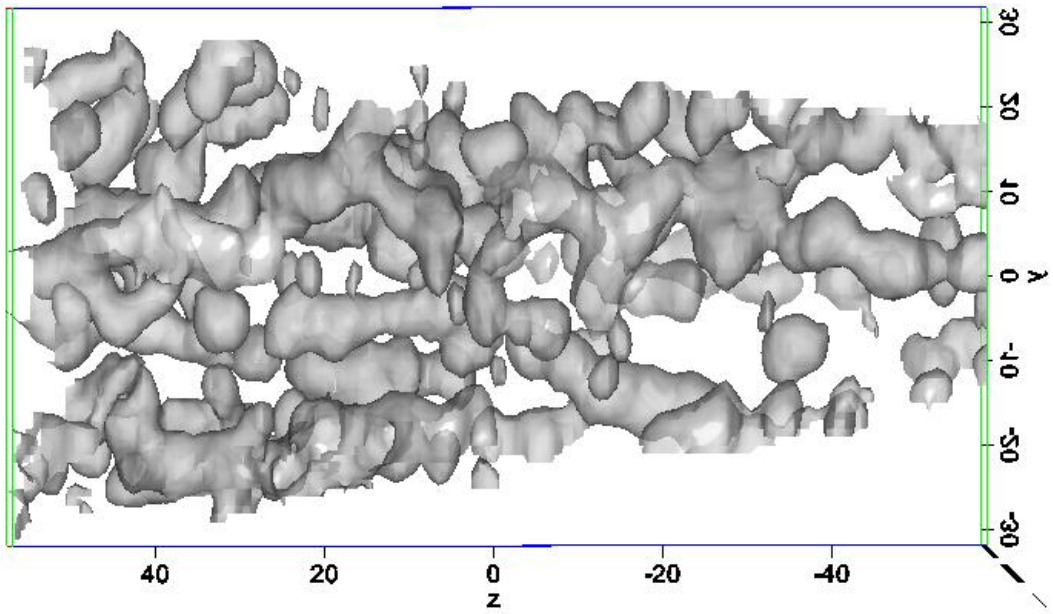

Figure 43 An APT image showing anisotropic 3D random network of Si quantum dots for an area of 65 nm x 65 nm x 110 nm.

To conclude the section, we would like to stress that structural investigations verified our chemical investigations point to the presence of three regions: Si-rich ($x < 0.9$), network ($0.9 < x < 1.3$), and SiO_2-rich ($x > 1.4$) regions for thin films with various x values that were fabricated via ballistic deposition. In addition, structural investigations confirm that the network region is composed mostly of substoichiometric, nominally unstable suboxides and that they are not affected by the post-annealing at high-temperatures. More importantly, both microscale and nanoscale morphology of the anisotropic 3D random network of Si quantum dots are presented through 2D EFTEM imaging and 3D APT analyses. The structural investigations proved without any question that we have fabricated a state-of-the-art Si nanostructure for the first time that is self-assembled in multiscale by utilizing ballistic deposition method: The structure is largely isotropic in the atomic scale,

showing a percolated quantum dot network and it is anisotropic in the microscopic scale, showing a vertically aligned random network of quantum dots.

5.3 Optical Investigations

The optical properties of anisotropic 3D random network of Si quantum dots were investigated through SE, PL, and UV-Vis spectroscopy analyses (please refer to Section 4.2.3 for details). Although our primary goal was to identify the optoelectronic features of the random network, we have extended our investigation for all three regions in order to observe how optoelectronic features are changing when crossing from one region to the other. In this vain, we will first present SE analyses in order to answer a very important question; how do nominally unstable suboxides affects the optical properties of thin-films that belongs to Si-rich, network, and SiO_2-rich regions?

SE is a powerful, easy-to-use, and non-destructive tool that can be used to evaluate a wide range of thin-film properties such as film thickness, crystallinity, average nanocrystal size, chemical composition, surface roughness, optical and dielectric constants, and optical bandgap [111]. Due to its practicality, SE is often preferred over alternative optical characterization methods, especially for nanoscale semiconductor materials, including Si-rich SiO_x thin-films [118-120]. However, the optical and electrical properties of these systems are strongly dependent on a wide range of parameters such as nanoscale morphology and type and chemical composition of the dielectric matrix [15,118-120]. Moreover, these properties depend on the fabrication procedure; in our case it is the ballistic deposition, which makes it essential to identify the optical properties of these thin-films. For these reasons, it is desirable to develop a generic optical model for SE studies that describes the system and characterizes the effect of these parameters. In our recent article [121], we have shown, for the first time, SE investigations on Si-rich SiO_x thin-films over a wide range of stoichiometries ($0 < x < 2$) and analyzed the effect of suboxides on their optical properties. Furthermore, we have presented a generic optical model to

analyze the SE data for Si-rich and SiO_2-rich thin-films, along with the intermediate region, where all the suboxides are stabilized. We have tried to develop a model that is as simple as possible, which consist of a rough surface oxide layer, a thin SiO_2 interface layer that is located between the thin-film and the substrate, and the thin-film layer. Since the composition of thin-films for three regions were different, we have identified the common elements in the light of chemical and structural analyses as a-Si, nc-Si, SiO_x, SiO_2, and void. Later, we have varied the volume concentrations of these species and run the software for simulations to the point where we have gathered good root mean square (RMS) ratio ($r^2 > 0.97$). Finally, we have compared the volume fraction content of the thin-films with those obtained from chemical analyses in order to validate the generality of our optical model.

Figure 44a shows the optical model that we have developed to describe Si-rich SiO_x thin-films for all three regions: Si-rich, network, SiO_2-rich. When we try to simulate the SE data obtained from the thin-films using this simple model, we have seen that the simulations were perfectly matched with the experimental data for Si-rich region. However, in order to successfully describe the thin-films from network and SiO_2-rich regions, we had to ignore the interface layer by setting its thickness to 0. This can be explained by the nature and distribution of the suboxides in the thin-films: As in the case of network and SiO_2-rich regions, Si-O bonds from SiO_x and SiO_2 dominate the chemical environment of the thin-films. Although there is an interface layer present between the thin-film and the substrate, it is rich in Si-O bonds so that the chemical environment of this interface layer is very similar to that of the thin-film layer, it behaves as if the interface and the thin film layers are fused together (for the SiO_2-rich region see Fig. 44b and for the network region see Fig. 34). Consequently, there is no need to introduce an extra interface layer to the optical model for these two regions. On the other hand, in the Si-rich region, the phase separation of Si and SiO_2 is much more prominent. Unlike the intermediate and SiO_2-rich regions, Si-Si bonds, surrounded by Si–O bonds, have a dominating influence on the chemical environment of the thin-films. This naturally evolves into a structure where a distinct

SiO_2 interface layer forms between the film and the substrate. The presence of the interface layer (red) between the c-Si substrate (green) and the thin-film for the Si-rich region is can be seen from the EFTEM images presented in Fig. 44c.

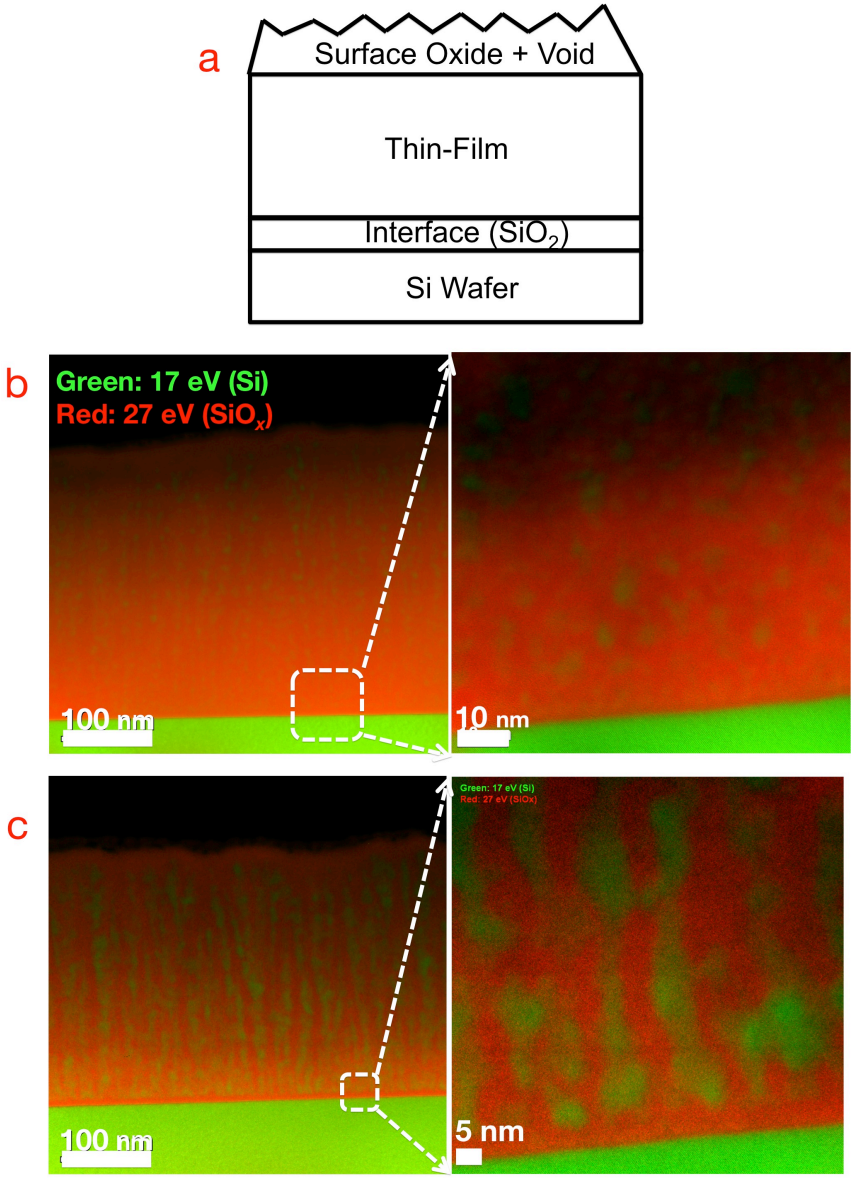

Figure 44 (a) Schematic of the optical model developed to describe the content of Si-rich SiO_x thin-films over a wide range of stoichiometries ($0 < x < 2$).

Superposition of the Si (green) and the SiO_x (red) plasmon EFTEM images obtained from 1100 °C post-annealed thin-films with **(b)** x = 1.19, where no significant interface layer seen between the substrate and the thin-film, and with **(c)** x = 0.51, where a well-defined thin interface layer between the substrate and the thin-film [121].

Figure 45 shows SE spectral data of the ellipsometric angles, Ψ and Δ, and mathematical fits to them, calculated using the generic optical model shown in Fig. 44a for the three representative regions: Si-rich ($x < 0.9$), SiO_2-rich ($x > 1.7$), and the network ($0.9 < x < 1.3$). As can be seen from Fig. 45, simulations fit extremely well to the experimentally obtained data of ellipsometric angles (Ψ, Δ) for Si-rich (Fig. 45c) and SiO_2-rich (Fig. 45a) regions using the optical model shown in Fig. 44a. However, for the network region, there is some deviation seen between the simulation and the experimental data (Fig. 44b) even though the RMS ratio is high ($r^2 = 0.95$). This can be explained by the increased volumetric fractions of suboxides in this region. We describe the suboxides as a combination of SiO_2 and void in our optical model, where the void fraction is not fully independent, thus preventing an excellent fitting. In addition, there can be stress relaxation in the system when volumetric fractions of the suboxides increase. Barbagiovanni, *et. al.* [107] studied Si quantum dots embedded in SiO_2 and performed an extensive XPS analysis, based on which they claim that when Si_2O_3 is present in the system no stress on the quantum dots is observed. Furthermore, through molecular dynamics simulations, Soulairol, *et. al*. [122] found that Si_2O helps relieve the stress in Si quantum dots embedded in SiO_2 through a Si-O-Si bridging bonds.

In addition, Fig. 45 contains valuable information on Si crystallization. The SE spectrum shown in Fig. 45a is similar to the well-known SE spectral data of SiO_2, which has an oscillatory form. This is to be expected since we know from the XPS analysis that for $x > 1.3$ (SiO_2-rich region) SiO_2 dominates the structure. Moreover,

Fig. 45b shows a decrease in oscillations and emergence of a broad feature between 4 and 5 eV photon energies, which indicates the formation of Si nanocrystals [121] for the network region, as also confirmed by the RS and EFTEM analyses (please refer to the Sections 5.1 and 5.2). The oscillations seen in Fig. 45c are further reduced in the Si-rich region and the broad feature becomes more prominent between 3 eV and 5 eV of photon energies.

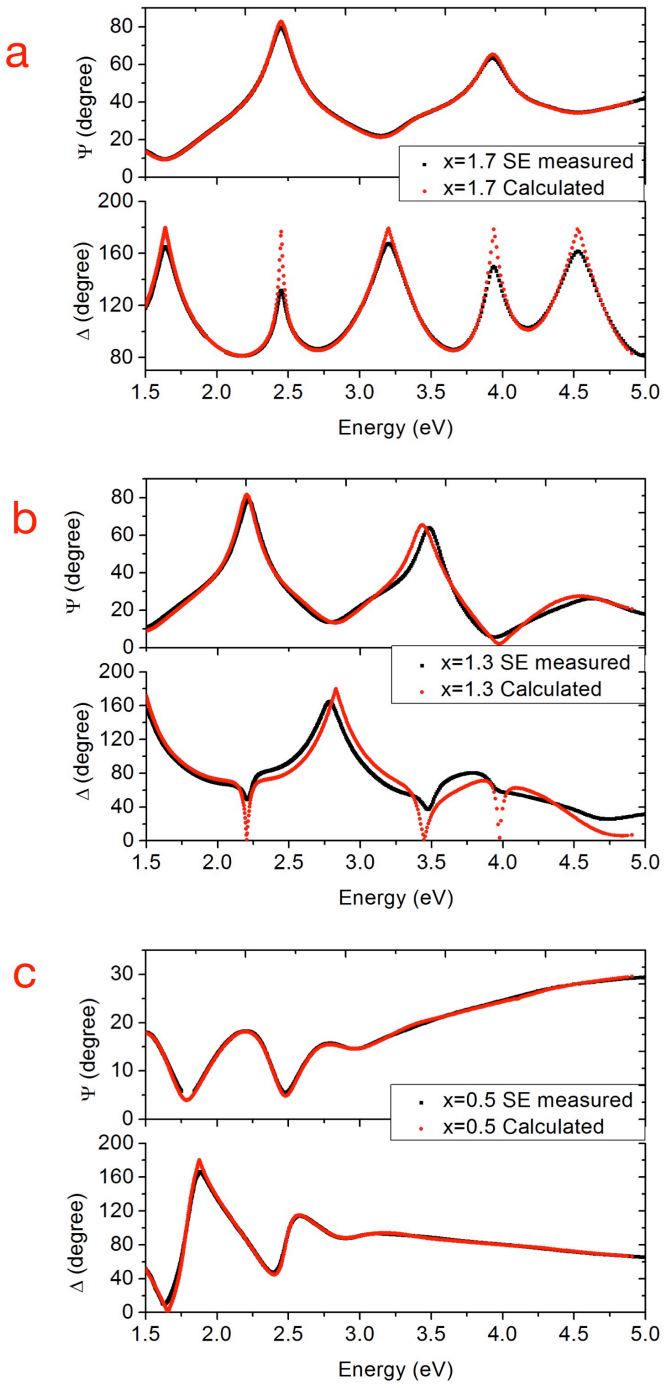

Figure 45 Graph showing the SE spectra of the ellipsometric angles Ψ and Δ and mathematical fits to them, calculated using the optical model that was developed in this study for **(a)** SiO_2-rich (x = 1.7), **(b)** network (x = 1.3), and **(c)** Si-rich (x = 0.5) regions [121].

Next, the real (ε_r) and imaginary (ε_i) parts of the complex dielectric function of the thin films representative to three regions are extracted from the ellipsometric angles (Ψ, Δ) in order to investigate their x-dependencies as seen in Fig. 46. The figure also displays the SE spectra of bulk c-Si for the sake of comparison. As can be seen from the figure, there are prominent oscillations in ε_i and ε_r spectra of the SiO_2-rich region. These oscillations start to decrease for the network and Si-rich regions. In these regions with the nanocrystal Si formation, two slightly prominent features begin to appear at ~3.3 eV and ~4.3 eV, respectively. These are attributed to the critical points of c-Si; 3.3 eV for E_1 and 4.3 eV for E_2, respectively [121]. Although the amplitudes of these two points for c-Si spectra are higher and the peaks are narrow, critical points of the nanocrystals show both peak broadening and decreases in amplitude since their finite size distribution broadens the transitions [123]. Due to the crystal sizes being much smaller than the wavelength of the laser used, we do not gather primary information (directly from the individual nanocrystals), but we do gather secondary information (as a function of the average nanocrystal density) from the nanocrystals. Basically, the presence of the nanocrystals results in minute variations in the effective susceptibility of the medium, which are impressed on the optical phase of the reflected laser beam and in turn are unraveled thanks to the extremely high resolving power of optical phase detection. It is clear from this picture that the strength of any signal from the nanocrystals is proportional to their density. Consequently, we can only observe a slight feature of critical points. In their work, Kovalev, *et. al.* also confirmed this idea [124]. It has been reported in numerous studies that the amplitudes of the signals originating from the critical points decrease, while the peaks broaden significantly due to small nanocrystal sizes [120,124,125]. One reason may be the negligence of excitonic effects, which are important in bulk spectra [124]. Agocs, *et. al.* [120] attributed decrease in the amplitude and the broadening phenomenon to increasing porosity and increasing grain boundaries. Lee, *et. al.* made a similar observation and concluded that this can be attributed to the inadequacy of band structure in nanocrystallites due to their extremely small volume and increased surface effects [125].

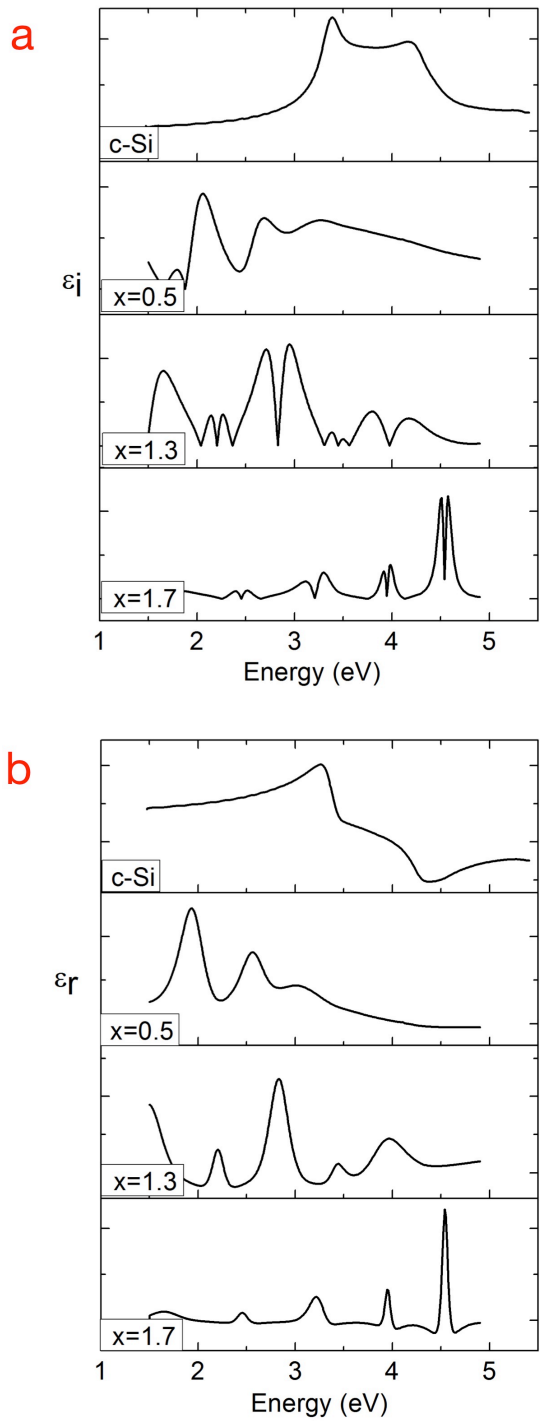

Figure 46 Graph showing SE spectra of (a) the imaginary part, ε_i, and (b) the real part, ε_r, of the dielectric functions for thin-films that belong to Si-rich (x = 0.5), network (x = 1.3), and SiO_2-rich (x = 1.7) regions [121].

The sharp intense structures observed for the SiO_2-rich region in the dielectric function spectra shown in Fig. 46 suggest a Fabry-Perot-like interference [121], which point towards a sharp, high-finesse interface between the c-Si substrate and the thin film. This is consistent with our optical model (Fig. 44a) and the EFTEM image (Fig. 44b), which shows that the thin-film is immediately grown on the c-Si substrate. However, the interference peaks are broadened to some extend for the network region, which points to a low-finesse, structured or rough interface. In addition, for the Si-rich region, the interference peaks are further broadened, also indicating a low-finesse, rough interface between the c-Si substrate and the thin film. This is consistent with the formation of an ultra-thin SiO_2 interface layer between the thin film and the c-Si substrate and this interface is not extremely flat. In other words, this SiO_2 interface layer acts in a manner similar to an index-matching layer in the sense of reducing the sharpness of the interface (Fig. 44c). This results in the broadened features observed in Fig. 45. Gravalidis, *et. al.* [126] reported a study where they observed growth of the thin-films in real time and analyzed optical characteristics of SiO, SiO_x, and SiO_2. They have also reported dominant interference fringes and related them to multiple reflections of the probe light at the back interface between the SiO_x film and the c-Si substrate, thereby to the thickness and the stoichiometry of SiO_x of the films. Clearly, these features need further study.

Lastly, we have extracted the values for the optical constants, namely, the refractive index (n) and the extinction coefficient (k) for the thin films of various x-values (Fig. 47). As it is seen from the figure, both n and k values decrease when x increases towards the SiO_2-rich region as expected [108]. However, there is a kink in the n and k curves for the network region. This is not surprising since we know from chemical, structural, and optical analyses that the material properties changes dramatically. As the strong experimental evidence suggests, this is due to the presence and dominant influence of suboxides in the network region. Since suboxides are nominally unstable, the Si-O bonds are disordered compared to a stable medium where suboxides are phase separated into Si and SiO_2.

In previous studies, this type of behavior is also observed experimentally for SiO_x films, where Tomozeiu *et.al.* [108,127] explained that the phenomenon is due to the fact that SiO_x structure changes from a random distribution of the Si–O bonds in the material bulk (RBM model) to a random mixing model (RMM).

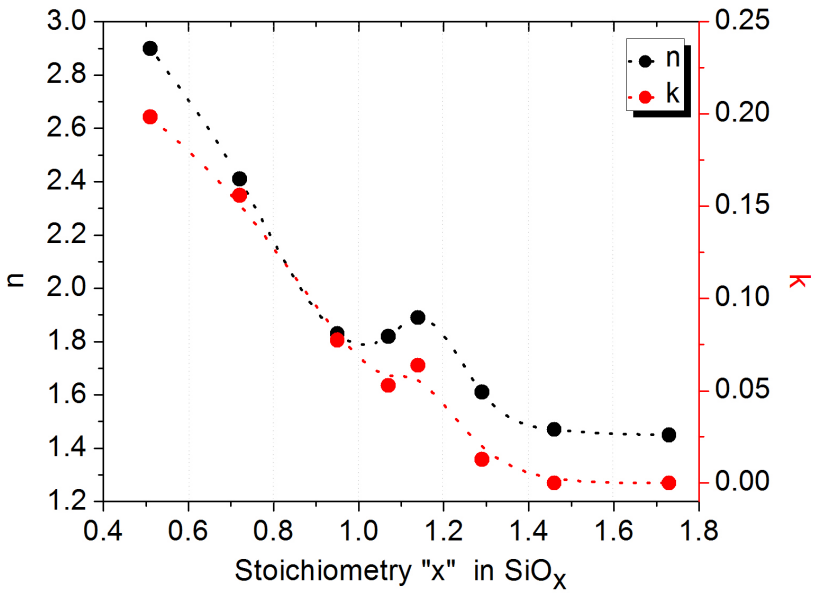

Figure 47 Graph showing optical constants, *n* and *k*, extracted from SE analyses and plotted as a function of *x*.

Thus far, we have presented a generic optical model to describe the SE spectral data of the thin-films representative to three regions. We have shown that the optical properties and optical constants along with dielectric functions of the system are highly dependent on the value of *x*, consequently the thin-film content. We will now proceed with the PL analyses in order to investigate quantum confinement phenomenon for the three regions. Figure 48 shows PL spectra of the thin-films with various *x* values that were post-annealed at 1000 °C (top, left) and 1100 °C (top, right).

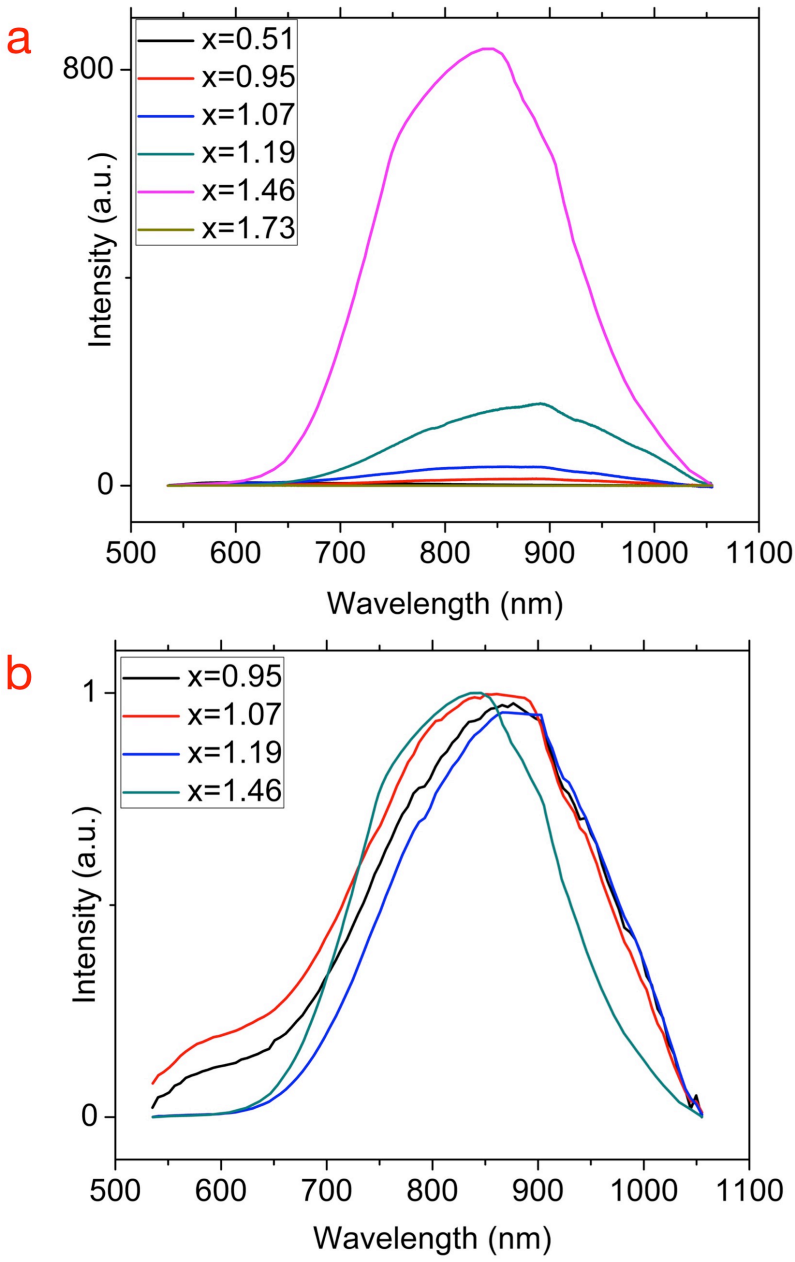

Figure 48 Graph showing **(a)** PL spectra of the thin films with various *x* values that are post-annealed at 1100 °C and **(b)** Normalized PL spectra of the thin-films that represent three regions.

Figure 48a shows that the PL response of the thin film with x = 1.46 is the largest, followed by the thin films with x = 1.19, x = 1.07, and x = 0.95. On the other hand, the thin films with x = 1.73 and x = 0.51 do not show any PL response. As we have concluded earlier in Section 5.1, the thin film with x = 1.73 is almost pure SiO_2, for which we do not expect any PL response. In the other extreme, the thin-film with x = 0.51 is almost like bulk Si, for which we also do not expect any PL response. However, a very strong response for the thin film with x = 1.46 suggests that the contents of this films are rich in quantum dots, which are isolated enough to confine their electrons in all spatial dimensions [128-130]. On the other hand, upon entering the network region (x = 1.19, x = 1.07, and x = 0.95), we still observe a PL response but the intensity is dramatically reduced. As we know from EFTEM analyses shown in Section 5.2, the quantum dots are connected to each other, while preserving their initial diameters before they form a network. The PL intensity decrease is then most probably due to the fact that in the random network, unlike quantum dots, electrons are not confined in all three dimensions, resulting in partial loss of confinement for each quantum dot along the spatial direction it is connected to another dot [131]. However, thanks to the network being randomly connected, quantum confinement is still preserved on average, as evidenced from the less intense but still strong PL emission. More importantly, the spectral blueshift with respect to x is observed from Fig. 48b that confirms that anisotropic 3D random network of Si quantum dots exhibits quantum confinement [15,27,28,128-130].

We have also verified quantum confinement for the network region through UV-Vis and SE analyses, where we have calculated the optical bandgap values as presented in Fig. 49. We have determined the bandgap values using Tauc plots calculated from UV-Vis analyses (please refer to Section 4.2.3) and compared to the bandgap values derived from SE studies. As shown in Fig. 49, the bandgap values are in good agreement for the two independent analyses techniques. It is seen that the bandgap decreases from ~4 eV for the SiO_2-rich region (for x = ~1.8) to ~1.6 eV for the Si-rich region (for x = ~0.5). In the network region, the bandgap ranges between ~1.9 <

E_g < ~2.8 eV, confirming that the nanostructures are quantum confined. It is also interesting to observe that the linear fitting of E_g data requires two lines with different slopes. In other words, there is again a kink point observed when evaluating the optical bandgap of thin-films with various x values. This is also experimentally observed in previous studies [82,108,127,132]. This kink, again, happens to be in the network region, confirming our earlier findings and claims that the material properties drastically changes in the network region, due to influence of nominally unstable suboxides. Furthermore the random network structure most definitely affects the optical bandgap as scrutinized theoretically by Keleş *et.al.* [133].

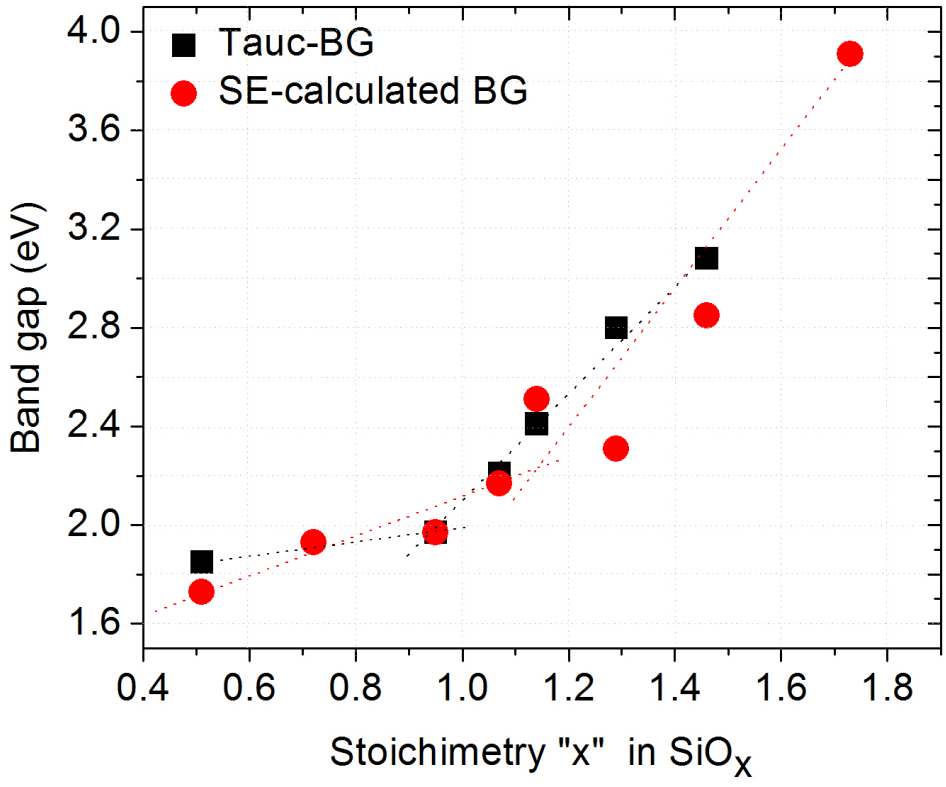

Figure 49 Graph showing optical bandgap values of the 1100 °C post-annealed thin-films that are calculated from SE and UV-Vis spectroscopy analyses and they are plotted as a function of x.

To conclude the section, we have identified the optical properties of the anisotropic 3D random network of Si quantum dots. We have presented a simple, generic optical model in order to interpret SE data of Si-rich SiO_x thin-films in a wide range of stoichiometries and investigated the effect of suboxides on the optical properties. More importantly, we show that the anisotropic 3D random network of Si quantum dots are quantum confined nanostructures and their bandgap energies can be tuned in a range that covers the visible light spectrum, where half of the sun's power lies in. This suggests that the Si quantum dot network is a very strong candidate for use in photonic devices [4,24-26], specifically solar cells [14-16,19,22-24,27-29].

5.4 Electrical Investigations

Now that it is proven that we have fabricated anisotropic 3D random network of Si quantum dots in a range of *x* values via ballistic deposition and the bandgap of this unique structure can be tuned over a wide range of energies, we need to provide the proof of good electrical conduction where current flows through the network structure, without relying on inefficient tunneling currents. However, the reader should bear in mind that in none of the device configurations shown in this section we used doped thin-film, rather we used intrinsic thin-films since the scope of these investigations is to determine the electrical properties of the anisotropic 3D random network of Si quantum dots. Furthermore, we have tried to anneal the metal contacts evaporated onto thin-film for *I-V* measurements along the vertical direction, however upon annealing, metal contacts diffused into the thin-film, where the structure is a random network of vertically aligned nanocrystals, leading to a short circuit. For this reason, we did not anneal the metal contacts for the electrical investigations presented in this section, not only for the vertical measurements but also for the lateral measurements for the sake of comparison. Obviously, this affects the *I-V* measurements since the extra resistance due to the unannealed contacts introduces an additional Schottky barrier effect, which reflects on the *I-V* graphs in the form of nonlinear curves [134,135]. However, since this extra resistance is constant when

comparing one configuration to the other, conclusions drawn from the variations on the curves are unaffected.

We have performed *I-V* measurements on various device configurations as could be seen from Fig. 19 (please refer to Section 4.2.4 for details). First, we have taken *I-V* measurements between two coplanar Al electrodes evaporated onto the film surface on a quartz substrate (Fig. 50a) for lateral conductivity and between the Al point contacts evaporated onto the film surface and Al contact that completely covers the Si substrate (Fig. 50e) for vertical conductivity of 1100 °C post-annealed thin-films with various x values.

Figures 50b and 50c shows *I-V* plots for measurements taken under dark conditions, where we observe linear ohmic currents for the thin-films with $x = 0.51$ (Si-rich region) and $x = 0.97$ (network region) along the lateral direction. Although, we have confirmed through chemical, structural, and optical characterizations that the thin films in the network region ($0.9 < x < 1.3$) are laterally connected, this is not reflected in the lateral *I-V* measurements, except for the thin-film with $x = 0.97$. This is due to the fact that we were limited by the device configuration. Allow us to explain: *I-V* curves reflect only the current flow between two coplanar Al contacts (Fig. 50a), which accounts for a thin section close to the surface, rather than the ~330 nm-thick film. Considering that the metal contacts are not annealed, we are considering contributions from a very thin surface layer. Furthermore, the magnitude of the lateral conductivity is also affected negatively by the distance of 1.5 cm between two coplanar Al contacts, which exceeds the transport distance limited by the charge carrier lifetimes. However, full electrical characterization of this complex morphology is beyond the scope of this thesis and we preferred to keep these simple device configurations to characterize the lateral and vertical conductivities in order to obtain unambiguous results with straightforward interpretations.

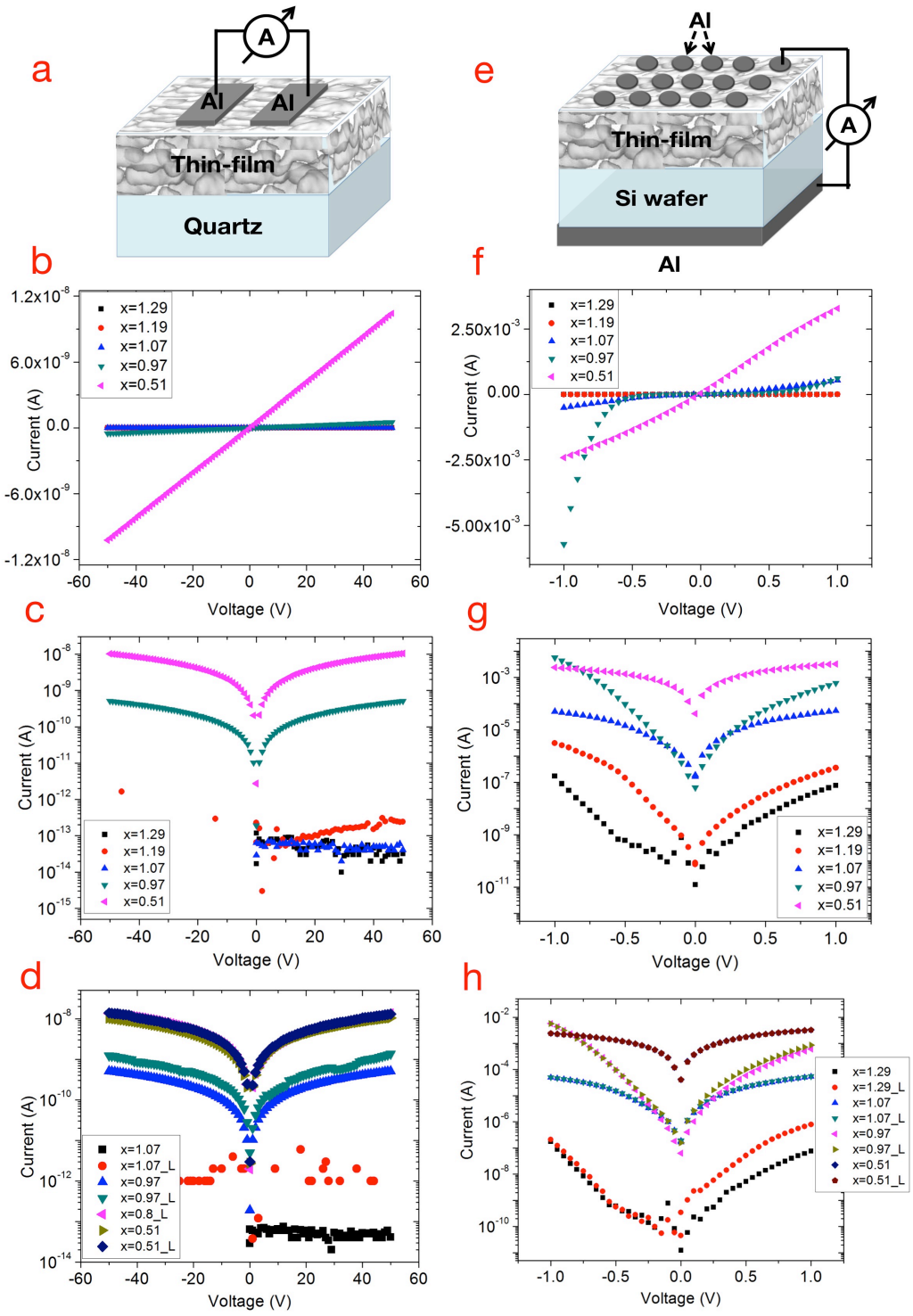

Figure 50 (a) Schematics of the device used to conduct *I-V* measurements along the lateral direction. Graph showing lateral *I-V* response of the 1100 °C post-annealed

thin-films with various x values: **(b)** *I-V* plot for measurements taken under dark conditions, **(c)** logarithmic *I-V* plot for measurements taken under dark conditions, **(d)** logarithmic *I-V* plot for measurements taken under dark and light-illuminated conditions. **(e)** Schematics of the device used for the *I-V* measurements along the vertical direction. Graph showing vertical *I-V* response of the 1100 °C post-annealed thin films with various x values: **(f)** *I-V* plot for measurements taken under dark conditions, **(g)** logarithmic *I-V* plot for measurements taken under dark conditions, **(h)** logarithmic *I-V* plot for measurements taken under dark and light-illuminated conditions.

Figures 50f and 50g shows *I-V* plots for measurements taken under dark conditions, where we observe a nonlinear behavior with a shape slightly similar to that of the Schottky barrier is observed along the vertical direction for the thin-films with x = 0.51, x = 0.97, x = 1.07, x = 1.19, and x = 1.29. This slight rectifying behavior is commonly observed for metal/semiconductor contacts especially when the metal contacts are not annealed [134,135]. This is because the barrier height that they introduce inhibits current flow across the metal/semiconductor interface [134,135]. It is well known that when the metal contacts are annealed at a sufficient temperature the *I-V* curves tend to be linear, indicating an ohmic contact. However, in our case, we confirm not test this theory because metal contact annealing causes a short circuit in the device since the structure is a random network. Yet, we know that the Schottky barrier height at metal/semiconductor interfaces is likely the result of [134,135]:

- the work function of the metal contact,
- the crystallinity of the structure,
- the metal atom diffusion from the interface to the semiconductor or
- the outermost electronic configuration of the metal atoms.

Either one or more of these factors can be the reason of this rather semimetallic curves observed in Fig. 50f. Yet, in our case it is more likely to be due to the

chemical environment and the unique network structure of our thin films. If we look at the log-log graph shown in Fig. 50g, we see that thin films with various x values show different curves. Since other factors are constant and the only variable is the thin film composition and morphology, we can argue that the other factors listed above plays no significant role on the curve behavior. Moreover, Fig. 50f and 50g shows that the slopes in the two directions are nearly symmetrical, indicating good quality of the ohmic contacts. Thus, we can rule out the first factor listed above. The metal atom diffusion from the interface to the semiconductor is also a weak effect since our metal contacts are not annealed thus the diffusion is limited. The outermost electronic configuration of the metal atoms most probably does not play a significant role since the configuration is the same for all samples.

Furthermore, *I-V* curve of $x = 0.97$ shows (Fig. 50f and 50g) an avalanche breakdown in the reverse direction at around -0.5 V. This can be explained as follows: When the applied voltage is very large, it accelerates the ejected electrons, which collide with the silicon atoms and eject more electrons due to the momentum conservation. The ejected electrons are also accelerated and collide with other atoms and this process goes on several times, generating an avalanche process, until the current in the semiconductor increases to a level that causes dielectric breakdown in the material. This phenomenon appears in the *I-V* curve as the reverse breakdown.

Figures 50c and 50g reveals another important information, namely that the current increases with increasing Si content. This is expected since any increase in Si concentration results in growth of the average nanocrystal diameters, which leads to the bulk-like behavior in favor of charge transport. More importantly, this is expected when the stoichiometries falls under the Si-rich region. This is also seen from Table 2, which shows the mean current flow, I (A), for dark and light-illuminated *I-V* measurements for the 1100 °C post-annealed thin-films with various x values both in the vertical and in the lateral directions.

Table 2 Table showing the mean current flow, *I* (A), for dark and light-illuminated *I-V* measurements for the 1100 °C post-annealed thin-films with various *x* values both in the vertical and in the lateral directions.

x	**Mean current flow, *I* (A)**			
	Lateral		**Vertical**	
	Dark	**Light**	**Dark**	**Light**
1.29	4.99×10^{-14}	-	1.67×10^{-8}	1.80×10^{-7}
1.19	1.17×10^{-13}	-	-	-
1.07	5.16×10^{-13}	1.03×10^{-12}	2.28×10^{-5}	2.41×10^{-5}
0.97	2.57×10^{-10}	5.47×10^{-10}	1.45×10^{-4}	2.18×10^{-4}
0.51	5.22×10^{-9}	6.35×10^{-9}	1.73×10^{-3}	1.72×10^{-3}

However, we also show reasonably good current flow for the network region, which is the ultimate proof of our claims that the current flows through the anisotropic 3D random network of Si quantum dots. This is true for conduction along both lateral and vertical directions. Naturally, the current flow along the vertical direction shoots up at higher *x* values since the microscale structure is a vertically aligned random network. In addition, another independent confirmation of our claims can be found in the fact that the amount of current produced for the vertical direction is significantly larger than the current produced for the lateral direction. Although we are aware of the fact that comparing device performances shown in Fig. 50a and 50e is not quite proper, we simply cannot ignore the fact that the behavior matches the expectations arising from the unique morphology of the network. Note that even though the amounts of current produced through these devices are largely limited by the device designs, they are still significantly larger than those reported for Si-rich SiO_x thin-films [15,108] and various Si nanostructures [15,108], thanks to the novel nanoarchitecture of the complex network.

We present lateral (Fig. 50d) and vertical (Fig. 50h) *I-V* curves measured for dark and light-illuminated conditions. As can be seen from Fig. 50d, when measurements are taken under light illuminated conditions for thin-film with $x = 0.97$, the current slightly increases, suggesting the presence of little photocurrent. Thin films with $x = 1.29$ shows a slight photocurrent. On the other hand, it is seen in Fig. 50h that an appreciable amount of photocurrent can be seen for the thin film with $x = 1.29$. As in the case of lateral conductivity, the magnitude of the vertical conductivity is limited by the device configuration, since conductivity values reflect only the current flow within the area between the Al point contacts and Al-coated Si substrate, whereas the current flow through the rest of the film is not accounted for (Fig. 19b). In order to gather current flow from the entire film surface we have sputtered an aluminum zinc oxide (AZO) layer between the thin film and the Ag point contacts (Fig. 19c and 51e). Note that Fig. 51a-d are the same as Fig. 50e-h. We have used the same figures again in order to compare them to Fig. 51e-h. As expected, the AZO layer significantly increases the current. Furthermore, the slight rectifying behavior seen in Fig. 51b and 51c is turned to linear, suggesting an ohmic contact when AZO layer is added (Fig. 51f and 51g). Furthermore, the nonlinear, asymmetric *I-V* curves for thin films with $x = 1.29$ and $x = 1.46$ demonstrates Schottky behavior with a good rectification. Lastly, we present lateral (Fig. 51d) and vertical (Fig. 51h) *I-V* curves measured for dark and light-illuminated conditions. As can be seen from Fig. 51d, when measurements are taken under light illuminated conditions for thin-film with $x = 1.29$, the current slightly increases in the forward bias, suggesting the presence of little photocurrent. Similarly, it is seen in Fig. 51h that when measurements are taken under light illuminated conditions for thin-film with $x = 1.29$, the current slightly increases in the forward bias and for thin-films with $x = 1.46$, the current slightly increases in the forward bias. This is also seen from Table 3, which shows the mean current flow, I (A), for dark and light-illuminated *I-V* measurements for the 1100 °C post-annealed thin-films with various x values both for Al/p-Si/thin-film/Al and Al/p-Si/thin-film/AZO/Ag device configurations.

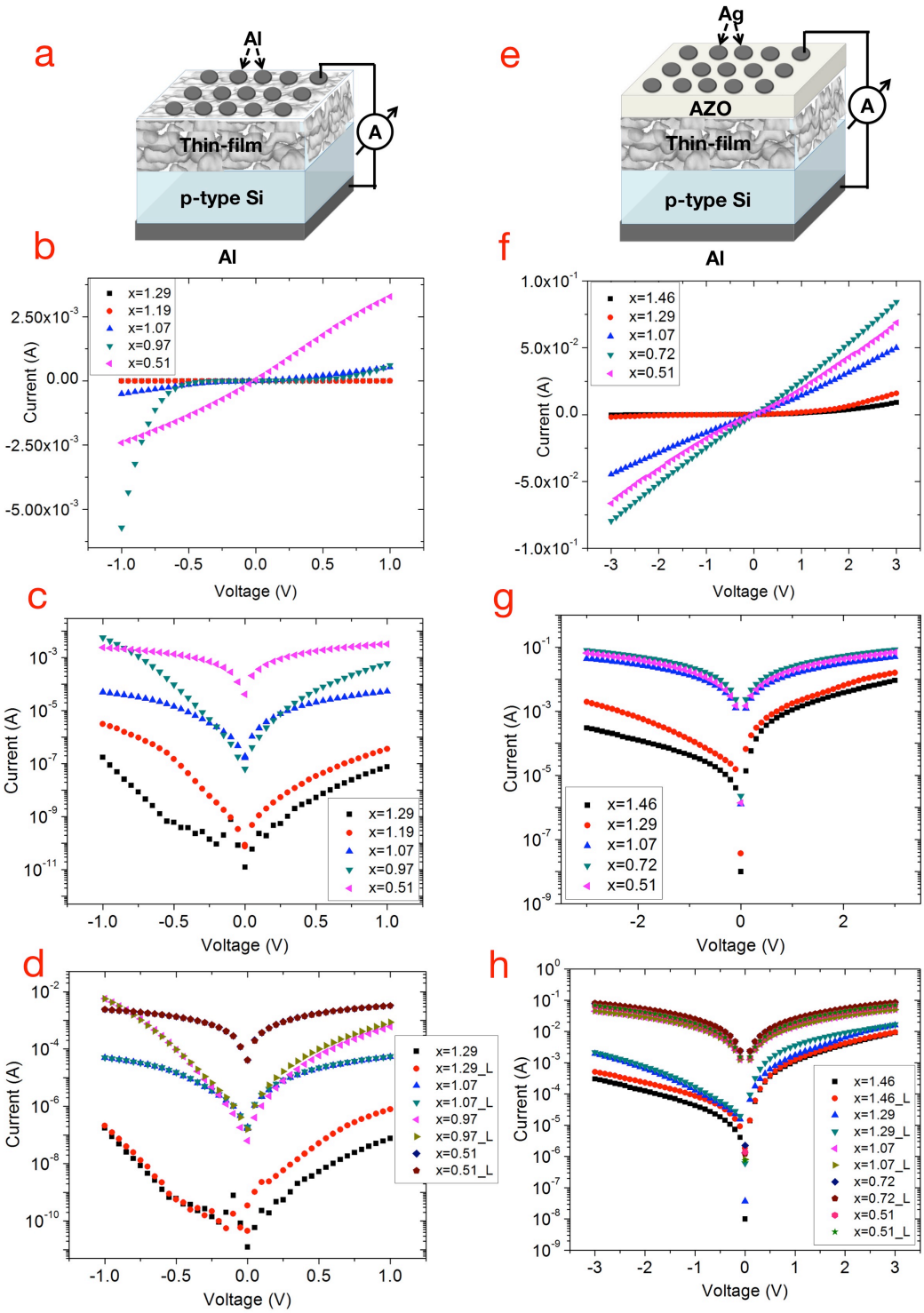

Figure 51 (a) Schematics of the device with Al/p-Si/thin-film/Al configuration used for the *I-V* measurements along the vertical direction. Graph showing vertical *I-V*

response of the 1100 °C post-annealed thin-films with various *x* values: **(b)** linear *I-V* plot for measurements taken under dark conditions, **(c)** logarithmic *I-V* plot for measurements taken under dark conditions, **(d)** logarithmic *I-V* plot for measurements taken under dark and light-illuminated conditions. **(e)** Schematics of the device with Al/p-Si/thin-film/AZO/Ag configuration used for the *I-V* measurements along the vertical direction. Graph showing lateral *I-V* response of the 1100 °C post-annealed thin-films with various *x* values: **(f)** linear *I-V* plot for measurements taken under dark conditions, **(g)** logarithmic *I-V* plot for measurements taken under dark conditions, **(h)** logarithmic *I-V* plot for measurements taken under dark and light-illuminated conditions.

Table 3 Table showing the mean current flow, *I* (A), for dark and light-illuminated *I-V* measurements for the 1100 °C post-annealed thin-films with various *x* values both for Al/p-Si/thin-film/Al and Al/p-Si/thin-film/AZO/Ag device configurations.

x	**Mean current flow, *I* (A)**			
	Al/p-Si/thin-film/Al		**Al/p-Si/thin-film/AZO/Ag**	
	Dark	**Light**	**Dark**	**Light**
1.46	-	-	2.99×10^{-3}	3.27×10^{-3}
1.29	1.67×10^{-8}	1.80×10^{-7}	5.21×10^{-3}	6.84×10^{-3}
1.07	2.28×10^{-5}	2.41×10^{-5}	2.35×10^{-2}	2.37×10^{-2}
0.97	1.45×10^{-4}	2.18×10^{-4}	-	-
0.72	-	-	4.01×10^{-2}	4.11×10^{-2}
0.51	1.73×10^{-3}	1.72×10^{-3}	3.17×10^{-2}	3.3×10^{-2}

To conclude the section, we have proven that the anisotropic 3D random network of Si quantum dots is connected both in the lateral and in the vertical directions. More

importantly, we show that a sufficient amount of current flow through the anisotropic 3D random network of Si quantum dots, without relying on the inefficient tunneling currents.

In this chapter we presented the methodology through which we have fine-tuned the stoichiometry of the thin films, which are fabricated via ballistic deposition. We have fabricated thin-films over a wide range of x values ($0 < x < 2$) in order to pinpoint the range of x values for which the desired morphology can be self-assembled in both the nanoscale and the microscale. We have shown that thin-films with a wide range of x values can be divided into three regions; Si-rich, network, and SiO_2-rich, for which the chemical, structural, optical, and electrical features significantly changes. We further demonstrate that these changes are rather drastic for the network region and we have explained the physical reasons for these observations.

CHAPTER 6

THREE-DIMENSIONAL RANDOM NETWORK OF SILICON QUANTUM DOTS

"Random chance seems to have operated in our favor"
- Spock, Star Trek: The Original Series, Season 2-Episode: The Doomsday Machine

In Chapter 5, we have presented a complete chemical, structural, optical, and electrical analyses of the anisotropic 3D random network of Si quantum dots. In this chapter we will focus only on the key findings of the abovementioned analyses to highlight the scope and to recapitulate the specific aim of the research presented in this thesis. We will summarize the results first for the microscale self-assembly of the vertically aligned random network, and then, for the atomic scale self-assembly of the percolated quantum dot network. Lastly, we will present briefly the proof of quantum confinement and electrical percolation in the random network.

6.1 Microscale Self-Assembly of the Vertically-Aligned Random Network

Microscale self-assembly of the vertically aligned random network is confirmed for an ~330 nm-thick film through EFTEM analysis, in particular valence-band plasmon energy-loss imaging at E_{loss} = 17 eV (Fig. 52a). For the sake of clarity, we also demonstrate the pseudo-colored superposition of the Si (green) and SiO_x (red) plasmon EFTEM images of the same field of view in Fig. 52b.

Furthermore, we have developed a theoretical model to understand the effect of ballistic growth on shape anisotropy and percolation of the random network and to help optimize the experimental parameters. As shown in Fig. 52c-e, we calculate which Si sites are connected through each other (indicated as blue dots) ultimately to

conducting layers at the top and bottom, representing electrodes sandwiching the thin-film. The isolated Si clusters, which do not contribute to current formation, are colored green. One of the key successes of this simple model is that it correctly predicts the range of x values for experimentally observed transition from a disconnected archipelago of quantum dots (for $x > 1.3$) (Fig. 52c), to a sparse, but percolated network (for $1.3 > x > 0.8$) (Fig. 52d), finally to a highly connected but overcrowded network (for $x < 0.8$) (Fig. 52e), for which the quantum confinement is irrevocably lost. These results reveal that at low concentrations, most of the Si sites lack paths connecting them to the electrodes above and below the thin-film. Thus, the disconnected Si sites form small islands of various sizes, like an archipelago, and do not contribute to the conductivity.

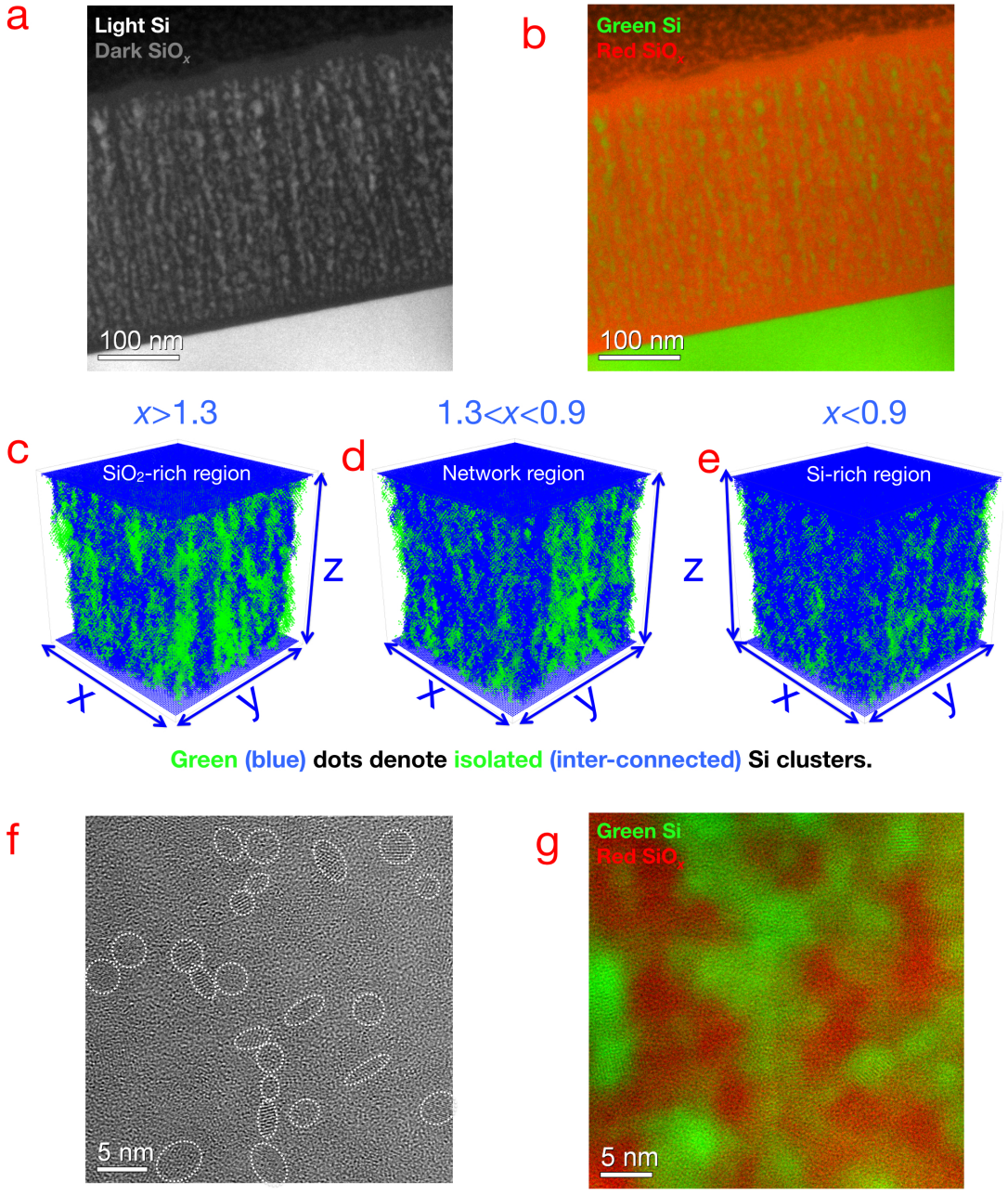

Figure 52 Structural characterization of the random network. Cross-sectional TEM images showing preferential growth of Si quantum dot network in the vertical direction **(a)** Si (bright) and the SiO_x (dark) plasmon EFTEM image. **(b)** Superposition of the Si (green) and the SiO_x (red) plasmon EFTEM images. Numerically calculated structures (green points are isolated Si quantum dots, blue

points are electrically percolated Si quantum dots) of **(c)** SiO_2-rich region for x = 1.46, **(d)** network region for x = 1.07, **(e)** Si-rich region for x = 0.51. Cross-sectional TEM images of Si quantum dot network with an average quantum dot diameter of ~2 nm: **(f)** Zero-loss-filtered HRTEM image. **(g)** Superposition of the Si (green) and SiO_x (red) plasmon EFTEM image of the same field of view as in (f).

6.2 Atomic Scale Self-Assembly of the Percolated Quantum Dot Network

Atomic scale self-assembly of the percolated quantum dot network is confirmed through zero-loss-filtered HRTEM image in Fig. 52f, which only shows Bragg-oriented Si nanocrystals, as well as the pseudo-colored superposition of the Si (green) and SiO_x (red) plasmon EFTEM image shown in Fig. 52g. We stress that both images were taken from exactly the same area of the same sample with dimensions of approximately 25 nm by 25 nm, as shown in Fig. 52a and 52b. As can be seen from the figures that the quantum dots are connected both in lateral and in vertical directions while the average quantum dot diameter remains at ~2 nm, which is well below the critical Bohr radius. These images were also taken from the thin-films that were post-annealed in order to demonstrate that the suboxides are stabilized during the stochastic growth and to prove that they are not affected by the post-annealing procedure. The multiscale topology of the random network is evident from the TEM images, which show that the structure is largely isotropic in the atomic scale (Fig. 52g), and anisotropic (vertically aligned) in the microscopic scale (Fig. 52b).

We verified the material composition through detailed XPS and FTIR analyses on post-annealed thin-films (Fig. 53a-c). Figure 53a shows XPS signal positions of Si oxidation states, Si^{n+} (n = 0, 1, 2, 3, 4) and which Si^{n+} species are present in the Si-rich (for $x < 0.8$), network (for $1.3 > x > 0.8$), and SiO_2-rich (for $x > 1.3$) regions. The suboxides (Si^{1+}, Si^{2+}, and Si^{3+}, which stand for Si_2O, SiO, and Si_2O_3, respectively)

are almost completely phase separated to Si^{0+} (Si) and Si^{4+} (SiO_2) after post-annealing both for the Si-rich samples, where the structure is bulk-like, and the SiO_2-rich samples, where there are isolated quantum dots or short-range ordered Si clusters. However, in the samples corresponding to the network region, the thin-film contains all the suboxides in addition Si and SiO_2, which demonstrates that complete phase separation is prevented and the suboxides are stabilized and have survived the post-annealing procedure at high-temperatures. We also show the integrated peak areas of the FTIR signals originating both from the anti-symmetric Si-O-Si stretching vibrations (SiO_2) and the suboxides (SiO_x) in Fig. 53b. These results show that the intensity of the signal originating from the stable SiO_2 decreases while the intensity of the signal originating from nominally unstable suboxides increases strongly in the network region. This is further confirmed by the XPS analyses shown in Fig. 53c and the molecular dynamics simulations shown in Fig. 53d and 53e. Figure 53c shows the calculated integrated peak areas of the XPS signals originating from Si^{n+} for samples representative of the three regions: Si-rich (for x = 0.51), network (for x = 1.19), and SiO_2-rich (for x = 1.46). As to be expected, the Si-rich region mostly consists of Si, the network region of suboxides, and the SiO_2-rich region of SiO_2.

Molecular dynamics simulations support the key findings of our XPS- and FTIR-based chemical bonding analyses: Figure 53d shows a histogram of Si coordination number defined as the number of O atoms within a given radius (results are presented for a value of 2 Å) surrounding each Si atom, as an indicator of the Si oxidation state for stoichiometries representative of the three regions: Si-rich (for x = 0.51), network (for x = 1.19), and SiO_2-rich (for x = 1.46). The simulations confirm that Si dominates the Si-rich region, SiO_2 dominates the SiO_2-rich region, and the network region is mostly comprised of the suboxides.

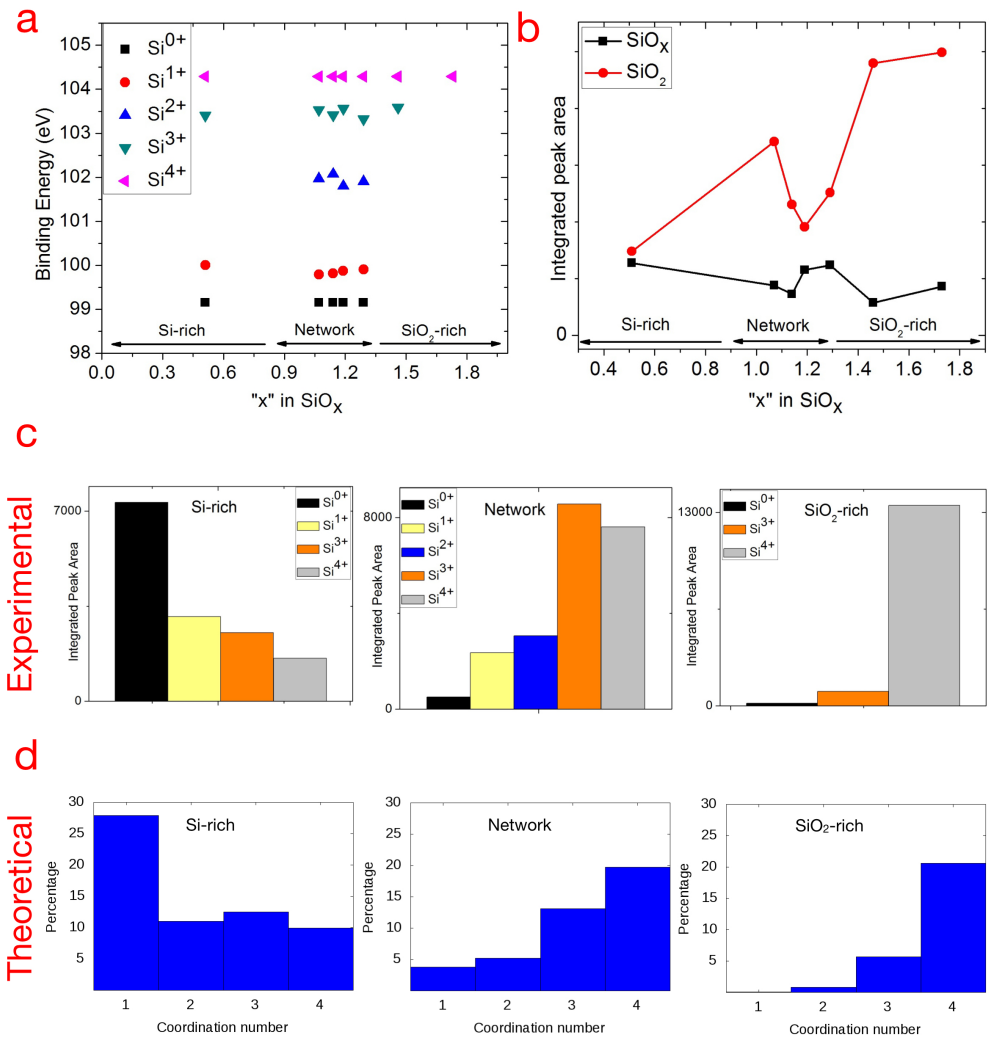

Figure 53 Chemical characterization of the random network. XPS and FTIR analyses show the nominally unstable suboxides are preserved after the post-annealing procedure. **(a)** Graph showing XPS signal positions of Si oxidation states, Si^{n+} (n = 0, 1, 2, 3, 4) and which Si^{n+} species exist in the SiO_2-rich, network, and Si-rich regions. **(b)** Graph showing the relative contributions of stoichiometric, stable, SiO_2 signal to the nominally unstable, SiO_x signal to FTIR spectra for the SiO_2-rich, network, and Si-rich regions. **(c)** Graph showing integrated peak areas of Si^{n+} XPS signals for the Si-rich (for x = 0.51), network (for x = 1.19), and SiO_2-rich (for x = 1.46) regions. Molecular dynamics simulation shows **(d)** Si coordination number histograms for the Si-rich (x = 0.5), network (x = 1), and SiO_2-rich (x = 1.5) regions.

6.3 Quantum Confinement and Electrical Percolation in the Random Network

It is seen from Fig. 52f and 52g that the quantum dots are connected both in the lateral and in the vertical directions, while preserving the average quantum dot diameter at ~2 nm, which is well below the critical Bohr radius. However, inside this random network, unlike quantum dots, free charge carriers are not confined in all three dimensions, resulting in partial loss of confinement for each quantum dot along the spatial direction it is connected to another dot (Fig. 52g). This is confirmed experimentally from PL measurements: As can be seen in Fig. 54a, PL signal intensity of isolated quantum dots (for $x > 1.3$), with an average diameter of ~2 nm, is quite strong whereas it decreases for the network due to the percolated quantum dots. However, thanks to the network being randomly connected, quantum confinement is still preserved on average, as evidenced from the less intense but still strong PL emission and the spectral blueshift with respect to decreasing quantum dot diameters (inset of Fig. 54a).

The preservation of quantum confinement is further verified from the size-dependent optical bandgap of the random network (Fig. 54b). We find that the bandgap decreases from ~4 eV for the SiO_2-rich region (for $x > 1.3$) to ~1.8 eV for Si-rich region. In the network region, the bandgap ranges between $\sim 1.9 < E_g < \sim 2.8$ eV, which covers the visible light spectrum, where half of the sun's power lies in. This suggest that the Si quantum dot network is a very strong candidate for use in photonic devices [4,24-27], specifically solar cells [14-16,19,22-24,27-29]: A solar cell based on an all-Si quantum dot network is particularly exciting due to the possibility and ease of band alignment in a tandem structure [15,16,29]. An independent confirmation is provided by the valence-band plasmon energy-loss TEM images that show increasing quantum dot diameters with increasing Si concentration (decreasing x) for the network region (Fig. 54c-f). These results confirm that quantum confinement is preserved and the bandgap is tunable in the network region over a range of Si concentration levels.

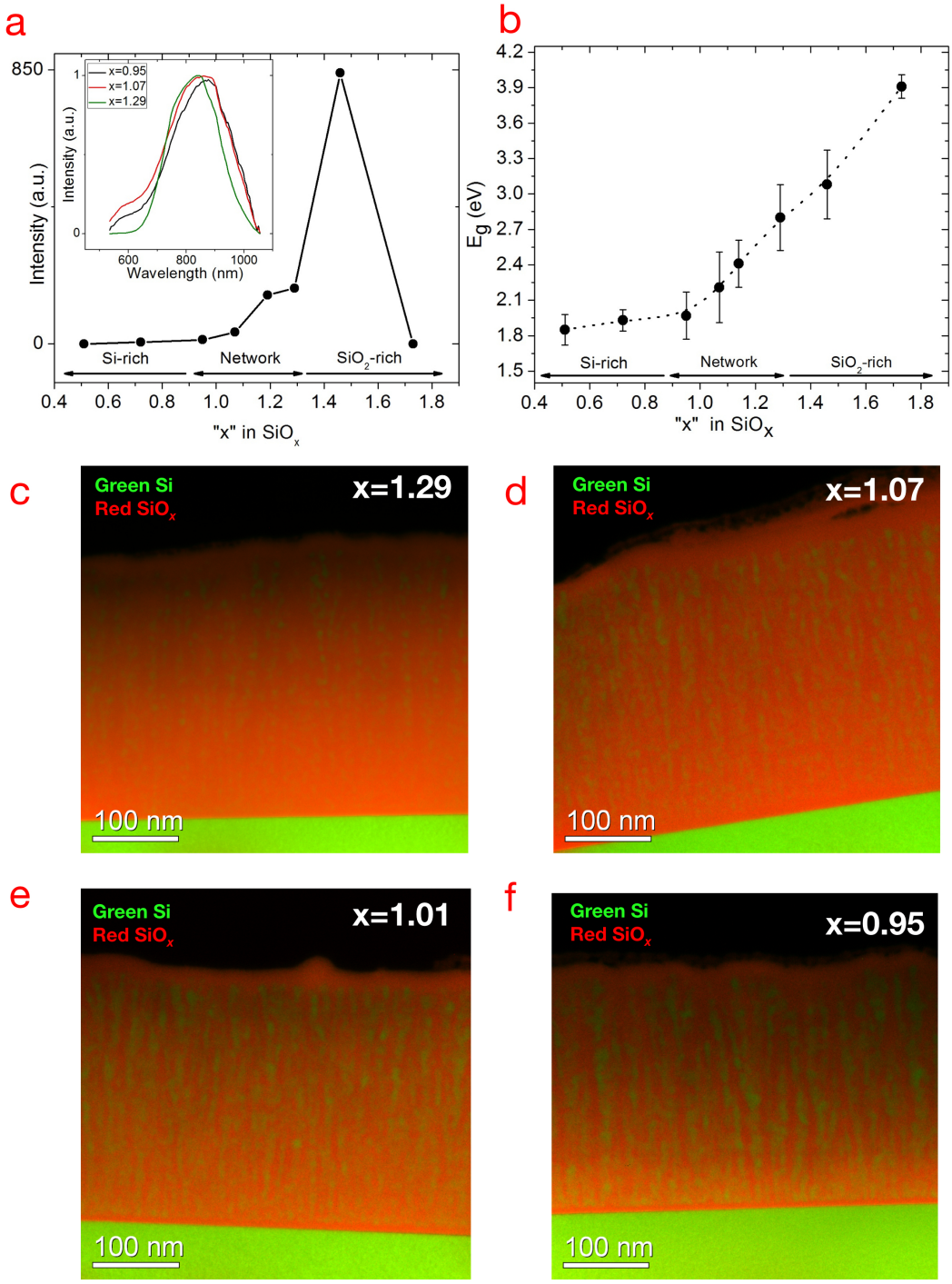

Figure 54 Optical characterization and TEM analyses of the random network. **(a)** Graph showing a highly intense PL signal for the SiO_2-rich region, where the quantum dots are isolated, and a reduced PL signal intensity for the network region,

and virtually zero PL signal for the Si-rich region. Inset shows size-dependent spectral blueshift of PL emission for network region. **(b)** Graph showing size-dependent, tunable optical bandgap from SiO_2-rich to network and Si-rich regions. Superposition of the cross-sectional Si (green) and SiO_x (red) plasmon EFTEM images of the network structure for various x values **(c)** $x = 1.29$, **(d)** $x = 1.07$, **(e)** $x = 1.01$, and **(f)** $x = 0.95$.

Further, we show that the random network exhibits abrupt formation of large-scale connectivity as the density of connections is increased (please refer to Section 2.2 and Fig. 8 for further details). When the Si concentration is increased, conductivity shoots up first in the vertical and later in the lateral directions (Fig. 55b and 55d), indicating ohmic current flow due to percolation without relying on tunnelling currents. The conductivity is examined through *I-V* measurements taken between the thin film and the Si substrate (Fig. 55a) for vertical contacts as a function of x (Fig. 55b). Similarly, we measured the *I-V* dependency between two coplanar aluminium electrodes evaporated onto the film surface on a quartz substrate (Fig. 55c) and determined the conductivity for horizontal contacts as a function of x (Fig. 55d). It is seen that the electrical conduction in the vertical direction increases abruptly at $x < 1.3$, which corresponds to a Si concentration well below the nominal percolation threshold ($x = \sim 1$) of Si in a SiO_x matrix [16,52,53]. As to be expected, conductivity between the horizontal contacts develops at a higher Si concentration, at $x = \sim 1$, which serves as an independent confirmation of the preferentially vertical connectedness of the random network. Although the magnitude of the vertical conductivity is quite high (Fig. 55b), its value is limited by the device configuration (Fig. 55a): Conductivity values reflect only the current flow within the area between the Al point contacts and Al coated Si substrate, whereas the current flow through the rest of the film is not accounted for. Similarly, the magnitude of the lateral conductivity (Fig. 55d) only reflects the current flow between two coplanar Al

contacts (Fig. 55c), which accounts for a thin section close to the surface rather than the ~330 nm-thick film.

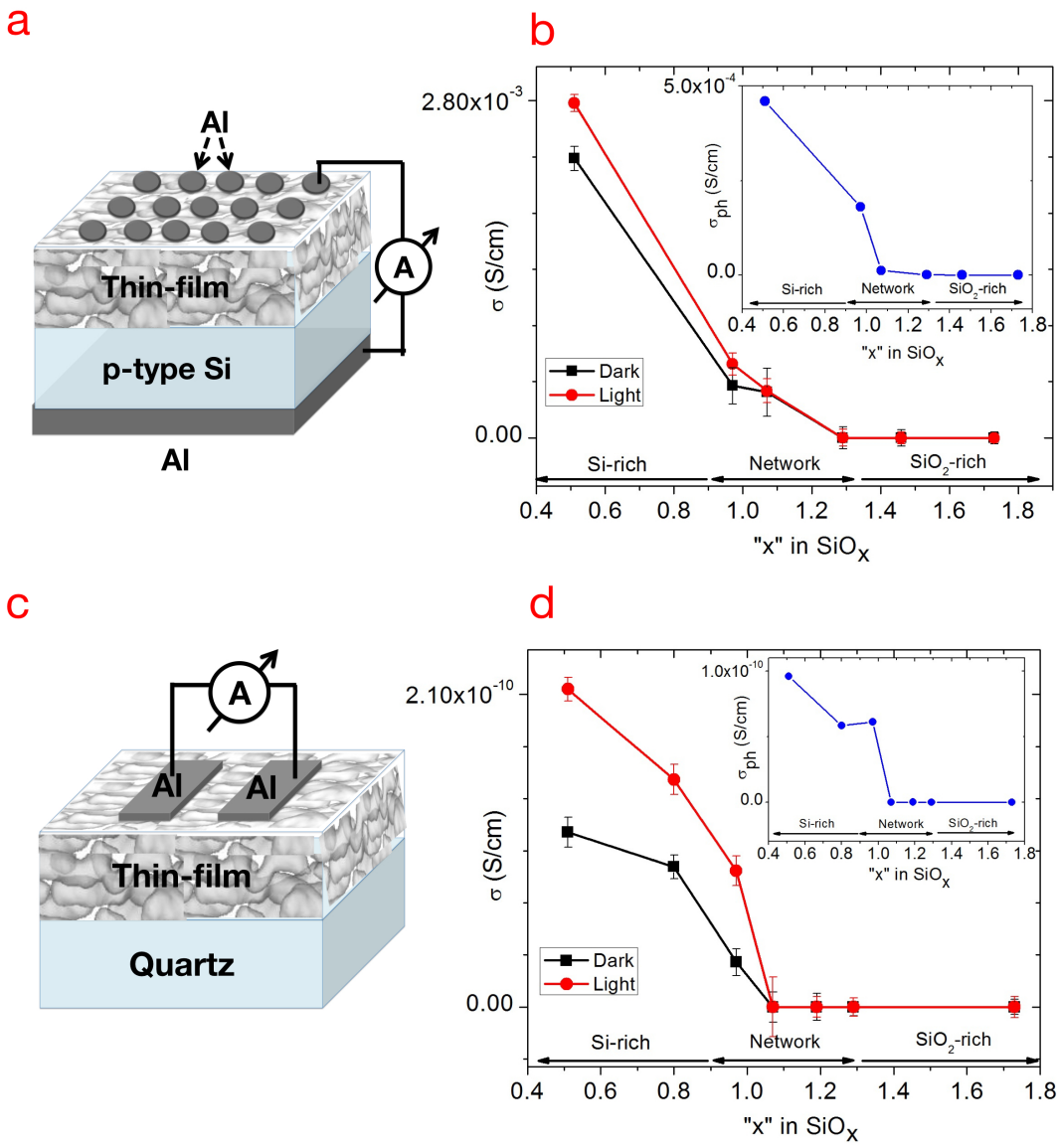

Figure 55 Electrical conductivity of the random network. **(a)** Schematics of the device used for the *I-V* measurements along the vertical direction. **(b)** Graph showing an abrupt increase in the vertical electrical conductivity at $x < 1.3$ (black line represents dark conductivity, red line represents conductivity under light-illuminated

conditions). Inset shows the photoconductivity in the vertical direction. **(c)** Schematics of the device used to conduct *I-V* measurements in the lateral direction. **(d)** Graph showing an abrupt lateral electrical conductivity increase when $x = \sim 1$ (black line represents dark conductivity, red line represents conductivity under light-illuminated conditions). Inset shows photoconductivity in the lateral direction.

Furthermore, the magnitude of the lateral conductivity is also affected negatively by the distance of 1.5 cm between two coplanar Al contacts, which exceeds the transport distance limited by the charge carrier lifetimes. However, full electrical characterization of this complex morphology is beyond the scope of this work and we preferred to use simple device configurations to characterize the lateral and vertical conductivities in order to obtain unambiguous results with straightforward interpretations. Furthermore, we observe a photoelectric effect both for the network and Si-rich regions (insets of Fig. 55b and 55d) as evidenced from the increased conductivity when measurements are taken under light-illuminated conditions. This photoelectric effect also suggests a diverse set of applications of the Si quantum dot network to various photonic devices [14-16,19,22-29]. We note that the magnitudes of conductivity values calculated from light-illuminated measurements are also limited by the device configuration since the Al point and coplanar contacts are partially blocking light interaction with the thin film, where the actual values are likely much higher.

To conclude the chapter, we report a novel Si topology that brings together quantum-dot-like optical properties and good electrical conduction, which can pave the way for a new era in Si photonics [4,14,15,24-26] and photovoltaics [14-16,19,22-29].

CHAPTER 7

CONCLUDING REMARKS, OUTLOOK AND FUTURE WORK

> *"A theory is the more impressive the greater the simplicity of its premises, the more different kinds of things it relates, and the more extended its area of applicability. Hence the deep impression that classical thermodynamics made upon me. It is the only physical theory of universal content concerning which I am convinced that, within the framework of the applicability of its basic concepts, it will never be overthrown."*
>
> *- Albert Einstein, The World As I See It, 1949*

Inspired by nature's methods for self-assembly, we have designed and fabricated a state-of-the-art nanostructure, an anisotropic 3D random network of silicon quantum dots, that effortlessly builds itself from the atomic to the microscopic scales, which can connect to the macroscopic world without detracting from its nanoscale properties.

The results of this thesis have implications for the broad scientific community by virtue of the methodology adopted: We have effectively steered multiscale self-assembly of a complex system towards a stable final state with preplanned properties. Our results demonstrate that a desired outcome can be achieved by following few simple, but cleverly chosen rules that exploit universal stochastic growth dynamics under nonequilibrium conditions and that there is no need for absolute control over every degree of freedom of this otherwise immensely complicated system. Our conceptually designed, theoretically predicted and experimentally demonstrated methodology is inherently adaptable and can serve as a

template for synthesizing other multifunctional materials for numerous applications that would benefit from properties that pertain to different size scales. For this reason, we believe our results provide a fresh perspective and a new impetus for experimental exploitation of multiscale self-assembly of complex systems. In addition to its fundamental significance, our results constitute a technological breakthrough in a 30-year-old problem in optoelectronics, with strong implications for photovoltaics: We demonstrate good current flow and tunable bandgaps, which pertain to microscopic and atomic scales, respectively; two features that were thought to be mutually exclusive. In their recent review article, Priolo, *et al.* (*Nature Nanotech.*, 2014) singled out the problem of having good conductivity together with bandgaps, stating "*Once this has been achieved, we can look forward to silicon nanostructures combining quantum-dot-like optical properties and with electrical conduction that may ultimately rival III–V materials*". We have fulfilled this goal through a novel and elegant topology; an anisotropic 3D random network of silicon quantum dots that grows preferentially in the vertical direction, which effortlessly self-assembles from a Si-rich SiO_x thin-film.

Moreover, we proved that the structure is not only robust after exposure to air for more than a year, but also survives prolonged annealing at high-temperatures, and it is highly uniform within a sample and highly reproducible from sample to sample. Combining unique features of this state-of-the-art topology with robustness and reproducibility, we could foresee that anisotropic 3D random network of silicon quantum dots can pave the way for a new era in silicon photonics [4,14,15,24-26], and photovoltaics [14-16,19,22-29]. Apart from its potential electronic, photonic, and photovoltaic applications, this unique architecture could also be used in biophotonics [29], imaging technologies [29], Li-ion batteries [29-31], and chemical and biomedical sensors [32] thanks to its large surface area and very easy fabrication method, combined with its unique properties.

Within the last year, pregnancy, followed by motherhood has induced the author of this thesis to think and read about biological morphogenesis. This is another key mechanism that nature uses to grow multi-functional structures. We now realize the powerful and versatility of this mechanism in "self-assembling" extremely complex systems, but it is simply not utilized in our man-made materials or systems. As demonstrated in this thesis, nonequilibrium dynamics allows to reach otherwise unreachable stable states. Sequential symmetry breakings appear to underlie morphogenesis in nature. A particularly fruitful and original direction may be to learn how to exploit symmetry breaking through defects or external perturbations to synthesize new nanomaterials. In the future, the author of this thesis intends to focus on a research direction, the ultimate aim of which will be to realize a 3D material synthesizer of complex materials with pre-programmed nanostructure, self-organized over multiple scales, subject to nonlinear and stochastic dynamics, similar to a complex biological organism. There is no physical law that precludes this, but first our fundamental understanding needs to develop.

REFERENCES

[1] Waissman, J., Honig, M., Pecker, S., Benyamini, A., Hamo, A., Ilani, S. Realization of pristine and locally tunable one-dimensional electron systems in carbon nanotubes. Nature Nanotech. 8, 569–574 (2013).

[2] Wolfowicz, G., Tyryshkin, A.M., George, R.E., Riemann, H., Abrosimov, N.V., Becker, P., Pohl, H.-J., Thewalt, M.L.W., Lyon, S.A., Morton, J.J.L. Atomic clock transitions in silicon-based spin qubits. Nature Nanotech. 8, 561–564 (2013).

[3] Xiea, C., Hansonb, L., Cuia, Y., Cuib, B. Vertical nanopillars for highly localized fluorescence imaging. PNAS 108, 3894-3899 (2011).

[4] Klimov, V.I., Mikhailovsky, A.A., Xu, S., Malko, A., Hollingsworth, J.A., Leatherdale, C.A., Eisler, H.-J., Bawendi, M.G. Optical gain and stimulated emission in nanocrystal quantum dots. Science 290, 314–317 (2000).

[5] Boal, A.K., Ilhan, F., DeRouchey, J.E., Thurn-Albrecht T., Russell, T.P., Rotello, V.M. Self-assembly of nanoparticles into structured spherical and network aggregates. Nature 404, 746-748 (2000).

[6] Lopinski, G.P., Wayner, D.D.M., Wolkow, R.A. Self-directed growth of molecular nanostructures on silicon. Nature 406, 48-51 (2000).

[7] Walt, D.R. Nanomaterials: Top-to-bottom functional design. Nature Mater. 1, 17-18 (2002).

[8] Fichthorn, K., Scheffler, M. Nanophysics: A step up to self-assembly. Nature 429, 617-618 (2004).

[9] Kippelen, B. Optical materials: Self-assembly reaches new heights. Nature Mater. 3, 841-843 (2004).

[10] Grubbs, R.B. Nanoparticle assembly: Solvent-tuned structures. Nature Mater. 6, 553-555 (2007).

[11] Hammond, P.T. Form and function in multilayer assembly: New applications at the nanoscale. Adv. Mater. 16, 1271-1293 (2004).

[12] Gleiter, H. Nanostructured materials: Basic concepts and microstructure. Acta Materiala 48, 1-29 (2000).

[13] Mann, S. Self-assembly and transformation of hybrid nano-objects and nanostructures under equilibrium and non-equilibrium conditions. Nature Mater. 8, 781-791 (2009).

[14] Priolo, F., Gregorkiewicz, T., Galli, M., Krauss, T.F. Silicon nanostructures for photonics and photovoltaics. Nature Nanotech. 9, 19-32 (2014).

[15] Si nanocrystals: Fundamentals, synthesis, and applications. Edited by Lorenzo Pavesi & Rasit Turan, Wiley-VCH Verlag GmbH & Co. (2010).

[16] Balberg, I., Jedrzejewski, J., Savir, E. Electrical transport in three-dimensional ensembles of silicon quantum dots. Phys. Rev. B 83, 035318 (2011).

[17] Nigro, B., Grimaldi, C., Ryser, P., Chatterjee, A.P., van der Schoot P. Quasiuniversal connectedness percolation of polydisperse rod systems. Phys. Rev. Lett. 110, 015701 (2013).

[18] Balberg, I. Tunnelling and percolation in lattices and the continuum. J. Phys. D: Appl. Phys. 42, 064003 (2009).

[19] Yan, R., Gargas, D., Yang, P. Nanowire photonics. Nature Photon. 3, 569-576 (2009).

[20] Min, Y., Akbulut, M., Kristiansen, K., Golan, Y. Israelachvili, J. The role of interparticle and external forces in nanoparticle assembly. Nature Mater. 7, 527 - 538 (2008).

[21] Escarcega-Bobadilla, M.V., Zelada-Guillen, G.A., Pyrlin, S.V., Wegrzyn, M., Ramos, M.M.D., Gimenez, E., Stewart, A., Maier, G., Kleij, A.W. Nanorings and rods interconnected by self-assembly mimicking an artificial network of neurons. Nature Commun. 4, 2648 (2013).

[22] Nie, Z., Petukhova, A. Kumacheva E. Properties and emerging applications of self-assembled structures made from inorganic nanoparticles. Nature Nanotech. 5, 15 - 25 (2010).

[23] Jia, G., Sitt, A., Hitin, G.B., Hadar, I., Bekenstein, Y., Amit, Y., Popov, I., Banin, U. Couples of colloidal semiconductor nanorods formed by self-limited assembly. Nature Mater. 13, 301-307 (2014).

[24] Gudiksen, M.S., Lauhon, L.J., Wang, J., Smith, D.C., Lieber, C.M. Growth of nanowire superlattice structures for nanoscale photonics and electronics. Nature 415, 617-620 (2002).

[25] Pavesi, L., Dal Negro, L., Mazzoleni, C., Franzo, G., Priolo, F. Optical gain in silicon nanocrystals. Nature 408, 440-444 (2000).

[26] Dasgupta, N.P., Sun, J., Liu, C., Brittman, S., Andrews, S.C., Lim, J., Gao, H., Yan, R., Yang, P. 25th anniversary article: Aemiconductor nanowires: Synthesis, characterization, and applications. Adv. Mat. 26, 2137–2184 (2014).

[27] Shah, A., Torres, P., Tscharner, R., Wyrsch, N., Keppner, H. Photovoltaic technology: The case for thin-film solar cells. Science 285, 692-698 (1999).

[28] Nozik, A.J. Quantum dot solar cells. Physica E 14, 115–120 (2002).

[29] Conibeer, G., Green, M., Corkish, R., Cho, Y., Cho, E.-C., Jiang, C.-W., Fangsuwannarak, T., Pink, E., Huang, Y., Puzzer, T., Trupke, T., Richards, B., Shalav, A., Lin, K.-L. Silicon nanostructures for third generation photovoltaic solar cells. Thin Solid Films 511, 654-662 (2006).

[30] Chan, C.K., Peng, H., Liu, G., McIlwrath, K., Zhang, X.F., Huggins, R.A., Cui, Y. High-performance lithium battery anodes using silicon nanowires. Nature Nanotech. 3, 31-35 (2008).

[31] Bogart, T.D., Oka, D., Lu, X., Gu, M., Wang, C., Korgel, B.A. Lithium ion battery peformance of silicon nanowires with carbon skin. ACS Nano 8, 915-922 (2014).

[32] Cui, Y., Wei, Q. Park, H., Lieber, C.M. Nanowire nanosensors for highly sensitive and selective detection of biological and chemical Species. Science 293, 1289-1292 (2001).

[33] Öktem, B., Pavlov, I., Ilday, S., Kalaycıoğlu, H., Rybak, A., Yavaş, S., Erdoğan, M., Ilday, F.Ö. Nonlinear laser lithography for indefinitely large

area nanostructuring with femtosecond pulses. Nature Photon. 7, 897-901 (2013).

[34] Garlaschelli, D., Capocci, A., Caldarelli, G. Self-organized network evolution coupled to extremal dynamics. Nature Phys. 3, 813-817 (2007).

[35] Barzel, B., Barabasi, A.-L. Universality in network dynamics. Nature Phys. 9, 673-681 (2013).

[36] Kyrylyuk, A.V., Hermant, M.C., Schilling, T., Klumperman, B., Koning, C.E., van der Schoot, P. Controlling electrical percolation in multicomponent carbon nanotube dispersions. Nature Nanotech. 6, 364-369 (2011).

[37] Rabani, E., Reichman, D.R., Geissler, P.L., Brus, L.E. Drying-mediated self-assembly of nanoparticles. Nature 426, 271-274 (2003).

[38] Barabasi, A.-L., Stanley, H.E. Fractal concepts in surface growth. Cambridge University Press (1995).

[39] Yip, H.-L. Zou, J., Ma, H., Tian, Y., Tucker, N.M., Jen, A.K.-Y. Patterning of robust self-assembled n-type hexaazatrinaphthylene-based nanorods and nanowires by microcontact printing. J. Am. Chem. Soc. 128, 13042-13043 (2006).

[40] Lee, Y.S. Self-assembly and nanotechnology systems, design, characterization, and applications. Wiley-VCH Verlag GmbH & Co. (2011).

[41] Miles, R.W., Hynes, K.M., Forbes, I. Photovoltaic solar cells: An overview of state-of-the-art cell development and environmental issues. Prog. Cryst. Growth Charact. Mater. 51 (2005) 1-42.

[42] Yuan, Z., Anopchenko, A., Daldosso, N., Guider, R., Navarro-Urrios, D., Pitanti, A., Spano, R., Pavesi, L. Silicon nanocrystals as an enabling material for silicon photonics. Proceedings of the IEEE 97, 7 (2009).

[43] Panthani, M.G., Korgel, B.A. Nanocrystals for electronics; Book series: Annual review of chemical and biomolecular engineering, Vol: 3; 287-311.

[44] Goetzberger, A., Hebling, C., Schock, H-W. Photovoltaic materials, history, status and outlook. Mater. Sci. Eng., R 40, 1–46 (2003).

[45] Peng, K.-Q., Lee, S.-T. Silicon nanowires for photovoltaic solar energy conversion; Adv. Mater. 23, 198–215 (2011).

[46] Gunawan, O., Wang, K., Fallahazad, B., Zhang, Y., Tutuc, E., Guha, S. High performance wire-array silicon solar cells. Prog. Photovolt: Res. Appl. 19, 307–312 (2011).

[47] Conibeer, G., Perez-Wurfl, I., Hao, X., Di, D., Lin, D. Si solid-state quantum dot-based materials for tandem solar cells. Nanoscale Res. Lett. 7, 193 (2012).

[48] Nanocrystalline Silicon for Nanophotonics, http://nanotech.fzu.cz/26/index.php?file=4, last visited on August 2014.

[49] The Fuss About Quantum Dots, http://www.photonics.com/, last visited on August 2014.

[50] Donega, C.M. Synthesis and properties of colloidal heteronanocrystals. Chem. Soc. Rev., 40, 1512-1546 (2011).

[51] Quantum Dots: Research, technology, and applications. Edited by Randolf W. Knoss, Nova Science Publishers, Inc. (2009).

[52] Hamilton, B. Jacobs, J., Hill, D.A., Pettifer, R.F., Teehan, D., Canham, L.T. Size-controlled percolation pathways for electrical conduction in porous silicon. Nature 393, 443-445 (1998).

[53] Manna, L., Milliron, D.J., Meisel, A., Scher, E.C., Alivisatos, A.P. Controlled growth of tetrapod-branched inorganic nanocrystals. Nature Mater. 2, 382-385 (2003).

[54] Kamat, P.V. Quantum dot solar cells: Semiconductor nanocrystals as light harvesters. J. Phys. Chem. C 112 (2008) 18737–18753.

[55] The global climate and energy project (GCEP), http://web.stanford.edu/group/gcep/cgi-bin/gcep-research/all/nanostructured-silicon-based-tandem-solar-cells/, last visited on August 2014.

[56] PV Education.Org, http://pveducation.org/pvcdrom/solar-cell-operation/tandem-cells, last visited on August 2014.

[57] Davies, J.H. The physics of low-dimensional semiconductors: An introduction. Cambridge University Press (1998).

[58] Handbook of Nanophysics: Nanoparticles and Quantum Dots. Edited by Klaus D. Sattler, Taylor and Francis Group (2011).

[59] Silicon Photonics. Edited by Lorenzo Pavesi and David J. Lockwood, Springer-Verlag (2004).

[60] Mazor, A., Srolovitz D.J., Hagan, P.S., Bukiet, B.G. Columnar growth in thin-films. Phys. Rev. Lett. 60, 424-427 (1988).

[61] Robledo, A., Grabill, C.N., Kuebler, S.M., Dutta, A., Heinrich, H., Bhattacharya, A. Morphologies from slippery ballistic deposition model: A bottom-up approach for nanofabrication. Phys. Rev. E. 83, 051604 (2011) .

[62] Kardar, M., Parisi, G., Zhang, Y.-C. Dynamic scaling of growing interfaces. Phys. Rev. Lett. 56, 889-892 (1986).

[63] Stauffer, D., Aharony, A. Introduction to Percolation. CRC Press (1994).

[64] Grimmett, G. Percolation. Springer-Verlag (1989).

[65] Barabasi, A.-L. Linked: The new science of networks. Plume Books (2003).

[66] Mandelbrot, B.B. The fractal geometry of nature. Freeman (1982).

[67] Bak, P. How nature works. Copernicus (1996).

[68] Gleick, J. Chaos: Making a new science. Penguin Books (1997).

[69] Pastor-Satorras, R., Vespignani, A. Evolution and structure of the internet: A statistical physics approach. Cambridge University Press (2004).

[70] Dorogovtsev, S.N., Mendes, J.F.F. Evolution of networks: From biological nets to the internet and www (Physics) Oxford University Press (2003).

[71] Cohen, R., Havlin, S. Complex networks: Structure, robustness and function. Oxford University Press (2010).

[72] Visual Studio Magazine, http://visualstudiomagazine.com/articles/2013/09/01/neural-network-training-using-back-propagation.aspx, last visited on August 2014.

[73] Ben.Knows.Code, http://www.benknowscode.com/2012/10/using-html5-canvas-to-create-cracked_3621.html, last visited on August 2014.

[74] Citylab, http://www.citylab.com/commute/2013/02/weve-been-looking-spread-global-pandemics-all-wrong/4782/, last visited on August 2014.

[75] The OPTE Project, www.opte.org, last visited on August 2014.

[76] Wahl, http://www.wahl.org/fe/HTML_version/link/FE1W/c1.htm, last visited on August 2014.

[77] Hofstadter, D.R. Gödel, Escher, Bach: An eternal golden braid. Penguin Books (2000).

[78] Hofstadter, D.R. I am a strange loop. Basic Books (2008).

[79] Kurzweil, R. How to create a mind. Gerald Duckworth & Co Ltd (2014).

[80] Stavarache, I., Ciurea, M.L. Percolation phenomena in Si–SiO_2 nanocomposite films. J. Optoelectron. Adv. Mater. 9, 2644–2647 (2007).

[81] Lepadatu, A.M., Rusnac, E., Stavarache, I. Percolation phenomena in silicon-based nanocrystalline systems. Semiconductor Conference CAS 2007 International (2007).

[82] Tomozeiu, N. Electrical conduction and dielectric relaxation of a-SiO_x thin films deposited by reactive RF magnetron sputtering. Thin Solid Films 516, 8199–8204 (2008).

[83] Azulay, D., Millo, O., Savir, E., Conde, J.P., Balberg, I. Microscopic and macroscopic manifestations of percolation transitions in a semiconductor composite. Phys. Rev. B 80, 245312 (2009).

[84] Pereira, R.N., Niesar, S., You, W.B., da Cunha, A.F., Erhard, N., Stegner, A.R., Wiggers, H., Willinger, M.-G., Stutzmann, M., Brandt, M.S. Solution-processed networks of silicon nanocrystals: The role of internanocrystal medium on semiconducting behavior. J. Phys. Chem. C 115, 20120–20127 (2011).

[85] Zhigunov, D.M., Emelyanov, A.V., Timoshenko, V.Y., Sokolov, V.I., Seminogov, V.N. Percolation effect in structures with amorphous and crystalline silicon nanoclusters. Phys. Status Solidi C 9, 1474–1476 (2012).

[86] Pelesko, J.A. Self assembly: The science of things that put themselves together. Chapman and Hall/CRC (2007).

[87] Phys. Org., http://phys.org/news/2011-12-physicist-scale-lhc-atlas-lego.html, last visited on August 2014.

[88] Nathan Savaya, http://brickartist.com/tag/lego-art/, last visited on August 2014.

[89] Cronodon, http://cronodon.com/BioTech/Virus_Tech.html, last visited on August 2014.

[90] Sematech, http://www.sematech.org/meetings/archives/litho/9025/Pres/DSA-01-Hinsberg.pdf, last visited on August 2014.

[91] Sethna, J.P. Statistical mechanics: Entropy, order parameters, and complexity. Oxford University Press (2006).

[92] Barabasi, A.-L. Burst: The hidden pattern behind everything we do. Plume Books (2011).

[93] Forsyth, D.R. Group dynamics. 5th Edition. Wadsworth Publishing Company (2009).

[94] Corwin, I. The Kardar-Parisi-Zhang equation and universality class. arXiv:1106.1596 [math.PR] (2011).

[95] Vold, M.J. the sediment volume in dilute dispersions of spherical particles. J. Phys. Chem. 64, 1616 (1960).

[96] Barenblatt, G.I. Scaling, self-similarity, and intermediate asymptotics. Cambridge University Press (1996).

[97] Sachdev, P.L. Self-similarity and beyond: Exact solutions of nonlinear problems. CRC, New York (2000).

[98] Smid, B., Li, Z., Ikova, A.D. Arey, B.W., Smith, R.S., Matolin, V., Kay, B.D., Dohnallek, Z. Characterization of nanoporous WO_3 films grown via ballistic deposition. J. Phys. Chem. C 116, 10649−10655 (2012).

[99] Flaherty, D.W., Dohnalek, Z., Dohnalkova, A., Arey, B.W., McCready, D.E., Ponnusany, N., Mullins, C.B., Kay, B.D. Reactive ballistic deposition of porous TiO_2 films: Growth and characterization. J. Phys. Chem. C 111, 4765-4773 (2007).

[100] Malaca, M., Egerton, R.F. Observations of the microscopic growth mechanism of pillars and helices formed by glancing-angle thin-film deposition. J. Vac. Sci. Technol. A 19, 158 (2001).

[101] Kim, J., Dohnalek, Z., Kay, B.D. Structural characterization of nanoporous Pd films grown via ballistic deposition. Surf. Sci. 586, 137-145 (2005).

[102] Dick, B., Brett, M.J., Smy, T.J., Freeman, M.R., Malac, M., Egerton, R.F. Periodic magnetic microstructures by glancing angle deposition. J. Vac. Sci. Technol. A 18, 1838 (2000).

[103] Smy, T., Vick, D., Brett, M.J., Dew, S.K., Wu, A.T., Sit, J.C., Harris, K.D. Three-dimensional simulation of film microstructure produced by glancing angle deposition. J. Vac. Sci. Technol. A 18, 2507 (2000).

[104] Ilday, S., Ilday, F.Ö., Ustunel, H., Toffoli, D., Nogay, G., Friedrich, D., Hübner, R., Schmidt, B., Heinig, K.-H., Turan, R. Si nano-VINe: Electrical percolation in quantum-confined nc-Si:SiO_2 systems. arXiv:1309.4400 [cond-mat.mtrl-sci] (2013).

[105] Nogay, G., Ozkol, E., Ilday, S., Turan, R. Structural peculiarities and aging effect in hydrogeneted a-Si prepared by inductively coupled plasma chemical vapor deposition technique. Vacuum (in press).

[106] Chapman, B. Glow discharge processes: Sputtering and plasma etching. Wiley-Interscience (1980).

[107] Barbagiovanni, E.G., Goncharova, L.V., Simpson, P.J. Electronic structure study of ion-implanted Si quantum dots in a SiO_2 matrix: Analysis of quantum confinement theories. Phys. Rev. B 83 035112 (2011).

[108] Optoelectronics: Materials and techniques. Edited by Padmanabhan Predeep. InTech (2011).

[109] Mirabella, S., Agosta, R., Franzo, G., Crupi, I., Miritello, M., Lo Savio, R., Di Stefano, M.A., Di Marco, S., Simone, F., Terrasi, A. Light absorption in silicon quantum dots embedded in silica. J. Appl. Phys. 106, 103505 (2009).

[110] Tauc, J. Amorphous and liquid semiconductors. Springer (1974).

[111] Tompkins, H.G., McGahan, W.A. Spectroscopic ellipsometry and reflectometry: A user's perspective. John Wiley & Sons (1999).

[112] Yu, J., Sinnott, S.B., Phillpot, S.R. Charge optimized many-body potential for the Si/SiO_2 system. Phys. Rev. B 75, 085311 (2007).

[113] Shan, T.-R., Devine, B.D., Hawkins, J.M., Asthagiri, A., Phillpot, S.R., Sinnott, S.B. Second-generation charge-optimized many-body potential for Si/SiO_2 and amorphous silica. Phys. Rev. B 82, 235302 (2010).

[114] Plimpton, S. Fast parallel algorithms for short-range molecular dynamics. J. Comp. Phys. 117, 1-19 (1995).

[115] Smit, C., Van Swaaij, R., Donker, H., Petit, A., Kessels, W., Van de Sanden, M. Determining the material structure of microcrystalline silicon from Raman spectra. J. Appl. Phys. 94, 3582-3588 (2003).

[116] Wenger, R. Isosurfaces: Geometry, topology, and algorithms. CRC Press (2013).

[117] Kelly, T.F., Miller, M.K. Invited review article: Atom probe tomography. Rev. Sci. Instrum. 78, 031101 (2007).

[118] Szekeres, A., Vlaikova, E., Lohner, T., Petrik, P., Huhn, G., Havancsak, K., Lisovskyy, I., Zlobin, S., Indutnyy, I.Z., Shepeliavyi, P.E. Ellipsometric characterization of SiO_x films with embedded Si nanoparticles. Vacuum 84, 115–118 (2010).

[119] En Naciri, A., Mansour, M., Johann, L., Grob, J.J., Eckert, C. Correlation between silicon nanocrystalline size effect and spectroscopic ellipsometry responses. Thin Solid Films 455, 486–490 (2004).

[120] Agocs, E., Petrik, P., Milita, S., Vanzetti, L., Gardelis, S., Nassiopoulou, A.G., Pucker, G., Balboni, R., Fried, M. Optical characterization of nanocrystals in silicon rich oxide superlattices and porous silicon. Thin Solid Films 519, 3002–3005 (2011).

[121] Ilday, S., Nogay, G., Turan, R. Spectroscopic ellipsometry studies of Si nanocrystals embedded in a SiO_x matrix: Modelling and optical

characterization. Appl. Surf. Sci. (in press, available online: http://www.sciencedirect.com/science/article/pii/S0169433214009295).

[122] Soulairol, R., Cleri, F. Interface structure of silicon nanocrystals embedded in an amorphous silica matrix. Solid State Sci. 12, 163-171 (2010).

[123] Ben-Chorin, M., Averboukh, B., Kovalev, D., Polisski, G., Koch, F. Influence of quantum confinement on the critical points of the band structure of Si. Phy. Rev. Lett. 77, 763-766 (1996).

[124] Kovalev, D., Heckler, H., Polisski, G., Koch, F. Optical properties of Si nanocrystals. Phys. Stat. Sol. B 215, 871-932 (1999).

[125] Lee, K.-J., Kang, T.-D., Lee, H., Hong, S.H., Choi, S.-H., Seong, T.-Y., Kim, K.J., Moon, D.W. Optical properties of SiO_2/nanocrystalline Si multilayers studied using spectroscopic ellipsometry. Thin Solid Films 476, 196–200 (2005).

[126] Gravalidis, C., Gioti, M., Laskarakis, A., Logothetidis, S. Real-time monitoring of silicon oxide deposition processes. Surf. Coat. Technol. 180, 655–658 (2004).

[127] Tomozeiu, N., van Faassen, E.E., Habraken, F.H.P.M. Structural transition in silicon suboxides at critical oxygen content. Annals of West University of Timisoara, Series Chemistry 12, 3, 1039 – 1046 (2003).

[128] Ruddy, D.A., Johnson, J.C., Smith, E.R., Neale, N.R. Size and bandgap control in the solution-phase synthesis of near-infrared-emitting germanium nanocrystals. ACS Nano 4, 7459-7466 (2010).

[129] Mogaddam, N.A.P., Ilday, S., Turan, R., Finstad, T.G. Influence of Ge content and annealing conditions on the PL properties of nc-$Si_{1-x}Ge_x$ embedded in SiO_2 matrix in weak quantum confined regime. J. Lumin. 155, 170-179 (2014).

[130] Kartopu, G., Sapelkin, A.V., Karavanskii, V.A., Serincan, U., Turan, R. Structural and optical properties of porous nanocrystalline Ge. J. Appl. Phys. 103, 113518 (2008).

[131] Balberg, I, Savir, E., Jedrzejewski, J. The mutual exclusion of luminescence and transport in nanocrystalline networks. J. Non-Cryst. Solids 102, 338-340 (2004).

[132] Ravindra, N.M., Auluck, S., Srivastava, V.K. On the Penn gap in semiconductors. Phy. Stat. Sol B 93, K155 - K160 (1979).

[133] Keleş, Ü., Liedke, B., Heinig, K.-H., Bulutay, C. Networks of silicon nanowires: a large-scale atomistic electronic structure analysis. arXiv:1311.3708 [cond-mat.mes-hall] (2013).

[134] Kolaklieva, L., Kakanakov, R., Avramova, I., Marinova, Ts. Nanolayered Au/Ti/Al ohmic contacts to p-type SiC: Electrical, morphological and chemical performances depending on the contact composition. Materials Science Forum, Vols. 556-557 (2007).

[135] Micro electronic and mechanical systems. Edited by Kenichi Takahata. InTech (2009).

VITA

SERİM KAYACAN İLDAY

Academic Affiliation:	Department of Micro and Nanotechnology and Center for Solar Energy Research and Applications (GÜNAM), Middle East Technical University
Date/Place of Birth:	09.11.1979 / Konya
Postal Address:	ODTÜ, Fizik Bölümü, Z-41, 06800, Ankara-Turkey
Phone:	++90-312-210-4324
E-mail:	serim.ilday@metu.edu.tr

EDUCATION

University	Subject of Study	Degree	Country	Graduation Year
Middle East Technical University	Micro and Nanotechnology	Ph.D.	Turkey	2014
Ankara University	Chemistry	M.S.	Turkey	2007
Selçuk University	Chemistry	B.S.	Turkey	2003

ACADEMIC EXPERIENCE

Institution	Country	Department	Title	Dates
Middle East Technical University	Turkey	Micro and Nanotechnology	Research Assistant	2010-2014
Bilkent University	Turkey	Materials Science and Nanotechnology	Teaching and Research Assistant	2007-2010
Ankara University	Turkey	Chemistry	Research Assistant	2005-2007

WORK EXPERIENCE

Institution	Country	Division	Title	Dates
FiberLAST Inc.	Turkey		Consultant	05-08/2011
Ministry of Health	Turkey	Strategy Development	Project Coordinator	2004-2007
Unilever	Turkey	DiverseyLever	Summer Trainee	05-08/2001

AREAS OF EXPERTISE

Nanoscience; Advanced multifunctional materials; Material processing and characterization; Solid state electronic devices; Solar cells; Semiconductor engineering; Laser-material interactions; Plasma science; Vacuum technology; Ultra-hard, wear and heat resistant coatings; Low-dimensional, high-tech ceramics; Carbon nanotubes; Statistical pyscics; Self-assembly.

RESEARCH EXPERIENCE

Experience in thin-film deposition systems:

Physical vapor deposition (PVD), chemical vapor deposition (CVD), pulsed laser deposition (PLD), plasma-assisted chemical vapor deposition (PECVD), thermal and e-beam evaporation.

Experience in material characterization techniques:

Scanning electron microscope (SEM), environmental scanning electron microscope (ESEM), energy-dispersive X-ray spectroscopy (EDX), electron backscatter diffraction (EBSD), transmission electron microscopy (TEM), electron energy loss spectroscopy (EELS), scanning transmission electron microscopy (STEM), energy filtered transmission electron microscopy (EFTEM), atomic force microscopy (AFM), optical microscopes, spectroscopic ellipsometry, photoluminescence, conductivity measurements, X-ray diffraction spectroscopy (XRD), grazing incidence X-ray diffraction spectroscopy (GIXRD), X-ray

photoelectron spectroscopy (XPS), Fourier transform infrared spectroscopy (FTIR), grazing incidence reflection (FTIR-GIR), attenuated total reflectance (FTIR-ATR), Raman spectroscopy, secondary ion mass spectroscopy (SIMS), ultraviolet-visible spectroscopy (UV-Vis), micro- & nano-indentation analysis, dektak, tribometric analysis, precision cutting, polishing, grinding equipment, mounting press, cross-sectional TEM-sample preparation techniques.

Experience in software:

Monte-Carlo, LabVIEW, LATEX, OriginLab, Mathematica, Matlab.

AWARDS

Award	**Granted By**	**Year**
Board of Trustees Scholarship Award for graduate study	Bilkent University	2007

PERSONAL DEVELOPMENT

- Representative of Ministry of Health in European Union negotiations in the Screening Meeting on Chapter 18 - Statistics held in Brussels (2006-2007),
- Representative of Ministry of Health to the World Health Organization (2006-2007),
- Representative of Ministry of Health in the "Health Transition Project" financed by the World Bank (2005-2007),
- Grant proposal writing experience (proposals prepared for: FP7, TÜBİTAK, World Bank, Ankara University).

Journal Reviewer

Materials Science and Engineering B, Energy Sources, Part A, Journal of Applied Physics, Nanoscale Research Letters

Industrial Impact

I have developed four kinds of ultra-hard, wear- and heat-resistant coatings for Art&Craft division of Güral Porselen to improve the lifetimes of glass forming molds. These coatings were verified and successfully implemented in the actual fabrication process, resulting in concrete industrial impact.

I have also developed ultra-hard, wear- and heat-resistant coatings for Erciyes University, Department of Dentistry to be used to improve the lifetime of dental drill bits. It is proven that the lifetimes of these dental drill bits are improved at least four times. Commercialization process is in progress and a US patent is pending.

PATENTS

Patent Title	**Patent Number**	**Country**
Dental implant drill bit with nano-engineered protective coating	pending	USA

PUBLICATIONS IN JOURNALS

1. G. Kucukayan, **S. Kayacan**, B. Baykal, E. Bengu. Use of saccharides as solid-state precursors for the synthesis of carbon nanotubes. *Materials Research Society Symposium Proceedings* **1081E**, 1081-P05-14 (2008).
2. G. Kucukayan, R. Ovali, **S. Ilday**, B. Baykal, H. Yurdakul, S. Turan, O. Gulseren, E. Bengu. Experimental and theoretical examination of the effect of sulfur on the pyrolytically grown carbon nanotubes from sucrose-based solid state precursors. *Carbon* **49**, 508-517 (2011).
3. B. Öktem, I. Pavlov, **S. Ilday,** H. Kalaycıoğlu, A.S. Rybak, S. Yavaş, M. Erdoğan, F.Ö. Ilday. Nonlinear laser lithography for indefinitely large area nanostructuring with femtosecond pulses. *Nature Photonics* **7**, 897-901 (2013).

4. **S. Ilday**, F.Ö. Ilday, H. Ustunel, D. Toffoli, G. Nogay, D. Friedrich, R. Hübner, B. Schmidt, K-H. Heinig, R. Turan. Si nano-VINe: Electrical Percolation in Quantum-Confined nc-Si:SiO_2 Systems. arXiv:1309.4400 [cond-mat.mtrl-sci] (2013).
5. **S. Ilday**, Z. Mısırlıoğlu, M. Canel, A. Sınağ. Removal of methylene blue from aqueous media by using cokes obtained from lignite pyrolysis. *Energy Sources, Part A* **36**, 2183–2193 (2014).
6. N.A.P. Mogaddam, **S. Ilday**, R. Turan, T.G. Finstad. Influence of Ge content and annealing conditions on the PL properties of nc-$Si_{1-x}Ge_x$ embedded in SiO_2 matrix in weak quantum confined regime. *Journal of Luminescence* **155**, 170-179 (2014).
7. **S. Ilday,** G. Nogay, R. Turan. Spectroscopic ellipsometry studies of Si nanocrystals embedded in a SiO_x matrix: Modelling and optical characterization. *Applied Surface Science* (in press, available online: http://www.sciencedirect.com/science/article/pii/S0169433214009295).
8. G. Nogay, E. Ozkol, **S. Ilday**, R. Turan. Structural Peculiarities and Aging Effect in Hydrogeneted a-Si Prepared by Inductively Coupled Plasma Chemical Vapor Deposition Technique. *Vacuum* (in press).
9. N. Er, A. Alkan, **S. Ilday**, E. Bengu. Examination of protective dental drill bit coatings: Effects on the alveolar bone temperature and drill bit lifetime. *Clinical Implant Dentistry and Related Research* (under revision).
10. **S. Ilday**, F.Ö. Ilday, H. Ustunel, D. Toffoli, G. Nogay, D. Friedrich, R. Hübner, B. Schmidt, K-H. Heinig, R. Turan. Multi-scale self-assembly of quantum dots into an anisotropic three-dimensional random network. *Science* (submitted).
11. **S. Ilday**, G. Nogay, E. Ozkol, R. Turan. Novel silicon nanostructures from Ballistic deposition: A bottom up approach for nanofabrication. (in preparation).
12. **S. Ilday**, B. Altuntas, S. Mirabella, S. Cosentino, R. Raciti, I. Kabacelik, A. Terrasi, R. Turan. Fabrication and a complete structural, optical and electrical

analyses of porous Ge nanostructures embedded in a dielectric matrix. (in preparation).

13. Z.M. Saleh, **S. Ilday**, B. Altuntas, R. Turan. ESR studies on the percolated and quantum-confined silicon quantum dots. (in preparation).
14. Z.M. Saleh, **S. Ilday**, R. Turan. Atmospheric aging and light-induced degredation silicon quantum dot network. (in preparation).

REFEERED CONFERENCE PAPERS

1. Z. Mısırlıoğlu, **S. Kayacan**, M. Canel, A. Sınağ. Adsoprtion of methylene blue from aqueous solution onto lignite-based cokes. *6th International Conference of the Chemical Societies of the South-Eastern European Countries*, Sofia-Bulgaria, September 2008.
2. G. Kucukayan, **S. Kayacan**, B. Baykal, E. Bengu. Saccharides as solid-state precursors for carbon nanotube synthesis. *Symposium on Surface Science*, Ankara, Turkey, March 2008.
3. **S. Kayacan**, M. F. Genisel, C. Karakaya, Z. Say, M. Kayhan, E. Bengu. Effect of precursors on boron carbide morphology. *Symposium on Surface Science*, Ankara, Turkey, March 2008.
4. M. F. Genisel, **S. Kayacan,** E. Bengu. The effect of gas ratio and substrate bias on the chemistry of r.f. reactive sputter deposited B-C-N films. *Symposium on Surface Science*, Ankara, Turkey, March 2008.
5. G. Kucukayan, **S. Kayacan**, M.F. Genisel, B. Baykal, E. Bengu. Use of saccharides as solid-state precursors for the synthesis of carbon nanotubes. *Materials Research Society (MRS) Spring Meeting*, San Francisco-California, USA, March 2008.
6. **S. Kayacan**, M. F. Genisel, C. Karakaya, Z. Say, M. Kayhan, E. Bengu. Catalyst induced vapor-solid growth route for the synthesis of boron carbide platelets and whiskers. *4th Nanoscience and Nanotechnology Conference (NanoTR 4)*, Istanbul, Turkey, June 2008.

7. M. F. Genisel, **S. Kayacan**, E. Bengu. Effect of gas ratio and substrate bias on the chemistry of R.F reactive sputter deposited BCN films. *4th Nanoscience and Nanotechnology Conference (NanoTR 4)*, Istanbul, Turkey, June 2008.
8. G. Kucukayan, **S. Kayacan**, B. Baykal, E. Bengu. Synthesis of carbon nanotubes using saccharides as solid state precursor. *4th Nanoscience and Nanotechnology Conference (NanoTR 4)*, Istanbul, Turkey, June 2008.
9. G. Kucukayan, **S. Kayacan**, B. Baykal, E. Bengu. Synthesis of carbon nanotubes using saccharides as solid state precursor. *2nd Workshop on Anisotropic Science and Technology of Materials (ASTMD-2)*, Gebze-Kocaeli, Turkey, June 2008.
10. M.F. Genisel, **S. Ilday**, B. Baykal, R. Ovali, O. Gulseren, E. Bengu. Experimental and theoretical investigation of the hardness and friction performance of B-N-C films. *2nd International Conference on Computational Methods in Structural Dynamics and Earthquake Engineering (COMPDYN 2009)*, Island of Rhodes, Greece, June 2009.
11. N. Er, A. Alkan, E. Bengu, **S. Ilday.** Examination of the Effects of Heat Production in Bone Caused by Dental Implant Drill Bits with Different Surface Characteristics. *American Association of Oral and Maxillofacial Surgeons (AAOMS) 2010*, Chicago, USA, September 2010.
12. N. Er, A. Alkan, E. Bengu, **S. Ilday**. Examination of the Effects of Heat Production in Bone Caused by Dental Implant Drill Bits with Different Surface Characteristics. *5th Ağız ve Çene-Yüz Cerrahisi Birliği Derneği (AÇBİD) International Conference on Oral and Maxillofacial Surgery Society*, Antalya, Turkey, May 2011.
13. **S. Ilday**, N.A.P. Moggaddam, R. Turan. Investigation on Silicon-nanosponge Structures Prepared by Magnetron Sputtering for Photovoltaic Applications. *Energy Challenges for Advanced Materials and Processes: Harvesting, Storage and Efficient Utilization (EnCAMP 2011)*, Cappadocia, Turkey, May 2011.
14. **S. Ilday**, N.A.P. Moggaddam, R. Turan. Investigation on Silicon-nanosponge Structures Prepared by Magnetron Sputtering for Photovoltaic Applications. *7th*

Nanoscience and Nanotechnology Conference (NanoTR 7), Istanbul, Turkey, June 2011.

15. **S. Ilday**, N.A.P. Moggaddam, R. Turan. Investigation on Silicon-nanosponge Structures Prepared by Magnetron Sputtering for Photovoltaic Applications. *26th European PV Solar Energy Conference and Exibition (26th EU PVSEC)*, Hamburg, Germany, September 2011.
16. **S. Ilday**, R. Turan, E. Sungur Ozen, S. Gundogdu, A. Aydinli. Synthesis and characterization of sponge-like silicon nanostructures for photovoltaic applications. *European Materials Research Society (E-MRS) Spring Meeting*, Strasbourg, France, May 2012.
17. **S. Ilday**, R. Turan, E. Sungur Ozen, S. Gundogdu, A. Aydinli. Synthesis and characterization of sponge-like silicon nanostructures for photovoltaic applications. *Photovoltaic Technical Conference - Thin Film & Advanced Silicon Solutions*, Aix-en-Provence, France, June 2012.
18. S. Gündogdu, E. Sungur Özen, **S. Ilday**, R. Turan, A. Aydınlı. Synthesis of silicon nanocrystals by laser annealing of silicon rich oxides. *8th Nanoscience and Nanotechnology Conference (NanoTR 8)*, Ankara, Turkey, June 2012.
19. M. Kulakci, H. E. Unalan, **S. Ilday**, G. Nogay, R. Turan. Si nanostructures for an efficient light harvesting in photovoltaic solar cells. *XXI International Materials Research Congress*, Cancun, Mexico, August 2012.
20. G. Nogay, **S. Ilday**, R. Turan. Spectroscopic Ellipsometry Studies of nc-Si/a-Si and nc-Si/SiO_x Systems: Optical Characterization of Crystallization. *27th European PV Solar Energy Conference and Exibition (27th EU PVSEC)*, Frankfurt, Germany, September 2012.
21. G. Nogay, **S. Ilday**, R. Turan, K-H. Heinig, D. Friedrich. Spectroscopic Ellipsometry Studies of nc-Si/a-Si and nc-Si/SiO_x Systems: Optical Characterization of Crystallization. *SolarTR-2*, Antalya, Turkey, November 2012.
22. **S. Ilday**, G. Nogay, R. Turan. Spectroscopic Ellipsometry Studies of Magnetron-Sputtered nc-Si/SiO_x Systems: Modeling and Optical Characterization. *9th*

Nanoscience and Nanotechnology Conference (NanoTR 9), Erzurum, Turkey, June 2013.

23. B. Altuntas, **S. Ilday,** R. Turan, S. Mirabella, S. Cosentino, R. Raciti, A. Terrasi. Fabrication and a complete structural, optical and electrical analyses of porous Ge nanostructures embedded in a dielectric matrix. *Solar Energy for World Peace*, Istanbul, Turkey, August 2013.
24. B. Altuntas, **S. Ilday,** M. Yilmaz, R. Turan, S. Cosentino, R. Raciti, I. Crupi, A. Mio, G. Nicotra, A. Terrasi, S. Mirabella. Formation of interconnected Ge nanostructures in SiO_2 matrix by in-situ annealing during co-sputtering of Ge and SiO_2. *European Materials Research Society (E-MRS) Spring Meeting*. Lille, France, May 2014.
25. M. Yilmaz, B. Altuntas, **S. Ilday,** R. Turan, S. Cosentino, R. Raciti, I. Crupi, A. Mio, G. Nicotra, A. Terrasi, S. Mirabella. Electrical and optical properties of sponge-like Ge embedded in dielectric matrix for solar cell applications. *European Materials Research Society (E-MRS) Spring Meeting*, Lille, France, May 2014.
26. R. Turan, **S. Ilday**, E. Ozen, S. Gundogdu, A. Aydinli. Sponge-like silicon nanostructures for third generation photovoltaic solar cells. *TMS Middle East - Mediterranean Materials Congress (MEMA 2015)*, Doha, Qatar, January 2015.